QUINONE DERIVATIVES AS NOVEL SINGLE-MOLECULE COMPONENTS FOR NANO-ELECTRONICS

Grant J. Simpson

A Thesis Submitted for the Degree of PhD
at the
University of St Andrews

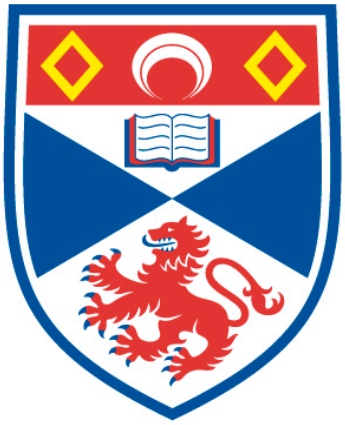

2014

Quinone derivatives as novel single-molecule components for nano-electronics

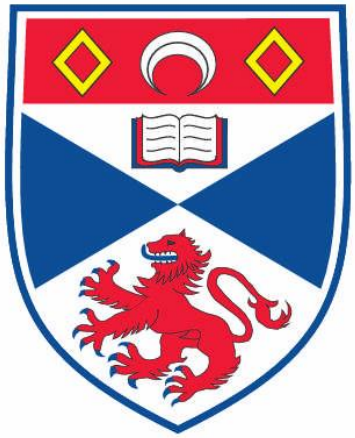

A thesis submitted for the degree of PhD

By

Grant J. Simpson

Supervised by Dr Renald Schaub

School of Chemistry
University of St Andrews
August 2014

Declaration

1. Candidate's declarations:

I, Grant J. Simpson, hereby certify that this thesis, which is approximately 33,000 words in length, has been written by me, and that it is the record of work carried out by me, or principally by myself in collaboration with others as acknowledged, and that it has not been submitted in any previous application for a higher degree.

I was admitted as a research student in September, 2010 and as a candidate for the degree of Doctor of Philosophy in September, 2010; the higher study for which this is a record was carried out in the University of St Andrews between 2010 and 2014.

Date …….. Signature of candidate ……

2. Supervisor's declaration:

I hereby certify that the candidate has fulfilled the conditions of the Resolution and Regulations appropriate for the degree of Doctor of Philosophy in the University of St Andrews and that the candidate is qualified to submit this thesis in application for that degree.

Date …….. Signature of supervisor …….

3. Permission for publication:

In submitting this thesis to the University of St Andrews I understand that I am giving permission for it to be made available for use in accordance with the regulations of the University Library for the time being in force, subject to any copyright vested in the work not being affected thereby. I also understand that the title and the abstract will be published, and that a copy of the work may be made and supplied to any bona fide

library or research worker, that my thesis will be electronically accessible for personal or research use unless exempt by award of an embargo as requested below, and that the library has the right to migrate my thesis into new electronic forms as required to ensure continued access to the thesis. I have obtained any third-party copyright permissions that may be required in order to allow such access and migration, or have requested the appropriate embargo below.

The following is an agreed request by candidate and supervisor regarding the publication of this thesis: embargo on both [all or part of] printed copy and electronic copy for the same fixed period of 2 years on the following ground: publication would preclude future publication.

Date …….. Signature of candidate ……

Signature of supervisor ……..

Acknowledgement

First and foremost, I thank my supervisor and friend Renald Schaub. His support throughout my PhD studies has been invaluable. I thank him for his enthusiasm when new results were produced, encouragement during work in the lab, and moral support when the stress of writing was getting too much. I'm very grateful for having the opportunity to work with him over the past four years and I have enjoyed every day of it (more or less).

I would also like to thank those in my research group, both past and present. Marco Caffio, who introduced me to the operation of the STM; Catherine Bromley, who I have shared the PhD journey with from day one; Michael John Treanor, for his help in the lab; and Jose Garrido Torres, who started only a short while ago but has produced considerable DFT support for the project. Herbert Früchtl and Tanja van Mourik are also acknowledged for their work on theoretical calculations. Thanks go to Chris Adams at the University of Bristol for synthesis of the investigated molecules. I am grateful to Neville Richardson, Christopher Baddeley, and Manfred Buck for fruitful discussions of the work. Thanks also go to the wider surface science research group at St Andrews for their help and support.

My time in St Andrews has been filled with many enjoyable experiences both in an out of university. For this I have all of my friends to thank. Thank you.

Abstract

In this thesis, quinone derivative molecules supported on a Cu(110) surface are studied using scanning tunnelling microscopy (STM). The experimentally investigated system is based on the bistable nature of these compounds, and so the work is introduced in the wider context of molecular electronics (Chapter 1). The theory and experimental techniques are also described (Chapters 2 and 3). In Chapter 4 the switching behaviour of azophenine (AP) and azotolyline (AT) is characterised using STM imaging and spectroscopy, and is demonstrated to be based on a hydrogen tautomerisation reaction. The activation energy for switching is quantified by measurement of the rate of switching as a function of varying bias voltage, and the process is determined to be stimulated by inelastic electron tunnelling. The reaction pathway is also revealed using theoretical modelling. Chapter 5 focusses on the condensed phase of AP on the Cu(110) surface. The switching behaviour is found to be largely quenched in the self-assembled phase, so statistical analyses of the AP-AP and AP-Cu interactions are conducted in order to try to explain this. Chapter 6 returns to the study of isolated AP molecules and investigates the spatial dependence of the switch with respect to the location of electronic excitation. It is shown that the final state of the molecule can be accurately selected by exciting specific functional groups within the molecule. This control originates from the non-degenerate reaction pathways for the sequential transfer of the two tautomeric protons. The work is then discussed in terms of future outlook and potential applications for bistable molecules.

Contents

1 Introduction

1.1 Motivation

Nanoscience is the study of physical systems at the small scale. It deals with the boundary between the classical and the quantum mechanical regimes. It has widespread reach in all realms of science, including medicine[1,2], electronics[3,4], and robotics[5]. One field which is particularly closely related to nanoscience is surface science: the study of interfaces at a vacuum or between different phases of matter. The study of surfaces allows us to understand the behaviour of atoms and molecules during catalytic processes, their properties of self-assembly, and during the formation of novel nanomaterials such as graphene or carbon nanotubes.

The scanning tunnelling microscope (STM) has led the way in nanotechnology and surface science in the past few decades. Invented in 1982 by Gerd Binnig and Heinrich Rohrer[6], it is the forerunner of a family of scanning probe microscopes (SPM) which would later be realised[7]. The STM allows real-space imaging of surface atoms and molecules, and hence is the ideal tool for nanoscience and nanotechnology. Early implementations aimed simply to resolve the step edges of atomic terraces[6], or to atomically resolve the reconstructed Au(111) herringbone[8] and the Si(111)-(7×7)[9] surfaces. The field advanced in many ways, including a range of different modes of operation, single molecule spectroscopy, and atomic manipulation.

Molecular electronics is an area of nanotechnology that has seen great progress thanks to STM. The current microelectronics industry is based on semiconductor devices which have seen a year-on-year decrease in size as the number of components fitted onto a microchip increases. However, as these components reach atomic dimensions, they do not function in the conventional manner and hence, new concepts for component design must be considered.

Molecular electronics aims to reproduce the function of an electronic component in a single molecule. Since molecules represent the smallest stable complex structures, they provide the ultimate miniaturisation for the electronics industry. The first publication in this field was in 1974[10], but despite a rather long period of time for further advancements, the field is still in its infancy. This reflects the challenges faced with finding suitable candidate molecules, probing their properties on an individual level and, for application, integrating them into a circuit.

A number of examples of different electronic components in molecular form have been realised including a rectifier, diode, transistor, and switch. Of these, switches have seen increased interest because of their ability to output the binary “1” and “0” states which form the basis of all logical circuits. There have been many examples published in the literature which use a range of different mechanisms, as well as a number of methods of activating the switches. These examples will be developed further in this chapter.

An important characteristic of a molecular switch is that it must have two different conductance states while, at the same time, not having a radical change in its shape or size. This is because after integration into a circuit, a molecule which changes significantly will not form a contact after it has been switched. Molecules which do not appreciably change shape include those which undergo an internal change in bonding such as a H-tautomerisation reaction. To date, the number of examples of molecular switches which undergo this process is few. These examples have all been based on the well-known porphyrin type molecule. This thesis expands this narrow range of H-tautomeric switches by developing a new class of molecules which undergo the same process, but possess an altogether different and unrestricted chemical structure. Furthermore, the controllability of the tautomerisation process will be addressed. Being able to say with certainty the state of a molecule is an important factor when considering future applications for molecular components such as memory storage devices and conductance switching. The ordering of these molecules is also investigated with the intention of producing high density arrays of components which far surpass the density of today’s transistors placed on a microchip.

1.2 Outline of the Thesis

Chapter 1 provides a motivation for the thesis and outlines its content before going on to introduce the study of single molecules on surfaces, molecular electronics, and specifically, molecular switches. Chapters 2 and 3 deal with the predominantly used technique: STM. A detailed explanation of the experimental and theoretical principles, as well as the pertinent spectroscopic modes, is given. The end of chapter 2 introduces density functional theory (DFT) which was used in many cases to compare experimental results to theoretical predictions. Chapter 4 is concerned with a new class of Cu(110)-bound molecular switches involving H-tautomerism, namely azophenine. Chapter 5 looks at azophenine at higher surface coverage on Cu(110) and its self-assembly into ordered, two dimensional arrays. Chapter 6 investigates

the controllability of the state of azophenine and how this may be applied to future nanoelectronics.

1.3 Molecules on Surfaces

The study of organic molecules on metal surfaces gives insight into a plethora of interesting chemical, physical and biological processes. Their study in this environment is important in a diverse range of research fields such as heterogeneous catalysis[11–13], nanomechanical biosensors[4] and nano electronics[14]. Both fundamental research and anticipation of applications in nanotechnology have driven research of molecules on surfaces forward greatly in recent years. STM has revolutionised the way that organic molecules on surfaces are studied due to the ability to probe the properties and directly manipulate individual molecules. The remainder of this chapter will review recent advancements on organic molecules on surfaces before going on to describe, in detail, the concept of molecular electronics. A focus will be put on STM studies of these systems; a full explanation of the STM technique will be given in the next chapter.

For small molecules such as O_2, NO and H_2O, properties such as diffusion, binding energy, adsorption site and desorption have been well documented on a range of different surfaces[15–17]. However, for larger organic molecules, such properties are poorly understood. The interaction of molecules is determined by many factors including the metal substrate used and the crystallographic face onto which the molecule is deposited. Once adsorbed, processes such as diffusion and ordering are determined by interactions between the surface and molecule (physisorption, chemisorption) and between the molecules themselves (van der Waals interactions, hydrogen bonding and dipole-dipole interactions).

Molecules, when given sufficient thermal energy, are able to diffuse on a surface. Any system will relax into the lowest energy equilibrium configuration, and for molecules on a surface this often results in self-assembly. This can be defined as the coalescence of groups of molecules held together by lateral intermolecular bonds to form a lower energy, stable structure. The self-assembly can lead to phenomena useful in catalysis such as chiral recognition and amplification to allow enantiopure self-assembled domains to be formed[18]. Another example of self-assembly is the construction of two-dimensional supramolecular networks[19]. Their ordering is controlled by the position of molecular functional units and the forces of attraction between them. Furthermore, their dimensions and porosity can be altered by selection of

different sized spacer groups. Careful control of these factors allows the study of host-guest interactions and confinement of molecular motion[20]. With real-space imaging, STM allows easy identification of the order and structure of these self-assembled networks.

STM has also been instrumental in developing so called single molecule chemistry. Due to the ease by which individual species can be manipulated, it is possible to bring reactants close to each other (as is a requirement during chemical reactions). The energy required to activate a reaction may also be applied by tunnelling electrons from the STM tip, thus providing an extremely local and selective method of controlling the steps of a chemical reaction. The discovery, in 1904, by Ullmann *et al.*[21], that biphenyl may be produced by reaction of iodobenzene in the presence of a copper powder catalyst was performed and imaged at the single molecule level in 2000[22]. This saw the manipulation of two iodobenzene molecules along a step edge of a Cu(111) crystal so that they were in close proximity. Using tunnelling electrons, the iodine atoms were dissociated from each molecule. The phenyl radicals were then brought close together and with the use of further inelastic tunnelling, were reacted to form a stable, single biphenyl molecule.

By controlling specific reactions one can direct a reaction along a coordinate that would ordinarily not be followed and allows study of exotic species or catalytic selectivity. Other processes which are accessible using STM include control of the stretching or umbrella motions of ammonia. Using inelastic tunnelling electrons, it is possible to induce translation or desorption of single molecules selecting which vibration is excited[23]. Further examples include real-time imaging of the formation of coordination compounds[24], and formation of covalently bonded networks through Ullmann coupling[25]. Molecular electronics is another expanding field where the control of reaction dynamics at the single molecule level is important. STM not only offers the ability to do this, but also allows measurements of conductivity which are important in the characterisation of molecular components.

1.4 Molecular Electronics

Since the invention of the first semiconductor transistor in 1947[26] (for which Bardeen, Brattain and Shockley were awarded the Nobel Prize for Physics in 1956) and the first silicon-based transistor in 1954, this device has seen a remarkable miniaturisation. Semiconductor devices have seen a vast miniaturisation through three orders of magnitude since 1971 (10 μm) to today (14 nm) and this has been spurred on by the modern computer and electronics

industry's demand for high speed processing. Modern lithographic techniques allow production of devices as small as 14 nm today and this is expected to decrease to 7 nm in 2017. However, this miniaturisation cannot go on indefinitely.

In the sixties, co-founder of Intel Corporation, Gordon E. Moore, postulated a well-known "law" which states that every two years a two-fold increase in the number of components placed on a microchip (accompanied by a doubling of computational speed) will be observed (Figure 1.1). This trend has, in fact, accelerated in recent years with a doubling of computational speed being observed approximately every 18 months.

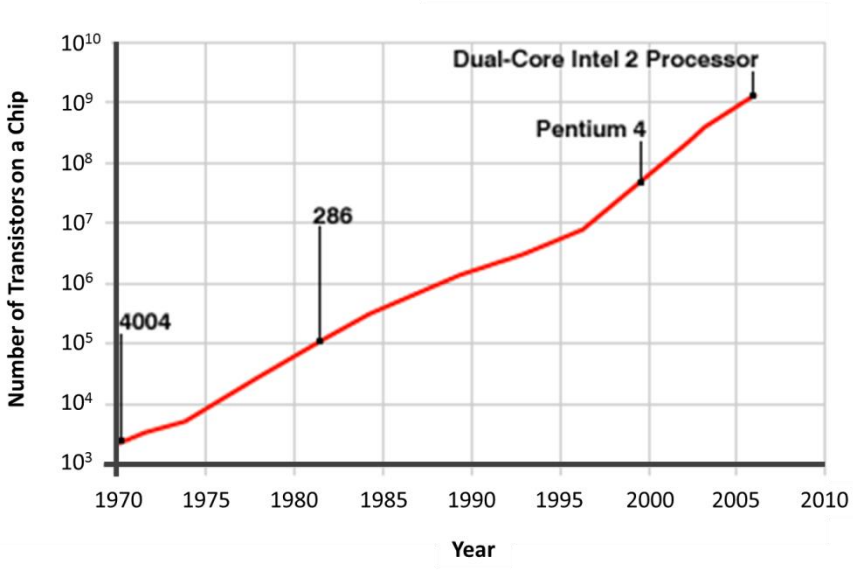

Figure 1.1 Prediction made by Gordon E. Moore showing the exponential increase in transistors placed on an electronic microchip.

The phenomenal increase in computing power faces a severe cost as the component size approaches atomic dimensions. Aside from the exponential increase in production cost, heat dissipation at this scale has become a major obstacle. Furthermore, a fundamental limit in size will be reached when the operation of such components is compromised by effects such as quantum tunnelling. A conceptually new approach to the design of nanoelectronic components is therefore required.

The field of molecular electronics presents an altogether different approach to the handling of information at the nanometre scale. Broadly speaking, molecular electronics aims to reproduce the function of an electronic component in a single molecule. Since molecules are the smallest complex structures it is seen as the ultimate form of miniaturisation. Using this approach, problems such as heat dissipation and production cost may be reduced. The issue of

heat dissipation may be avoided when considering molecular electronics because single electrons are required to activate processes in molecular components, as well as relaxation from excited states being accompanied, in many cases, by photon emission rather than phonons. The latter is addressed by chemical synthetic techniques which provide simple, large-scale production methods for molecular components.

The first paper published in this field came from Aviram and Ratner in 1974 in which they proposed a molecular structure capable of rectification of electrical current[10]. Calculations were based on unidirectional current flow through a molecule which had acceptor and donor moieties separated by and insulating σ-electron system. For about 20 years, this prediction was not confirmed experimentally[27], and very little research was conducted in this field. Some work in the 80s in which biological processes in proteins and DNA were used as the basis of "switchable molecular machines" sparked interest. However, the hype surrounding so called biochips was ill-founded and funding in this area suffered[28].

With the invention of the STM, and a coinciding interest in nanotechnology in the 1990s, molecular electronics started to regain popularity, and the first experimental measurement of the rectification properties of organic molecules was published[27]. The experimental challenges faced when incorporating single molecules into an electrical circuit, however, remained. In the past decade the field has exploded in research activity with electronic components such as transistors[29], resistors/wires[30], diodes[31], and switches[32,33] all being realised at the molecular level. Further components such as molecular amplifiers have been treated recently at a theoretical level[34].

The STM has advanced the field greatly because of the ability to "see" and manipulate molecules on metal surfaces. Furthermore, the set-up of STM in which the metallic or semiconducting sample and the tip act as electrodes (simulating incorporation into an electrical circuit), while at the same time allows spectroscopic measurements, means that it is the ideal tool to study molecular electronics[35].

1.5 Molecular Switches

A specific area of molecular electronics which has seen advancement in its own right is the study of switchable molecules. A molecule must meet two requirements in order to function as a switch: it must possess two or more distinguishable, stable states; and it must be able to

change between them on demand. “Switching” in molecules is not a new concept and has been known since the first observation of dynamic isomerism/tautomerism. However, their consideration as electronic devices requires precise control and measurement at an individual level as discussed previously. They have attracted more attention than any other molecular device, possibly due to their ability to represent logical 1 and 0 states but at extremely small scales. In addition to performing the function of a switch, they could act as memory elements with improved properties over today’s size (~nanometres), speed (~picoseconds), and stability (large energy barrier between states) standards.

The first and simplest switch to be observed, employed the STM set-up to reversibly transfer a xenon atom from a nickel surface to the tip[36]. This led to different conductance states being measured for the two situations. This “atom switch”, although rudimental, was a proof of concept for further more complex molecular designs. Since this study, a plethora of molecular switches have been investigated, and it is therefore necessary to categorise them depending on their chemical structure, their switching mechanism, or the stimulus used to induce a switch event. The remainder of this chapter will define these different categories and review specific examples of each.

The chemical structure is a natural way to classify similar molecular switches because, usually, a prototype is developed and then a number of derivatives are studied which are chemical functionalisations of the original molecule. The most well-known such family is that based on the azobenzene molecule. Further groups include porphyrins[37], catenanes and rotaxanes[38,39], and organometallic complexes[40]. A new class of molecules which can be grouped together according to chemical structure are those based on a prototypical quinone derivative and is the main focus of this thesis[41].

Two broad categories into which all molecular switches can be placed is that of intrinsic or extrinsic[42]. Intrinsic switches are those which display switching behaviour before coupling to electrodes and continue to do so after coupling. Extrinsic switches are those which display no switching in their native state, but after coupling to the substrate show switching properties. Selecting molecular candidates with some form of active switching and then coupling to a metallic substrate with the hope that this switching will be retained is the most popular method, and this is reflected in the literature with most examples reported being intrinsic switches. Extrinsic switches are much less common due to the perceived difficulty in designing a composite electrode-molecule-electrode device which will be active only after coupling has taken place.

The switching mechanism can be classified into two general groups: conformational switches and charging/redox switches. The latter are molecules which accept or donate electrons to the attached electrodes, leading to a different charge state. Conformational switches are those which undergo some form of isomerisation resulting in a change of bonding or shape.

The stimulus used to induce switching can take many forms such as inelastic tunnelling[33], electric or magnetic field[43], mechanical manipulation[44], photon excitation[45], or thermal excitation[46]. In fact, for a given molecule, it may be possible to use more than one of these to induce a switch. However, the principle behind a two-state molecular switch is the same, regardless of the method of stimulation. This is illustrated in Figure 1.2 where we have two pathways to overcome the ground state activation barrier on the potential energy surface[42].

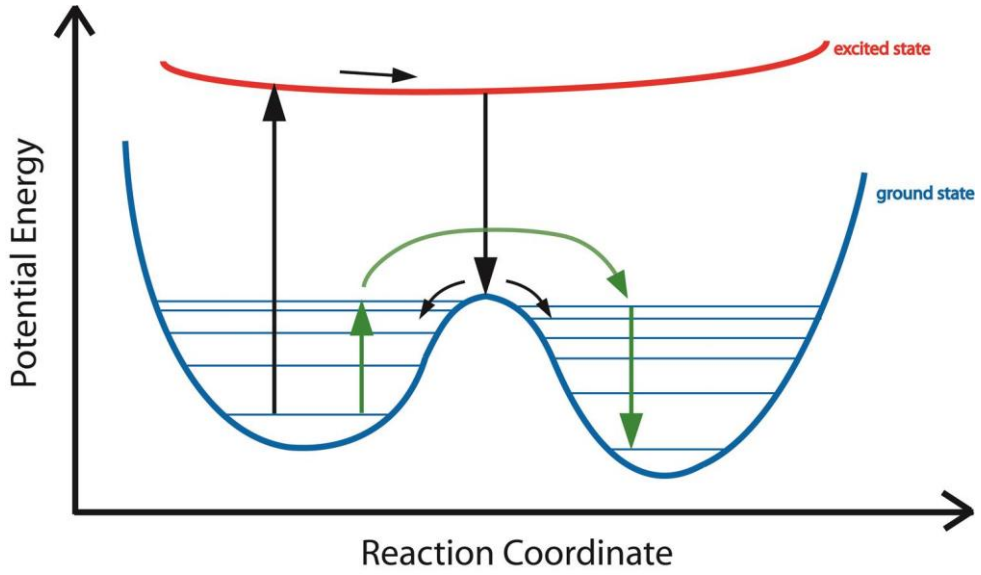

Figure 1.2 Schematic drawing of a potential energy diagram for a typical molecular switch. The two energy minima represent the stable states of the molecule and they can be accessed either by a vibrational ladder climbing mechanism (green arrows), or through relaxation from an excited state (black arrows).

The ground state has two local minima corresponding to the two stable forms of the molecule. In one case (for example, with photon excitation) the molecule reaches an excited state. This is followed by relaxation to one of the two ground state minima. Hence, there is a (not necessarily equal) probability for the molecule to relax to either the original state or to the switched state. The second reaction pathway is to remain in the ground state and simply overcome the activation barrier separating the two minima. This is the case, for example, with excitation of vibrational modes by inelastic tunnelling electrons (so-called vibrational heating). A third possibility (not indicated in Figure 1.2) in going from one state to the other is to tunnel through the barrier which separates them. The probability of this process decreases with

increased mass of the tunnelling object. However, observations atom tunnelling have been reported, for example, in tropolone[47].

A specific example is the aforementioned azobenzene molecule seen in Figure 1.3a. This molecule undergoes a reversible conformational change from *cis*- to *trans*-azobenzene and can be activated using an electric field[48], tunnelling electrons[49] or UV radiation[45]. Derivatives of this molecule have also been extensively studied and retain the isomeric switching property, provided that there is a weak interaction with the underlying substrate[50]. Within self-assembled domains, it is also possible to switch specific molecules. The large body of work behind azobenzene-type molecules illustrates their versatility as molecular switches. However, a rather unattractive feature is that the switch involves a radical change in the geometry of the molecular structure. This would cause obvious problems when connecting such a molecule across a junction in an electrical circuit.

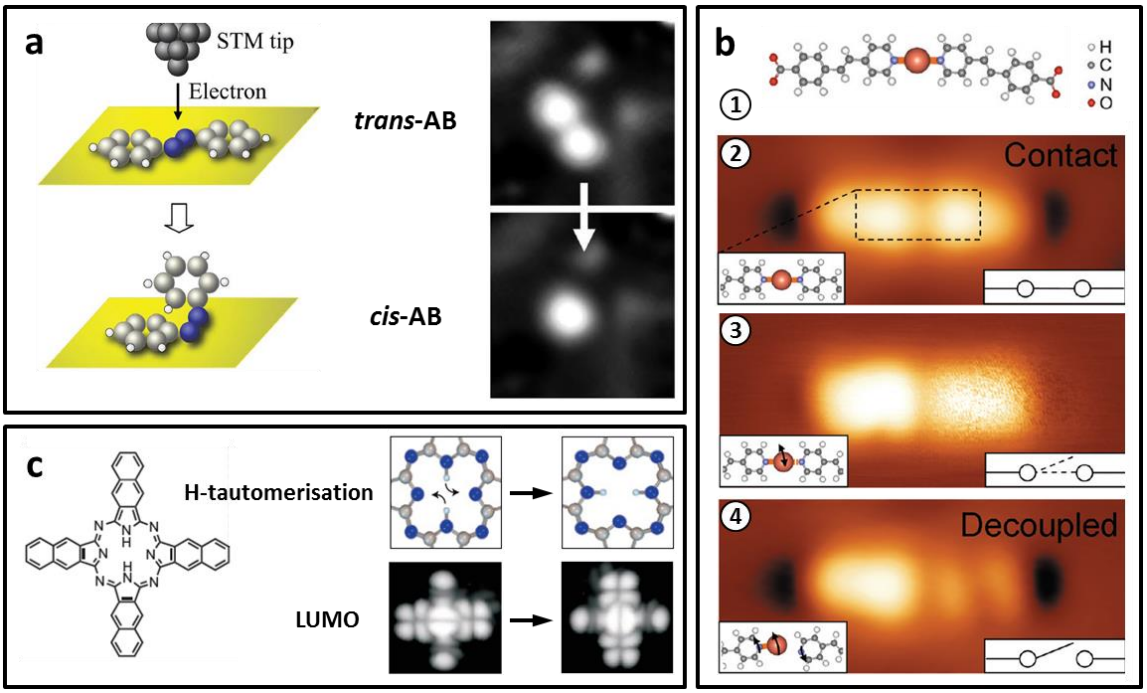

Figure 1.3 (a) *cis*-/*trans*- isomerisation of azobenzene (AB) induced by inelastic electron tunnelling[49]. Topographic images before and after the switch show a conformational change from planar (*trans*-AB) to upright (*cis*-AB). (b) Transitory metal-ligand bond cleavage and formation in a self-assembled complex[40]. 1: Chemical structure of $Cu[PVBA)_2$, 2: Intact complex, 3: Rapid switching induced by imaging at high voltge, 4: Cleaved complex. (c) H-tautomerisation in a naphthalocyanine molecule[33]. An asymmetry in the LUMO allows confirmation of the transfer of 2 H atoms located in the central molecular cavity.

The self-assembled switching complex $Cu[PVBA]_2$ (PVBA = 4-[*trans*-2-(pyrid-4-yl-vinyl)] benzoic acid) does not drastically change in shape and is a rare example of an extrinsic switch. Ohmann *et al*. showed that a metal-organic bond could be formed and broken by inelastic tunnelling

into the molecule[40]. The observable result of this is an electronic decoupling of the molecule leading to a decrease in the apparent STM height observed in one half of the complex (Figure 1.3b). By comparing complexes aligned along different crystallographic directions of the substrate (in this case Cu(111)) it was found that the preferred adsorption sites in the 'on' and 'off' states were responsible for the decoupling mechanism.

Charging/redox switches are difficult to study on metal surfaces due to stabilisation of charge by the substrate and hence quenching of any switching behaviour. It is, however, possible to study organic molecules of this type using STM by adsorption onto a thin insulating layer which electronically decouples the molecule and the substrate. For example, a NaCl bilayer is a common method of achieving decoupling while being sufficiently thin to allow tunnelling and hence imaging of the molecules. A recent study used this method to investigate the difference in conductance of charge states of *bis*-dibenzoylmethanato-copper molecules[51].

In a similar vein, using the same decoupling mechanism and a chemically similar molecule, it was found that tautomerisation of a pair of hydrogen (H) atoms in the central macrocycle system of naphthalocyanine leads to different conductance states (Figure 1.3c)[33]. This was the first reported example of a molecular switch which undergoes H-tautomerisation. The simple structural isomerism is equivalent to a 90° rotation of the molecule. While, in fact, only the central H atoms move, the molecular orbitals are rotated by 90° which leads to difference in conductivity. This was proved with beautiful STM images of HOMO and LUMO obtained by resonant tunnelling before and after the switch.

Further to this, a four-level switch was produced by using a similar system but removing one of the central protons by a controlled voltage pulse from the STM tip[52]. Another example of H-tautomerisation was seen in the structurally similar porphycene molecule[53,54]. These H-tautomeric switches are attractive in the field of molecular electronics because the energy required to induce a switch is low and the molecules do not significantly move or change shape, and hence will remain in contact with attached electrodes. The small number of reported examples using this switching mechanism is somewhat in conflict with the number of compounds which are known to undergo H-tautomerisation (in solution or gas-phase). This therefore exemplifies that careful consideration of both molecule and substrate is required to produce an active switch (as will be addressed in Chapters 4 and 5).

The molecules focussed on in this thesis are the first examples of H-tautomeric molecular switches which do not utilise the porphyrin moiety.

1.6 References

1. N. A. Peppas, J. Z. Hilt, A. Khademhosseini, and R. Langer, *Adv. Mater.*, 2006, **18**, 1345–1360.

2. E. Boisselier and D. Astruc, *Chem. Soc. Rev.*, 2009, **38**, 1759–1782.

3. W. Lu and C. M. Lieber, *Nat. Mater.*, 2007, **6**, 841–850.

4. E. Katz and I. Willner, *Angew. Chem. Int. Ed.*, 2004, **43**, 6042–6108.

5. N. A. Weir, D. P. Sierra, and J. F. Jones, *A Review of Research in the Field of Nanorobotics*, Sandia National Laboratories, Albuquerque, USA, 2005.

6. G. Binnig, R. Rohrer, C. Gerber, and E. Weibel, *Phys. Rev. Lett.*, 1982, **49**, 57–61.

7. R. J. Hamers, *J. Phys. Chem.*, 1996, **3654**, 13103–13120.

8. J. V. Barth, H. Brune, G. Ertl, and R. J. Behm, *Phys. Rev. B*, 1990, **42**, 9307–9318.

9. G. Binnig, R. Rohrer, C. Gerber, and E. Weibel, *Phys. Rev. Lett.*, 1983, **50**, 120–123.

10. A. Aviram and M. A. Ratner, *Chem. Phys. Lett.*, 1974, **29**, 277–283.

11. C. J. Baddeley, *Top. Catal.*, 2003, **25**, 17–28.

12. M.-L. Bocquet and A. Michaelides, in *Properties of Single Organic Molecules on Crystal Surfaces*, eds. P. Grutter, W. Hofer, and F. Rosei, Imperial College Press, London, 2006, pp. 389–424.

13. J. Greeley, J. K. Nørskov, and M. Mavrikakis, *Annu. Rev. Phys. Chem.*, 2002, **53**, 319–348.

14. D. Vuillaume, *C. R. Acad. Sci.*, 2008, **9**, 78–94.

15. R. Schaub, E. Wahlström, A. Rønnau, E. Lagsgaard, I. Stensgaard, and F. Besenbacher, *Science*, 2003, **299**, 377–379.

16. J. S. Foord, P. J. Goddard, and R. M. Lambert, *Surf. Sci.*, 1980, **94**, 339–354.

17. P. A. Thiel and T. E. Madley, *Surf. Sci. Rep.*, 1987, **7**, 211–385.

18. M. Lorenzo, C. Baddeley, C. Muryn, and R. Raval, *Nature*, 2000, **404**, 376–379.

19. C. Shen, I. Cebula, C. Brown, J. Zhao, M. Zharnikov, and M. Buck, *Chem. Sci.*, 2012, **3**, 1858–1865.

20. J. V. Barth, *Surf. Sci.*, 2009, **603**, 1533–1541.

21. F. Ullmann, G. M. Meyer, O. Loewenthal, and O. Gilli, *Liebigs Ann.*, 1904, **331**, 38.

22. S. Hla, L. Bartels, G. Meyer, and K. Rieder, *Phys. Rev. Lett.*, 2000, **85**, 2777–2780.

23. J. I. Pascual, N. Lorente, Z. Song, H. Conrad, and H.-P. Rust, *Nature*, 2003, **423**, 525–528.

24. N. Lin, A. Dmitriev, J. Weckesser, J. V Barth, and K. Kern, *Angew. Chem. Int. Ed.*, 2002, **41**, 4779–4783.

25. L. Grill, M. Dyer, L. Lafferentz, M. Persson, M. V Peters, and S. Hecht, *Nature Nanotechnol.*, 2007, **2**, 687–691.

26. J. Bardeen and W. H. Brattain, *Phys. Rev.*, 1948, **74**, 230–231.

27. A. S. Martin, J. R. Sambles, and G. J. Ashwell, *Phys. Rev. Lett.*, 1993, **70**, 218–221.

28. R. M. Metzger, *J. Mater. Chem.*, 2008, **18**, 4364–4396.

29. W. Liang, M. P. Shores, M. Bockrath, J. R. Long, and H. Park, *Nature*, 2002, **417**, 725–729.

30. L. A. Bumm, J. J. Arnold, M. T. Cygan, T. D. Dunbar, T. P. Burgin, L. Jones II, D. L. Allara, J. M. Tour, and P. S. Weiss, *Science*, 1996, **271**, 1705–1707.

31. J. H. Burroughes, D. D. C. Bradley, A. R. Brown, R. N. Marks, K. Mackay, R. H. Friend, P. L. Burns, and A. B. Holmes, *Nature*, 1990, **347**, 539–541.

32. M. Alemani, M. V Peters, S. Hecht, K.-H. Rieder, F. Moresco, and L. Grill, *J. Am. Chem. Soc.*, 2006, **128**, 14446–14447.

33. P. Liljeroth, J. Repp, and G. Meyer, *Science*, 2007, **317**, 1203–1206.

34. C. Toher, D. Nozaki, G. Cuniberti, and R. M. Metzger, *Nanoscale*, 2013, **5**, 6975–6984.

35. F. Moresco, *Phys. Rep.*, 2004, **399**, 175–225.

36. D. M. Eigler, C. P. Lutz, and W. E. Rudge, *Nature*, 1991, **352**, 600–603.

37. T. M. Wallis, X. Chen, and W. Ho, *J. Chem. Phys.*, 2000, **113**, 4837–4839.

38. C. P. Collier, E. W. Wong, M. Belohradsky, F. M. Raymo, J. F. Stoddart, P. J. Keukes, R. S. Williams, and J. R. Heath, *Science*, 1999, **285**, 391–394.

39. Y.-L. Zhao, W. R. Dichtel, A. Trabolsi, S. Saha, I. Aprahamian, and J. F. Stoddart, *J. Am. Chem. Soc.*, 2008, **130**, 11294–11296.

40. R. Ohmann, L. Vitali, and K. Kern, *Nano Lett.*, 2010, **10**, 2995–3000.

41. G. J. Simpson, S. W. L. Hogan, M. Caffio, C. J. Adams, H. Früchtl, T. van Mourik, and R. Schaub, *Nano Lett.*, 2014, **14**, 634–639.

42. S. Jan van der Molen and P. Liljeroth, *J. Phys.: Condens. Matter*, 2010, **22**, 133001.

43. X. H. Qiu, G. V. Nazin, and W. Ho, *Phys. Rev. Lett.*, 2004, **93**, 1–4.

44. F. Moresco, G. Meyer, K.-H. Rieder, H. Tang, A. Gourdon, and C. Joachim, *Phys. Rev. Lett.*, 2001, **86**, 672–675.

45. M. Comstock, N. Levy, A. Kirakosian, J. Cho, F. Lauterwasser, J. Harvey, D. Strubbe, J. Fréchet, D. Trauner, S. Louie, and M. Crommie, *Phys. Rev. Lett.*, 2007, **99**, 1–4.

46. P. Gutlich, A. Hauser, and H. Spiering, *Angew. Chem. Int. Ed.*, 1994, **33**, 2024–2054.

47. R. L. Redington, *J. Chem. Phys.*, 1990, **92**, 6447.

48. M. Alemani, M. V Peters, S. Hecht, K.-H. Rieder, F. Moresco, and L. Grill, *J. Am. Chem. Soc.*, 2006, **128**, 14446–14447.

49. B.-Y. Choi, S.-J. Kahng, S. Kim, H. Kim, H. Kim, Y. Song, J. Ihm, and Y. Kuk, *Phys. Rev. Lett.*, 2006, **96**, 1–4.

50. M. Alemani, S. Selvanathan, F. Ample, M. V. Peters, K.-H. Rieder, F. Moresco, C. Joachim, S. Hecht, and L. Grill, *J. Phys. Chem. C*, 2008, **112**, 10509–10514.

51. T. Leoni, O. Guillermet, H. Walch, V. Langlais, A. Scheuermann, J. Bonvoisin, and S. Gauthier, *Phys. Rev. Lett.*, 2011, **106**, 4–7.

52. W. Auwärter, K. Seufert, F. Bischoff, D. Ecija, S. Vijayaraghavan, S. Joshi, F. Klappenberger, N. Samudrala, and J. V Barth, *Nat. Nanotechnol.*, 2012, **7**, 41–46.

53. T. Kumagai, F. Hanke, S. Gawinkowski, J. Sharp, K. Kotsis, J. Waluk, M. Persson, and L. Grill, *Phys. Rev. Lett.*, 2013, **111**, 246101.

54. T. Kumagai, F. Hanke, S. Gawinkowski, J. Sharp, K. Kotsis, J. Waluk, M. Persson, and L. Grill, *Nat. Chem.*, 2014, **6**, 41–46.

2 Methods

This chapter outlines the methods used for the work presented in this thesis, namely scanning tunnelling microscopy (STM) and density functional theory (DFT). STM is given more emphasis as this was the technique used for collection of all experimental data; DFT optimisations were used to calculate the most favourable configuration of molecules on a surface, and hence, helped to rationalise the STM data. STM experiments were conducted by myself, and DFT calculations were performed in close collaboration with colleagues at the University of St Andrews.

2.1 Scanning Tunnelling Microscopy

Since its invention[1,2] in 1981 at the IBM labs in Zurich, Switzerland, STM has been established as a powerful technique for probing surfaces at the local scale. The principle of its operation relies on precise control of a conducting probe tip separated by a few Ångströms from a conducting sample. When close in space, the wavefunctions of the probe and the surface overlap sufficiently to allow electrons to quantum mechanically tunnel through the vacuum gap that separates them.

With application of a bias to one of these two electrodes, a tunnel current is established, which is generally on the order of pA to nA. Measurement of this current, as the tip is raster scanned with precision control over an area of the surface, allows a real-space image of the surface to be obtained. The precise control of the tip is achieved using piezoelectric elements in the *x*, *y*, and *z* directions, and allows resolution as low as 0.1 Å laterally, and 0.01 Å vertically.

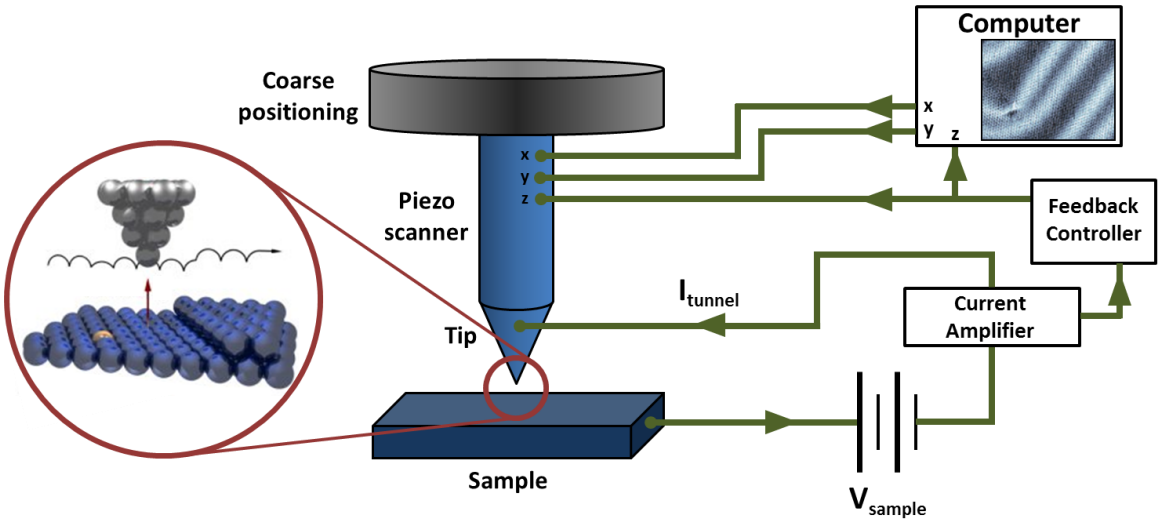

Figure 2.1 Schematic drawing of a scanning tunnelling microscope (modified from refs [3,4]). The tip is brought to within a few Ångtröms of the biased sample by the course positioning device. The tunnel current, I_{tunnel}, is measured and used to regulate the tip height using the feedback controller.

A schematic drawing of an STM is shown in Figure 2.1. Topographic imaging is usually conducted in the constant-current mode. This uses an electronic feedback system to regulate the tunnel current at a constant set-point value, by moving the tip with respect to the surface (*z* direction) as it moves across the surface (*x* and *y* directions). Atomically resolved images can be routinely acquired in this manner with reduced risk of a tip crash.

Theory

As stated above, the process of quantum tunnelling is key to the operation of STM. The simplest example to consider is the single particle tunnelling through a rectangular potential energy barrier, as shown in Figure 2.2. Classically, if the particle does not possess sufficient energy, the barrier is insurmountable, and the particle remains in region **a**. However, in the quantum regime, where the particle (e.g. an electron) is small (compared to its de Broglie wavelength), it can be considered as both a particle and a wave. For particle energies lower than that of the barrier ($E < V_0$), there is a non-zero probability that the particle can traverse region **b** to reach region **c**. This is known as tunnelling, and will be briefly explained here before going on to describe the theory and practicalities of STM imaging and spectroscopy.

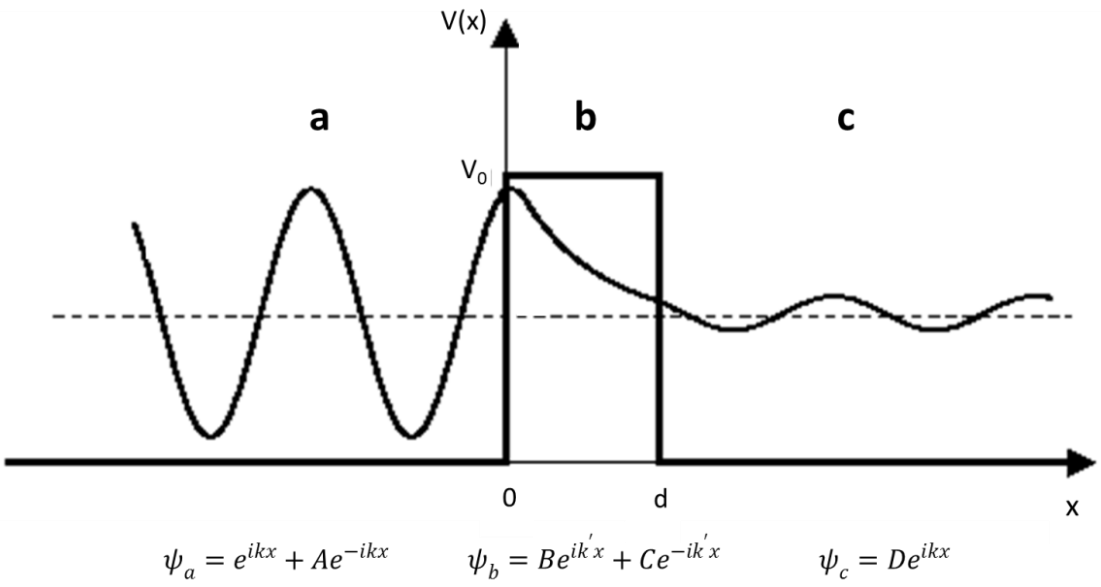

Figure 2.2 Quantum tunnelling through a rectangular potential energy barrier.

Electron Tunnelling

For the simple time-independent, one-dimensional case depicted in Figure 2.2, the regions **a**, **b**, and **c** are described by the wavefunctions ψ_a, ψ_b, and ψ_c, respectively. The Schrödinger equations for an electron travelling along the *x* direction in the three regions can be written:

Region **a**:

$$-\frac{\hbar^2}{2m}\frac{d^2\psi_a}{dx^2} = E\psi_a$$

$$\psi_a = e^{ikx} + Ae^{-ikx}$$

$$k = \sqrt{\frac{2mE}{\hbar^2}}$$

where *A* represents the reflected amplitude of the incoming electron with wavenumber *k*.

Region **b**:

$$-\frac{\hbar^2}{2m}\frac{d^2\psi_b}{dx^2} + V_0\psi_b = E\psi_b$$

$$\psi_b = Be^{ik'x} + Ce^{-ik'x}$$

$$k' = \sqrt{\frac{2m(V_0 - E)}{\hbar^2}}$$

where the first term of the wavefunction is the forward travelling component inside the barrier and the second is the reflected component at the boundary at position *d*.

Region **c**:

$$-\frac{\hbar^2}{2m}\frac{d^2\psi_c}{dx^2} = E\psi_c$$

$$\psi_c = De^{ikx}$$

where *D* is the amplitude of the transmitted electron.

For the case where $E < V_0$ (i.e. the classically forbidden case) we see that we have a non-zero transmission probability, *T*:

$$T = \frac{1}{1 + \frac{V_0 \sinh^2(k'd)}{4E(V_0 - E)}}$$

Outside the barrier, the wavefunction oscillates with wavevector *k*, but inside the barrier the wavefunction decays exponentially. Hence, if the barrier width, *d*, is large, the wavefunction decays significantly so that regions **a** and **b** are essentially independent and tunnelling does not occur.

In the limit where the wavelength of the electron is much smaller than the width of the barrier ($1/k' << d$), the above equation reduces to:

$$T \approx ce^{-2k'd}$$

$$c = \frac{-16k^2k'^2}{(k^2 - k'^2)^2}$$

From this we can see that the transmission probability, and hence the tunnel current in the case of STM, is dominated by the strong exponential dependence on the barrier width. So for a barrier width of 5 Å and a barrier height of 4 eV (typical values for tip-sample separation and workfunction in STM experiments), a change in barrier width of just 1 Å leads to an order of magnitude change in *T*.

This high sensitivity was the basis of Binnig and Rohrer's conception of an instrument which would provide very high spatial resolution of a conducting surface. The above description is true for the one-dimensional case. Extension of this to a barrier of arbitrary shape was formalised in 1926 by Wenzel, Kramers, and Brillouin using their eponymous WKB approximation[5].

STM Imaging

STM imaging considers a three dimensional system: a metallic tip in close proximity to a conductive surface. The "wave-matching" description of quantum tunnelling described above becomes extremely cumbersome when extended to such a system. Bardeen's approach[6] uses the time-dependent Schrödinger equation and Fermi's golden rule from perturbation theory to describe the tunnel current as:

$$I = \frac{2\pi e}{\hbar}\sum_{\mu,\nu}\{f(E_\mu)[1-f(E_\nu+eU)]-f(E_\nu+eU)[1-f(E_\mu)]\}.|M_{\mu\nu}|^2\delta(E_\nu-E_\mu)$$

where *f(E)* is the Fermi function, *U* is the bias voltage applied, E_μ and E_ν are the energies of states of the tip (ψ_μ) and surface (ψ_ν), respectively, and $M_{\mu\nu}$ is the tunnelling matrix element. The calculation boils down to the evaluation of this matrix element which is determined by the states of the tip and sample and their separation (the integral is over any plane in the barrier region):

$$M_{\mu\nu} = \frac{-\hbar^2}{2m}\int d\boldsymbol{S}\left(\psi_\mu^*\,\boldsymbol{\nabla}\psi_\nu - \psi_\nu\boldsymbol{\nabla}\psi_\mu^*\right)$$

The structure of the surface is generally known due to well characterised surfaces being used. The state of the tip, however, is generally unknown. Under the assumption that, for an arbitrarily shaped tip, the most extreme point is locally spherical, Tersoff and Hamann[7,8] approximated the tip with a s-function. This is appropriate for most cases because, provided the tip is terminated with a single atom, 90% of the current tunnels though this atom. Hence, for a tip at position $\boldsymbol{r} = \boldsymbol{r_0}$ with radius of curvature *R*, its wavefunction is:

$$\psi_\mu = \Omega_t^{-\frac{1}{2}} c_t k' R e^{k'R} e^{-k'|r-r_0|}(k'|\boldsymbol{r}-\boldsymbol{r_0}|)^{-1}$$

where *k'* is as defined above, c_t is a normalisation factor, and Ω_t is the volume of the tip. The matrix element, $M_{\mu\nu}$, therefore becomes:

$$M_{\mu\nu} = \frac{2\pi\hbar^2}{mk'}\Omega_t^{-\frac{1}{2}}k'Re^{k'R}\psi_\nu(\boldsymbol{r_0})$$

i.e. a function dependent only on the wavefunction of the sample.

Using the Tersoff-Hamann approximation we therefore finally arrive at an expression for the tunnel current in terms of the states of the surface:

$$I \propto \exp(2\varkappa R)\sum_\nu |\psi_\nu(\boldsymbol{r_0})|^2 \cdot \delta(E_\nu - E_F) \qquad \varkappa = \frac{2m\phi}{\hbar}$$

where $\varkappa$ is the decay rate, φ is the local potential barrier height, and E_F is the Fermi energy. The summation in this expression can be identified as the local density of states (LDOS) of the surface evaluated directly below the STM tip. Since this is dependent on the wavefunction and, from the time-independent approach, we know that this decays exponentially as a function of the barrier width, *d*, we return to the previous expression for tunnel current:

$$I \propto e^{-2\varkappa d}$$

From this approach, we have determined that, at the position of the tip, the current is a measure of the LDOS. Hence, as the tip is moved laterally across the surface, while keeping the current constant, we can map out the contours of constant LDOS and, in this way produce an STM image.

The two most common methods for STM imaging are constant height and constant current imaging. The former, which is less commonly used, involves scanning the tip across the surface without adjusting its height. Variation in the measured current as the tip moves over features of differing heights provides the contrast seen in the image. The main disadvantage, and reason for its unpopularity, is that there is a risk of a tip crash if there are large variations in height. In contrast, constant current imaging, which provides much the same information, uses a feedback loop to maintain the current at a set value by varying the height of the tip as it scans over the surface. The measured height of the tip therefore provides contrast visible in the STM image. During imaging, precise control of the probe both laterally (*x*-*y* plane) and vertically (*z*) is required.

Various methods for sub-Ångström control of the tip position exist, including magnetic positioning[9,10], mechanical positioning[11,12] and piezoelectric positioning devices[13–15]. Piezoelectric devices employ three piezoelectric elements in the three dimensions *x*, *y* and *z*. They afford the best control and precision, and therefore are most commonly used in STM.

The piezoelectric effect is the reversible change in the physical dimensions of a material in response to an externally applied electric field. For a piezoelectric tube of length *l* and wall thickness *h*, the change in length, *Δl*, upon application of a voltage *U* is given by:

$$\Delta l = d\frac{l}{h}U$$

where *d* is the piezoelectric coefficient particular to the material. Hence, using a high voltage amplifier to apply voltage pulses to the *x* and *y* piezoelements, the tip may be raster scanned over the surface.

In terms of the practicalities of scanning, it is desirable to have piezoelectric devices capable of large changes in length (to allow large scan areas), while maintaining a high sensitivity (high resolution). It is also important to have elements with high resonance frequencies so that, when scanning, coupling to the scan frequency does not occur, which would result in superimposed noise appearing in the images. Finally, it is important to design piezoelectric scanners which have low thermal drift, low creep/hysteresis and little cross-talk between the *x*, *y*, *z* elements.

In order for the tunnel current to be recorded by a computer, and allow constant current imaging, an electronic unit and feedback control are required. Since the measured current is so small, a preamplifier is used to convert the signal to a voltage, the gain of which is typically 10^6 – 10^9 V A^{-1}. After the tunnel current is measured and the current set-point is chosen by the user, the feedback amplifiers compare the two values and send a voltage signal to the z piezoelement. This induces a change in the height of the tip in order to keep the current signal constant.

2.2 Scanning Tunnelling Spectroscopy

In addition to imaging, a range of spectroscopic modes are available using the scanning tunnelling microscope. Spectroscopy involves, for example, the measurement of the tunnel current (*I*) while another parameter, e.g. the bias (*V*) or the tip-sample separation (*Z*), is varied. The information obtained depends on which parameters are measured/varied. The technique allows spectroscopic measurement at the extreme local scale, and can provide information on individual species which would otherwise be unavailable using ensemble techniques such as infra-red spectroscopy.

The various different modes come from the fact that the three STM variables *I*, *V* and *Z*, and their derivatives (e.g. d*I*/d*V*, d^2I/dV^2, d*Z*/d*V*,…) can be measured. For a full overview of the different spectroscopic modes of STM see reference[16]. The three most commonly used modes are *I*/*V* and its first and second derivatives d*I*/d*V* and d^2I/dV^2. From these, one can extract information on the conductance, the electronic structure, and the vibrational structure of a sample, respectively. d*I*/d*V* spectroscopy is commonly referred to simply as scanning tunnelling spectroscopy (STS); d^2I/dV^2 is referred to a inelastic electron tunnelling spectroscopy (IETS).

The following section will outline the principle of these techniques. Although conventional spectroscopy is not used in the present work, inelastic electron tunnelling is the reason for switching in the molecules studied. Accordingly, a full description of inelastic tunnelling will also be given.

Spectroscopic measurements are implemented with an STM by disabling the feedback control in order to keep the tunnel gap constant, and then measuring the tunnel current while a voltage ramp is applied. This gives a conductance spectrum (*I*/*V*). Information on the LDOS of the sample can be obtained from the differential signal, d*I*/d*V*, for example the energies of the frontier orbitals of molecular adsorbates. The differential signal can be interpreted from the WKB approximation shown below:

$$\frac{dI}{dV} = \rho_s(\boldsymbol{r}, eV)\rho_t(\boldsymbol{r}, 0)T(E, eV, \boldsymbol{r}) + \int_0^{eV} \rho_s(\boldsymbol{r}, E)\rho_t(\boldsymbol{r}, E - eV)\frac{dT(E, eV, \boldsymbol{r})}{dV}dE$$

We can see that both terms contain the transmission probability, *T*, which varies as a function of voltage. The second term gives a background signal upon which the first term is superimposed. The first term is dependent on the density of states of the surface, and this is why features in the spectrum can be interpreted as variations in the LDOS. Such spectra can be obtained experimentally either by numerical differentiation of the I/V curve, or directly by using lock-in techniques. For the second case, a small modulation is applied to the sample bias, and the resultant modulation in I is measured as the voltage sweep is performed[17]. This modulation frequency should be outside the range of the resonances of the electronics and the instrument to allow spectra of high resolution to be acquired.

d*I*/d*V* imaging is also possible by recording the differential spectrum at each pixel in a topographic image. This is achieved by collecting a constant-current image (feedback switched on) in the normal manner, but interrupting the scan to perform a spectrum (with the feedback

switched off) at each point in the image. The result is a very rich data-set from which spatially resolved images of molecular resonances can be produced[18]. However, care must be taken in interpretation because the signal not only depends on the LDOS, but also the transmission probability, *T*, which is not necessarily constant over the whole sample.

Inelastic Tunnelling Spectroscopy

While d*I*/d*V* spectroscopy provides information on the electronic structure of the sample, d^2I/dV^2 spectroscopy provides information on the vibrational structure of the surface[19]. Until now, only elastic tunnelling has been considered where the energy of tunnelling electrons is conserved. In inelastic tunnelling the electron energy is increased or decreased following interaction with vibrational modes (phonons or molecular vibrations). The process is drawn schematically in Figure 2.3a.

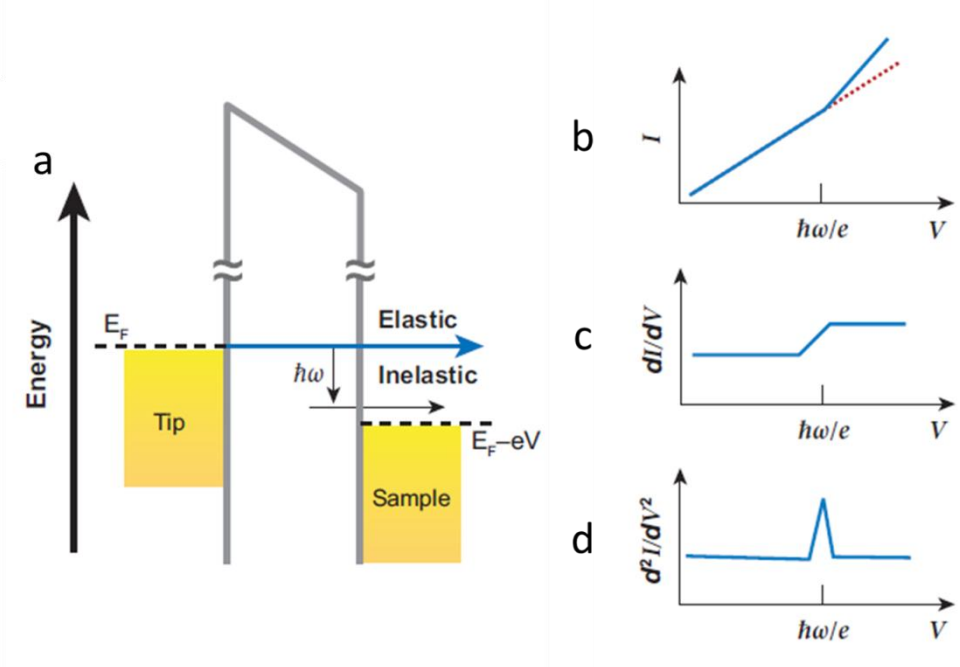

Figure 2.3 Inelastic electron tunnelling. (a) Energy level diagram for inelastic tunnelling from tip to sample. (b) Current vs. voltage measurement of conductance. (c) Differential conductance measuring the LDOS. (d) Second order differential conductance measuring molecular vibrations. Modified from reference[20].

Upon sweeping the bias from zero to a value *V*, electrons will tunnel elastically from the tip to the unfilled states of the surface. When the bias reaches a threshold of $\hbar\omega_0/e$, corresponding to the energy of a vibrational mode, an inelastic channel becomes available through which electrons can tunnel. Prior to this bias, this state is occupied and, due to the Pauli exclusion

principle, is unavailable for electrons to tunnel into it. During the inelastic tunnelling process the electron loses a quantum of energy $\hbar\omega_0$ to the mode.

This extra channel, through which electrons can tunnel, is seen in the *I*/*V* curve as an increase in the gradient at the position of the bias threshold, as seen in Figure 2.3b. This becomes a step in the differential conductance spectrum (Figure 2.3c). As the portion of inelastically scattered electrons is only 0.1-1% of those tunnelling elastically, the step is very small. It is therefore necessary to measure the second derivative of the current which displays a peak at the voltage corresponding to the inelastic channel (Figure 2.3d). As the bias voltage is increased still further, more peaks appear, corresponding to further inelastic channels and hence further vibrational modes of the surface. In this way, a vibrational spectrum of the sample can be built up.

IET spectra can be used to identify the chemical structure of molecules in the same way as other vibrational spectroscopies (infra-red and Raman). The complementary photon-based techniques have differing selection rules, meaning that a combination of the two techniques is required to identify all of the vibrational modes of a system. Unlike these techniques, IET spectral features do not arise from the field-dipole interaction but rather from vibronic modification of the electronic levels[21]. Therefore IETS does not have such strict selection rules and peaks corresponding to both infra-red and Raman active modes can be obtained from this method.

One of the main advantages of IETS is that, using a carefully positioned STM tip, one can gather information on single bonds within a molecule. The inherently local nature of this technique means that the sample size is often a single molecule, and the intensity of the peaks is therefore of the order of a picoamp. For this reason, it is necessary to conduct experiments at cryogenic temperatures, with good vibration isolation, and long integration times to get spectral resolution that compares with the aforementioned ensemble techniques.

2.3 Density Functional Theory

Density functional theory (DFT) is a computational method used to theoretically model many electron systems by determining their ground state properties[22]. The work presented in this thesis uses DFT in many cases to substantiate reaction mechanisms and chemical structure hypotheses. The method complements chemically insensitive STM data well, to allow correct

interpretation of images. Through discussion and collaboration with colleagues at the University of St Andrews, models were formulated and optimised using DFT methods. The calculations were performed by our in-house collaborators and the results are discussed along with the STM data. The background of DFT is therefore presented to give the reader a better understanding of these discussions.

Any many-bodied system of interacting particles can, in principle, be described by the time-independent Schrödinger equation:

$$\hat{\mathrm{H}}\Psi(\mathbf{r}_1, \mathbf{r}_2, \ldots, \mathbf{r}_n) = E\Psi(\mathbf{r}_1, \mathbf{r}_2, \ldots, \mathbf{r}_n)$$

where $\hat{\mathrm{H}}$ is the Hamiltonian operator, which contains terms for the kinetic energy, the electrostatic potential, and the interaction between electrons. Ψ is the wavefunction and contains all of the information on the physical state of the system. For a system with two electrons, the equation may be solved analytically, but for even one extra electron, the problem becomes extremely difficult because of the correlation of the individual electronic wavefunctions. Hence, for a many electron system, a series of approximations must be made to make the calculation feasible. The first such approximation is the Born-Oppenheimer approximation. This states that the nuclei can be treated as having fixed positions and the electrons are free to move.

Further approximations, in conjunction with computationally expensive methods such as Hartree-Fock, allow the above Schrödinger equation to be solved. DFT, however, uses a different approach. Instead of grappling with a complicated, many-variable wavefunction, Hohenberg and Kohn[23] replaced it with the electron density $n(\mathbf{r})$. The ground state energy, E, of a system can then be expressed in terms of a functional of this quantity $G[n]$, and the total external potential $v(\mathbf{r})$:

$$E = \int n(\mathbf{r})v(\mathbf{r})\, d\mathbf{r} + \frac{1}{2}\iint \frac{n(\mathbf{r})n(\mathbf{r}')}{|\mathbf{r} - \mathbf{r}'|} d\mathbf{r}d\mathbf{r}' + G[n]$$

In doing this, the problem is reduced from a 3n variable problem, to a problem with just three spatial coordinates. Based on this, Kohn and Sham[24] split the functional into a kinetic term, T, and an exchange-correlation term, E_{xc}, and formulated a series of single electron Schrödinger equations:

$$(T + E_{xc})\phi_i(\mathbf{r}) = \epsilon_i\phi_i(\mathbf{r})$$

The electron density is determined from these “Kohn-Sham” equations by:

$$\sum_i |\phi_i(\mathbf{r})|^2 = n(\mathbf{r})$$

These equations are iteratively solved during a DFT calculation starting from a guess for $n(\mathbf{r})$ until self-consistency is achieved.

Approximations have to be made for the exchange-correlation term as this is not known exactly. The most common approximations are the local density approximation (LDA), and the generalised gradient approximation (GGA)[25]. LDA treats the electrons as being homogeneously spread out, and calculates E_{xc} for this simplified case. It works well for systems with slowly varying electron densities. GGA improves on this by introducing a term to describe the gradient of the density, but can also lead to inaccuracies if the gradient is too steep.

Due to its simplicity and reduced computational cost compared to *ab-initio* methods, DFT has found popularity in many fields of research. Development of functionals such as B3LYP[26,27] and PBE[28] to describe discrete systems, as well as extended periodic systems, means that DFT simulation, followed by comparison with empirical data, has become routine. There are many software packages which are capable of implementing DFT methods including: Vienna *Ab-Initio* Simulation Package (VASP), Spanish Initiative for Electronic Simulations with Thousands of Atoms (SIESTA), Gaussian, and Cambridge Serial Total Energy Package (CASTEP). Depending on the system under consideration, the choice of which package to use will affect the accuracy and computational speed of the calculations. For example, Gaussian is optimised for calculations of discreet systems, and so works well for gas phase species; SIESTA uses atom centred basis-sets which reduce the computational expense, and so works well on systems with large numbers of atoms. The package used for the surface-based calculations addressed in this thesis is VASP, which uses a plane wave basis set and performs accurate optimisation on periodic systems.

2.4 References

1. G. Binnig, R. Rohrer, C. Gerber, and E. Weibel, *Phys. Rev. Lett.*, 1982, **49**, 57–61.
2. G. Binnig, R. Rohrer, C. Gerber, and E. Weibel, *Appl. Phys. Lett.*, 1982, **40**, 178–180.
3. S. Woedtke, Christian Albrechts Universität, Kiel, 2002.
4. R. J. Hamers, *J. Phys. Chem.*, 1996, **3654**, 13103–13120.

5. D. Bonnell, *Scanning Probe Microscopy and Spectroscopy: Theory, Techniques, and Applications*, Wiley-VCH, New York, 2001.

6. J. Bardeen, *Phys. Rev. Lett.*, 1961, **6**, 57–59.

7. J. Tersoff and D. R. Hamann, *Phys. Rev. Lett.*, 1983, **50**, 1998–2001.

8. J. Tersoff and D. R. Hamann, *Phys. Rev. B*, 1985, **31**, 805–813.

9. D. P. E. Smith and S. A. Elrod, *Rev. Sci. Instrum.*, 1985, **56**, 1970–1971.

10. B. W. Corb, M. Ringger, and H.-J. Güntherodt, *J. Appl. Phys.*, 1985, **58**, 3947–3953.

11. D. P. E. Smith and G. Binnig, *Rev. Sci. Instrum.*, 1986, **57**, 2630–2631.

12. J. E. Demuth, *Journal of Vacuum Science & Technology A: Vacuum, Surfaces, and Films*, 1986, **4**, 1320–1323.

13. G. Binnig and R. Rohrer, *Helv. Chim. Acta*, 1982, **55**, 726–735.

14. H. J. Mamin, D. W. Abraham, E. Ganz, and J. Clarke, *Rev. Sci. Instrum.*, 1985, **56**, 2168–2170.

15. K. Uozumi, K. Nakamoto, and K. Fujioka, *Jpn. J. Appl. Phys.*, 1988, **27**, L123–L126.

16. R. Wiesendanger, *Scanning Probe Microscopy and Spectroscopy*, Cambridge University Press, Cambridge, 1994.

17. G. Binnig, K. H. Frank, H. Fuchs, N. Garcia, B. Riehl, H. Rohrer, F. Salvan, and A. R. Williams, *Phys. Rev. Lett.*, 1985, **55**, 991–994.

18. W.-H. Soe, C. Manzano, A. De Sarkar, N. Chandrasekhar, and C. Joachim, *Phys. Rev. Lett.*, 2009, **102**, 176102.

19. T. Komeda, *Prog. Surf. Sci.*, 2005, **78**, 41–85.

20. A. M. Moore and P. S. Weiss, *Annu. Rev. Anal. Chem.*, 2008, **1**, 857–882.

21. A. Troisi and M. a Ratner, *Nano Lett.*, 2006, **6**, 1784–1788.

22. R. G. Parr and W. T. Yang, *Density Functional Theory of Atoms and Molecules*, Oxford University Press, Oxford, 1994.

23. P. Hohenberg and W. Kohn, *Phys. Rev.*, 1964, **136**, B864–B871.

24. W. Kohn and L. J. Sham, *Phys. Rev.*, 1965, **140**, A1133–A1138.

25. C. J. Cramer, *Essential of Comutational Chemistry: Theories and Models*, Wiley, Chichester, UK, 2nd edn., 2002.

26. A. D. Becke, *J. Chem. Phys.*, 1993, **98**, 5648–5652.

27. P. J. Stephens, F. J. Devlin, C. F. Chabalowski, and M. J. Frishch, *J. Phys. Chem.*, 1994, **98**, 11623–11627.

28. J. P. Perdew, K. Burke, and M. Ernzerhof, *Phys. Rev. Lett.*, 1996, **77**, 3865–3868.

3 Experimental Methods

3.1 Summary

This chapter describes the experimental methods used during the course of the PhD. The STM instrumentation is detailed in full, as well as the procedures used to prepare the metallic surfaces, probe tips, and deposition of molecules. The computational infrastructure, used to perform DFT calculations, is also reported.

3.2 The CreaTec LT-STM System

The entirety of the experimental data acquired during this project involved the use of the commercially available low-temperature scanning tunnelling microscope (LT-STM) from CreaTec. CreaTec is an established manufacturer of highly customised and application oriented systems for use in ultrahigh vacuum (UHV), and are headquartered in Erligheim, Germany. Many of their systems are designed in close collaboration with leading research institutions, and indeed, the LT-STM was developed during the PhD project of Sven Zöphel in the group of Karl-Heinz Rieder at the Free University of Berlin[1]. The system used for the current work was commissioned in August 2008, in St Andrews, by the group of Renald Schaub as part of the foundation of the Scottish Centre for Interdisciplinary Surface Spectroscopy (SCISS). Compared to its manufacturer specification, the LT-STM has been modified in a number of ways in order to achieve more efficient use of the system, and the following chapter will go on to describe the full experimental set-up in detail.

3.2.1 UHV system

When studying surfaces at the atomic level, extreme control of the environment is required to ensure that external pollutant species do not affect the behaviour of the system of interest. For this reason, the system is held under UHV so that a sample can be prepared *in vacuo*, and remain clean for an extended period of time to allow measurements to be made. For example, the surface of a reactive substrate would be completely saturated with molecules after a few nanoseconds (assuming that the gas molecules have a sticking coefficient of 1), whereas at a

pressure of 1×10^{-11} mbar, monolayer coverage would occur only after a minimum of 28 hours. Often, this time is much greater when working with relatively unreactive systems. Since the typical time required to conduct an experiment can be as short as 1 hour or as long as 24 hours, the surface remains free of contamination long enough to acquire data.

An overview of the vacuum system is shown in Figure 3.1; the main sections and components are annotated. The system is composed of three main sections: the STM chamber, the preparation (prep) chamber, and the turbo pumping stage. These three sections can be isolated from each other using gate valves.

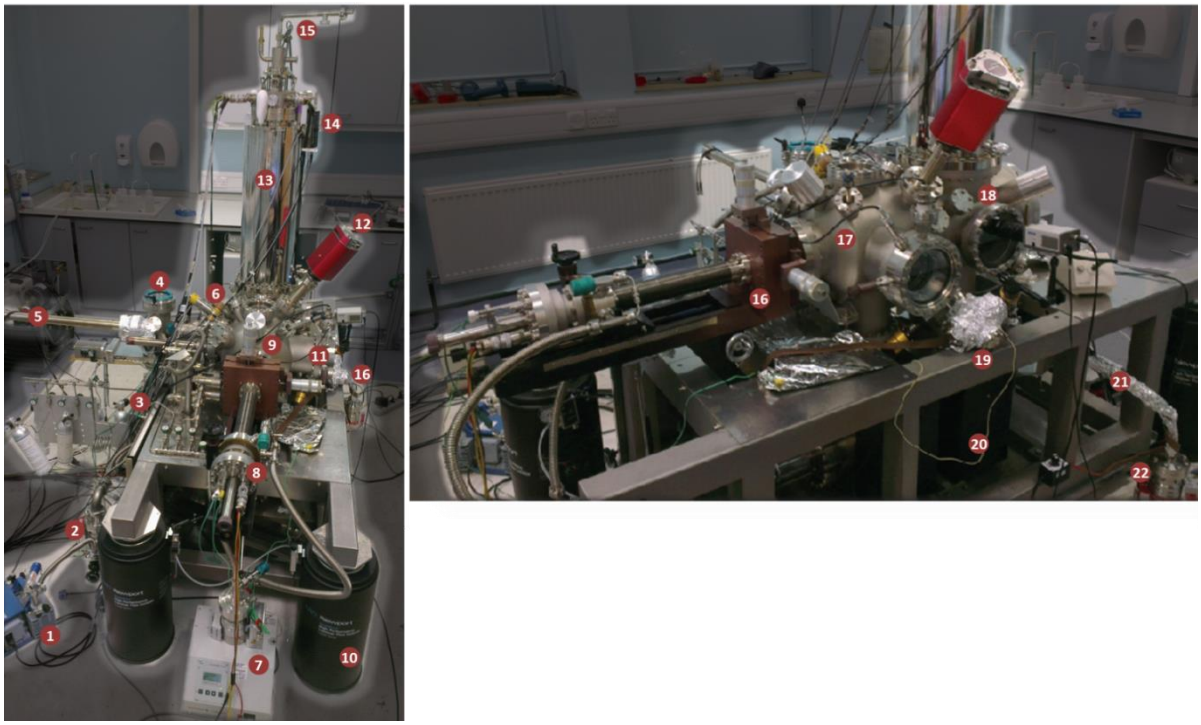

Figure 3.1 Overview of the UHV CreaTec LT-STM system. (1) Two-stage membrane pump. (2) 60 L/s pre-turbomolecular pump. (3) 240 L/s main turbomolecular pump. (4) Load lock chamber. (5) Magnetic transfer rod. (6) Ion gun with piezo-controlled leak valve. (7) Turbo pack for pumping of manipulator and gas-line system. (8) Variable-temperature manipulator. (9 & 17) Preparation chamber. (10) Compressed air Newport damping legs. (11) LEED/AES. (12) Residual gas analyser. (13) LN_2/LHe bath cryostat. (14) Current pre-amplifier for the STM. (15) Transfer line for cryogens. (16) x/y movement stage for manipulator. (18) STM chamber. (19) Molecular evaporator. (20) Ion pumps/TSP. (21 & 22) Pumping line for molecular evaporator.

The turbo chamber is separated into two parts by a gate valve. Below the gate valve, there is a 240 L/s turbo-molecular pump which is backed by a 60 L/s turbo pump, which in turn, is backed by a two-stage membrane pump. Above the gate valve is a fast entry load lock with a hinged KF viewport flange, which can be isolated from the vacuum and opened to atmospheric pressure. This allows for quick transfer of samples into or out of the UHV system without the need to vent the entire system. Pumping through the turbo pumps directly below returns the

pressure to an acceptable level (1×10^{-9} mbar) within 30 minutes, and allows the newly introduced sample to be moved to the prep chamber using the magnetic transfer rod.

To achieve UHV conditions, all three sections of the vented system are opened to each other and then pumped through the turbo stage until a pressure of approximately 10^{-5} mbar is achieved. Then a metal baking tent is constructed around the system and the entire instrument is heated to 135°C for at least 72 hours. This removes water adsorbed on the interior walls, which would otherwise be pumped away very slowly at room temperature. After this stage, the system is cooled while outgassing all of the filaments. A base pressure of approximately 10^{-9} mbar remains, and is mainly due to residual hydrogen gas in the system which the turbo pumps are inefficient at removing. The hydrogen is removed using titanium sublimation pumps (TSP) located in both the prep and STM chambers. After full conditioning of the system, ion pumps maintain the pressure in both of the main chambers, and the turbo stage may be isolated from them. The full baking and conditioning process leaves the UHV system with base pressures of 3×10^{-11} mbar in all three sections (without additional cryo-pumping).

Besides providing pumping during evacuation of the system, the turbo stage is used when high pressure operations such as sputtering or deposition are performed in order to protect the ion pumps from high pressure, which can reduce their lifetime of operation. The turbo pumps are switched off during scanning to reduce vibration. A series of shut-off valves directly at the exit of these pumps preserve the vacuum well during this time (by minimising back flow into the turbo stage), and when switched back on, the pressure recovers very quickly (typically 10^{-10} mbar after 60 minutes), allowing the instrument to be used without any delays to wait for vacuum recovery.

The prep chamber is where most of the sample preparation is conducted. It houses a manipulator which allows the samples to be annealed via resistive heating, and it allows movement of the samples from the prep chamber into the STM chamber for measurement. The manipulator can be cooled with cryogens to achieve deposition temperatures as low as 20 K. It is differentially pumped by a dedicated turbo station through a rotational feedthrough, and allows movement of the sample in all three spatial dimensions as well as 360° rotation. The samples used by this system have a specific geometry and is displayed in Figure 3.2. A typical sample consists of a high purity metal single crystal (Cu(110) in the case of this project), which is attached to a heating oven by a molybdenum clip, and is connected to four pins on the back. The manipulator T-piece is attached at the rear and makes a connection from these

pins to external electrical feedthrough connections. Pins 1 and 4 allow current to pass through the oven to heat the crystal during annealing; pins 2 and 3 provide connection for the thermocouple (type K) to allow the sample/surface temperature to be monitored. When not in use, samples are stored in the prep chamber on a dedicated garage, which also accommodates spare STM tips.

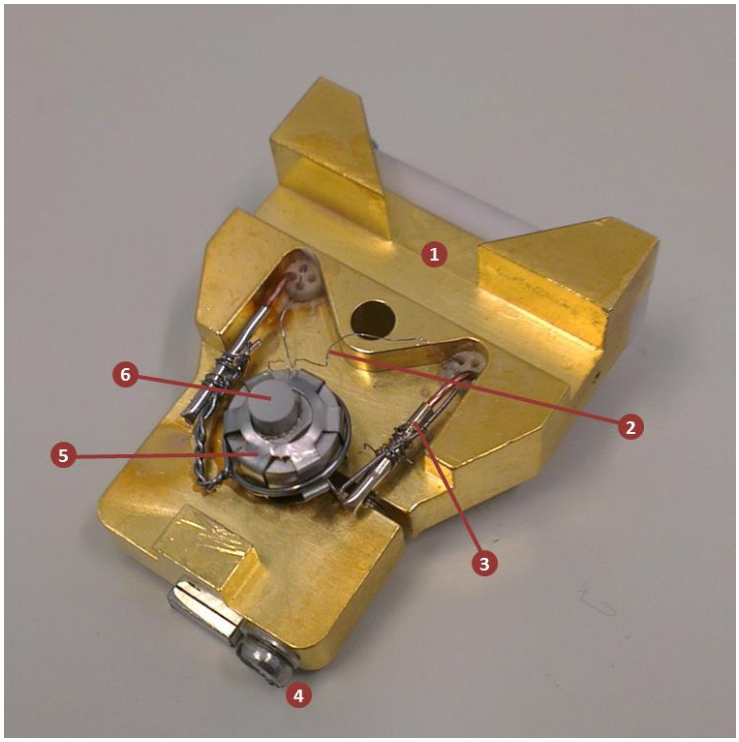

Figure 3.2 Single crystal sample holder for LT-STM system. (1) Attachment point of manipulator. (2) Thermocouple wires (alumel/chromel). (3) Connections for annealing and sample biasing. (4) Screw to secure heating oven. (5) Heating oven and Mo clip. (6) Single crystal surface.

Also housed in the prep chamber are the ion gun (for sputtering the sample), a wobble-stick (for cleavage of layered samples), a combined LEED/Auger system (for checking sample cleanliness and crystallinity), and a residual gas analyser mass spectrometer (RGA with 0—100 amu range). Access to the gas line system allows a range of gases and volatile liquids to be deposited on the sample with fine control of the pressure via a piezo controlled leak valve. Solid materials can also be deposited via sublimation from a molecular evaporator. In the event that organic molecules with a high vapour pressure are used, which may contaminate the prep chamber, deposition can be performed in the load lock.

The STM chamber houses the STM scanning unit. The STM is attached to the bottom of the cryostat which is composed of a 15 L outer section, and a 4 L inner tank. The outer part is filled

with LN_2 and serves to insulate the central section which can be filled with LN_2 or LHe to allow measurements to be conducted at 78 and 5 K, respectively. The STM block is cooled by thermal contact via a gold finger, which extends from the base of the inner cryostat, and thermal equilibrium is typically reached after 1 hour at 78 K, and after 8 hours at 5 K. To further insulate the sample, the STM is protected by a two-layered radiation shield which is opened and closed for sample delivery via a lever at the top of the cryostat. A further hole at the rear, which can opened and closed using a wobble stick in the STM chamber, makes it possible to deliver gases from the gas-line system and allows real-time monitoring of adsorption processes during STM acquisition. The radiation shield has two viewports to allow visualisation of the tip approach using a camera. Nevertheless, the optical access to the interior of the STM is severely limited and care must be taken when transferring a sample so as not to damage the delicate parts of the scanner.

3.2.2 The CreaTec LT-STM

The STM is a Besocke-beetle-type[2] and hangs below the inner cryostat suspended from fine springs. This design is known to have good thermal and vibrational isolation from the surrounding UHV chamber. The STM is shown in Figure 3.3 dismounted from the chamber. The tip is attached by a magnet to a central piezo element which is attached to a metal disk (ramp). The ramp position is controlled by a further three coarse piezo stacks. Coarse approach of the tip is achieved by moving the ramp rotationally downwards when pulse voltages are applied to the three outer external piezos. Using this method, the user moves the tip into close proximity with the surface, and then an automatic approach routine is activated. Fine approach is then achieved by repetitive coarse movement of the tip, followed by extension of the central piezo in a stepwise manner. When a tunnel current exceeding the set-point current is measured, the auto-approach is deactivated and scanning can commence. The x-y motion of the tip across the surface is controlled by the outer piezos, while the central piezo controls the tip height. Alternatively, all three directions of motion can be controlled using the central piezo. The former method provides images with less distortion due to the absence of electronic cross-talk and mechanical instabilities which comes from coupling of x,y,z deformations of a single piezo element. During STM measurements, the sample is biased via a connection to the pins in the STM unit (1 in Figure 3.3). This means that any data which has been collected with negative bias corresponds to tunnelling from the filled states of the surface to the empty states of the tip. Conversely, positive bias indicates tunnelling from the tip into the sample.

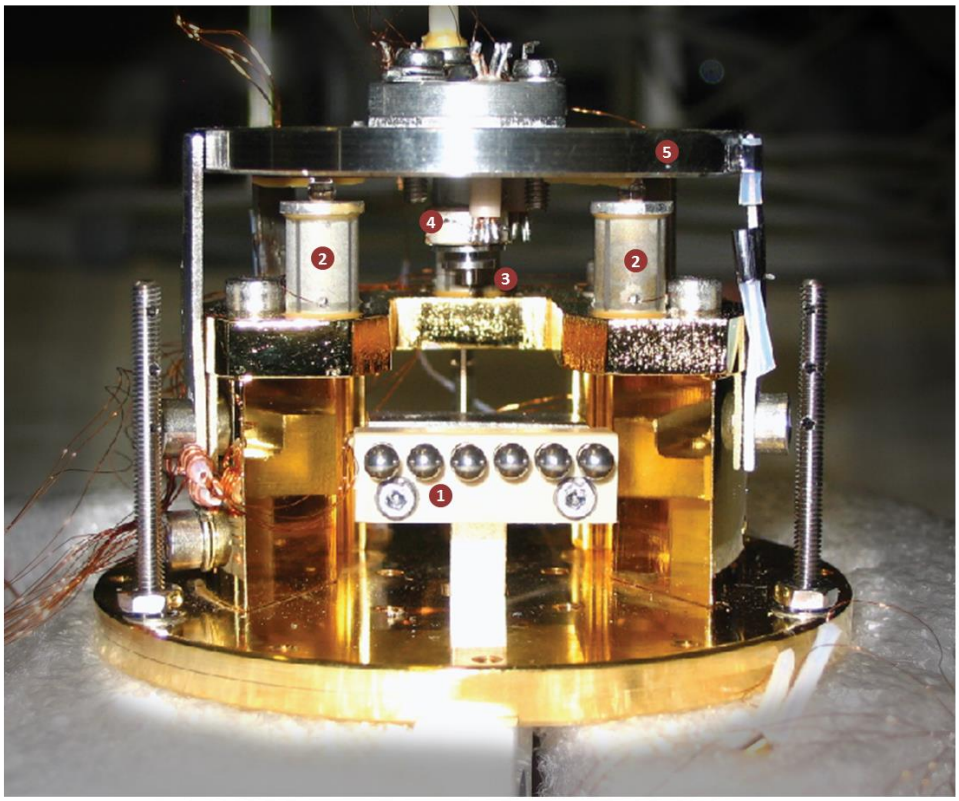

Figure 3.3 The dismounted scanning unit. (1) Sample stage with contact pins. (2) Coarse piezo stacks (×3). (3) STM tip. (4) Central piezo element. (5) Ramp for coarse tip positioning and approach.

Controlled movement of the tip relative to the surface is achieved by sub-Ångström displacements of the piezo elements. To allow high resolution data to be collected, it is crucial that the STM is mechanically isolated in order to prevent introduction of vibrational noise into images. This is achieved in a number of ways. First, the STM block can be released via a pull-down mechanism, and the aforementioned springs mechanically decouple the STM from the chamber while scanning occurs. Second, the system is equipped with four Newport air-legs, which lift the system off the ground when pressurised with air and damp mechanical vibrations down to approximately 5 Hz. Finally, the whole system is placed on a 14 tonne concrete block which rests on the earth below the building, and serves to decouple the building and the system to exclude external disturbances from affecting measurements. Further stability of the STM junction is achieved by cooling to 5 K using LHe. This dramatically reduces thermal drift to 1 Å/hour laterally and 1 pm/hour in the z direction.

All of the described features mean that the STM is very stable, and this is vital when spectroscopic measurements are undertaken. During these measurements, the feedback control, which holds the tip at a set height above the surface, is deactivated. Appreciable vertical drift would cause exponential changes in the measured current and therefore preclude

the measurement of pA differences in the tunnel current, which are required for STS experiments. To further improve the signal to noise ratio of STS spectra, the derivative signal can be obtained directly using an internal lock-in amplifier. Rather than collecting zero order I vs V data, the lock-in applies a small oscillatory modulation to the sample bias and measures the current via a separate channel at the modulation frequency. Frequencies of up to 6 kHz can be selected and are usually chosen carefully so as to not couple to the resonance frequency of the system.

The tunnel current is of the order of 1 nA and therefore cannot be measured directly by the electronic unit due to resistive losses in the wiring. Therefore, the current is converted to a voltage signal by a variable gain, low noise pre-amplifier (for scanning, a gain of 10^9 is generally used). This signal is fed to the digital signal processing (DSP) unit, with which the computer software interfaces to display the data as it is collected.

3.2.3 Molecular Sources

To introduce molecules into the UHV system, two main methods exist: sublimation from a molecular doser; or delivery of gases via the gas-line system. Cleaning of the crystal by sputter and anneal cycles takes place first, then the vacuum in the chamber is recovered, and then exposure of chemical species can take place. Purity of such materials can be verified using the RGA provided that their mass does not exceed 100 atomic mass units.

Molecular Evaporator

For polycrystalline, powdered organic substances (as is the case for the quinone derivatives, azophenine and azotolyline, used in this study), a home-built molecular evaporation system is used. Shown in Figure 3.4, it consists of a glass tube containing the powder, and is secured to a copper support rod with a tantalum clip. A ceramic stopper is placed in one end, and thermocouple connections are introduced through the ceramic to read the temperature at the centre of the powder. The organic molecules are heated by a tantalum wire wrapped around the tube. The filament is connected to a further two Cu contacts which are fed through the CF36 flange to a power supply.

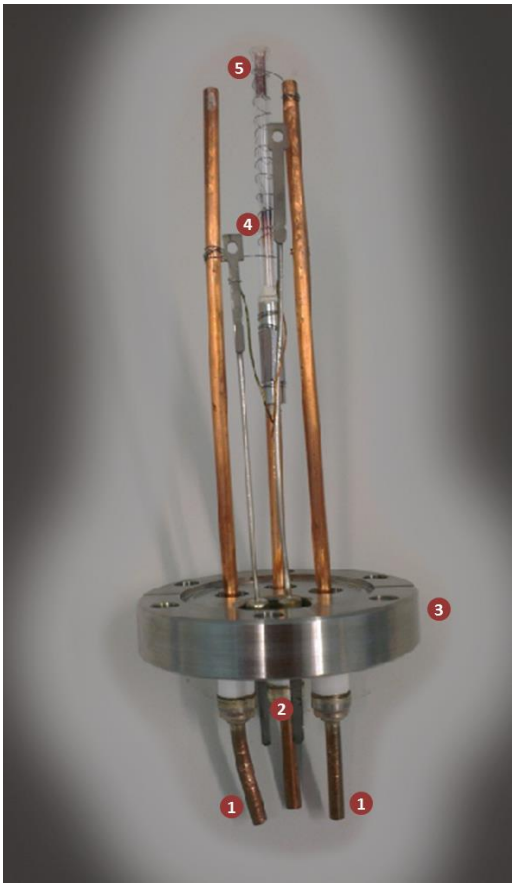

Figure 3.4 Molecular evaporator. (1) Electrical contacts for heating filament. (2) Thermocouple contacts. (3) CF36 flange for attachment to UHV system. (4) Polycrystalline molecules to be sublimed. (5) Glass tube with tantalum filament wrapped around.

The molecular doser is fitted to a T-piece and attached behind an external gate valve on the prep chamber. A dedicated pumping system, consisting of a 60 L/s drag pump backed by a 60 L/s turbo pack, is also attached at the T-junction. While pumping, this line is baked using a heating tape at a temperature just below the sublimation temperature of the molecules. A pressure of about 5×10^{-9} mbar is achievable using this system. Furthermore, a low current is passed through the filament for 2-3 hours prior to deposition to thoroughly outgas the evaporator and remove excess moisture from the powder. This set-up allows the molecular evaporator to be replaced quickly without the need to vent the entire system.

For a typical deposition, the current passing through the filament is slowly ramped until the evaporation temperature is reached. The gate valve separating the prep and doser is quickly opened while the external pumps are isolated to stop any back flow of atmospheric gases into the chamber. For a typical molecular deposition, a pressure increase to only ~ 3×10^{-10} mbar in the prep chamber is observed, indicating a pure and clean sample of molecules has been

achieved after baking. After the deposition time has elapsed, the gate valve is closed and the sample is swiftly transferred to the cooled STM to avoid contamination.

The azophenine molecules, which form the main part of this work, were synthesised at the University of Bristol by Christopher J. Adams. The route to their synthesis is as follows: To a solution of N,N'-diphenyl-p-quinone diimine (0.5 g, 1.93 mmol) in chloroform (25 ml) was added aniline (0.4 ml, 4.21 mmol) and a catalytic amount (a few crystals) of p-toluenesulphonic acid. The solution was stirred overnight, and then 25 ml of methanol was added to complete the precipitation of the dark red product. This was isolated by filtration, washed with methanol and dried to give 0.276 g (0.63 mmol) of product. Microanalysis for $C_{30}H_{24}N_4$ (azophenine): Calculated: C, 81.8; H, 5.5; N, 12.7 %; Found C 80.8; H 5.4; N, 12.3 %. The N,N'-diphenyl-p-quinone diimine is made according to reference[3]. The azotolyline sample was purchased from Sigma-Aldrich.

Gas-Line System

The gas-line system is an in-house addition to the manufacturer's specification, and can be used to deliver a range of gases to both the prep and STM chambers. Gases contained in pressurised bottles can be stored in one of three reservoirs prior to deposition. Control from leak-valves behind these reservoirs allows the chamber to be back-filled with the desired partial pressure of gas. In the case of pressures exceeding 10^{-9} mbar, or when noble gases are used, the ion pumps are isolated. Volatile liquids can also be administered using the gas line by attachment on a blind valve, and using a heat source to evaporate it into the prep chamber. Another use for the gas-line is to supply argon to the ion gun during sputtering procedures. The line is held under vacuum when not in use by the turbo pack used to differentially pump rotary feedthrough of the manipulator.

3.2.4 Tip Preparation

Acquisition of quality STM data depends on the shape of the probe and, ideally, it should be terminated with a single atom. Tips which are blunt provide images with poorly resolved features, while tips terminated by multiple atoms give images which show features with ghosted duplication. Care must therefore be taken to prepare STM tips so that the likelihood of them providing clear images after transfer to the vacuum is maximised.

STM probes can in theory be fabricated from any conductive material; the two most commonly used are W and Pt/Ir alloy. Tips for the CreaTec system are held in a tip holder of specific design, as shown in Figure 3.5a. The wire is held in place by making a small bend at the top and pulling it through the central hole until it becomes secure. Preparation of a Pt/Ir tip involves pulling a piece of wire (Pt 80%, Ir 20%, 0.25 mm diameter) at both ends while making a quick cut with a pair of sharp wire cutters. The sharpness of both cut ends can then be inspected macroscopically using an optical microscope; however, there is no guarantee that an atomically sharp termination has been created. Using W to produce a tip can be done in a more controllable and reliable manner by electrochemical etching. This is done using an improvised etching device (shown in Figure 3.5b). A piece of wire (0.25 mm diameter) is secured in the tip holder, and then attached to the button magnet indicated by the number 3. Next, the micrometre screw is adjusted until the length from the base of the tip holder to the part of the wire dissecting the plane of the tantalum loop is 4.5 mm. A solution of concentrated NaOH is then used to produce a film in the loop where the etching of the wire will occur. An electrochemical potential is then applied by positively biasing the tip and negatively biasing the loop. The following reaction then takes place as the W wire is etched by the alkaline solution:

Tip: $\mathrm{W}(s) + 8\mathrm{OH}^{-}(aq) \rightarrow \mathrm{WO}_4^{2-}(aq) + 4\mathrm{H_2O}(l) + 6\mathrm{e}^{-}$

Loop: $6\mathrm{H_2O}(l) + 6\mathrm{e}^{-} \rightarrow 3\mathrm{H_2}(g) + 6\mathrm{OH}^{-}(aq)$

Redox: $\mathrm{W}(s) + 2\mathrm{OH}^{-}(aq) + 2\mathrm{H_2O}\ (l) \rightarrow \mathrm{WO}_4^{2-}(aq) + 3\mathrm{H_2}(g)$

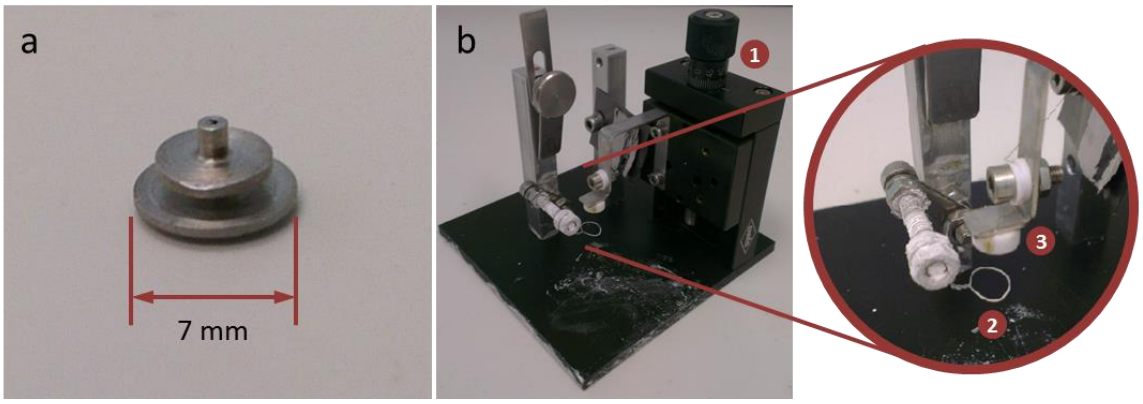

Figure 3.5 Tip preparation apparatus. (a) STM tip holder. (b) Home-build electrochemical etching set-up. (1) Micrometre screw for adjustment of tip length. (2) Tantalum loop on which film of NaOH is made for etching. (3) Magnetic button for holding tip holder.

The rate of the reaction can be altered by increasing the potential difference between the electrodes. A long etching time is preferable as it produces a more tapered shape with higher chance of an atomically sharp tip. When the etching process is completed, the excess W drops off, and the tip has the desired length. A post-etching rinse with deionised water to remove excess ions, and storage under ethanol ensures that the tip is not oxidised appreciably by the ambient air before it is introduced into the UHV system. W tips have the advantage of controlled fabrication but can have a complicated signature when used for spectroscopic measurements due to the presence of oxide. Pt/Ir on the other hand has a smooth density of states at the Fermi level and is resistant to oxidation in ambient environments, and is therefore preferred when conducting STS measurements.

In vacou, a number of methods exist to improve the tip shape; however, there is no tried and tested way of producing a single atom termination. STM users have to rely, in part, on the black art of tip preparation. With that being said, the tip can be sputtered with Ar^+ and annealed by electron bombardment to clean any excess oxide which may be present. After transfer to the STM, the tip can also be sharpened by locally heating the end of the tip. This is done using field emission by applying a high voltage (~100 V) between the tip and an unused part of the metal crystal. With the methods of tip preparation described, these two procedures are rarely used and it is sufficient to improve the tip upon reaching tunnelling. Repeated voltage pulses or controlled tip crashes usually allow the user to form the tip to allow collection of sharp images.

3.3 The Cu(110) Surface

Copper is a face centred cubic (FCC) metal with atoms located at the vertices and at the centre of each face of the unit cell (Figure 3.6a). A cut through the (110) plane gives the unreconstructed, two-fold symmetric Cu(110) surface. In comparison with the Cu(111) and Cu(100) surfaces, which have atom coordination numbers of 9 and 8, respectively, the Cu(110) surface has coordination of 7 and therefore has a higher surface energy, is more open, and is therefore more reactive. The interatomic spacing along the high symmetry [-110] and [001] directions are 2.56 Å and 3.62 Å, respectively.

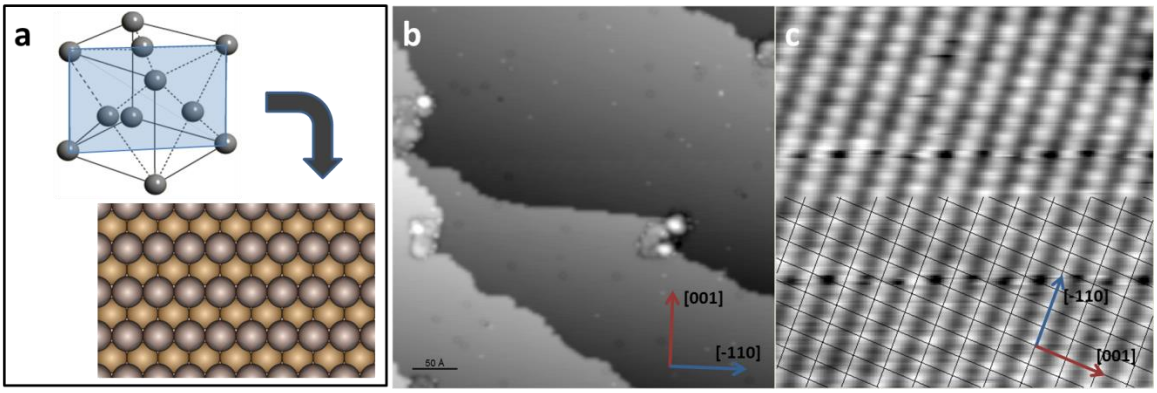

Figure 3.6 (a) Face-centred cubic unit cell with a cut along the [110] face with the resulting surface schematically drawn. (b) Constant current STM image of the Cu(110) surface after preparation (I = 0.89 nA, V = -0.85 V, T = 5 K). (c) Atomically resolved image of the Cu(110) surface (I = 1.0 nA, V = 0.02 V, T = 5 K)

The crystal is cleaned by repeated cycles of sputtering with Ar^+ (1.5 keV, 1×10^{-6} mbar, 10 min), followed by annealing to 773 K for 15 min. In Figure 3.6b the clean surface is imaged using STM, and it can be seen that the cleaning process results in large atomically flat terraces with few defects or pollution. The step-edges generally run in the [-110] direction due to the stronger interaction between atoms due to their closer packing. Small amount of pollution species such as CO or oxygen are seen on the terraces and at the step edges, respectively. The source of CO is most likely from desorption from the internal filaments or the walls of the chamber when the pull-down mechanism is used to release the sample for scanning. The release of the sample, using this mechanism, is done carefully to avoid contamination, but it is not completely avoidable.

3.4 DFT Calculations

The DFT calculations were performed both locally, using the Wardlaw computational cluster in St Andrews, and on a national supercomputer, HECToR, located at the University of Edinburgh. Wardlaw consists of 290 nodes, each containing 12 processing cores and either 24 or 48 GB memory. They are connected over a quad date rate (QDR) Infiniband network, which delivers four bits of data per clock cycle, allowing more efficient processing. There are 150 TB of disk space. The front-end system operates under Linux CentOS, and is equipped with software for molecular quantum chemistry, molecular dynamics, and periodic methods including plane wave DFT. HECToR is composed of 90,112 cores and is capable of 800 teraflops. It has storage

space in excess of 1 PB. The more computationally intensive calculations, such as nudged elastic band (NEB) calculations, were performed using HECToR.

3.5 References

1. S. Zöphel, Freie Universität Berlin, 1996.
2. K. Besocke, *Surf. Sci.*, 1987, **181**, 145–153.
3. J. Honzl and M. Metalová, *Tetrahedron*, 1969, **25**, 3641–3652.

4 Molecular Switches

4.1 Summary

In this chapter, the switching properties of a family of quinone derivatives adsorbed on Cu(110) are investigated. STM measurements are used to image the molecules and identify the topographical change induced when pulsed with electrons from the STM tip. By quantifying their rate of switching under different tunnelling conditions, the activation energy of the switch is determined and the excitation stimulus is identified as inelastic electron tunnelling. Through computational modelling, the mechanism underlying the switching process is confirmed to be hydrogen tautomerisation. The reaction pathway is also determined, and is found to consist of a sequential transferral of protons occupying adjacent amino groups located in the central active moiety of the molecules. The work of this Chapter has been published in Nano Letters[1] and the abstract figure is displayed in Figure 4.1.

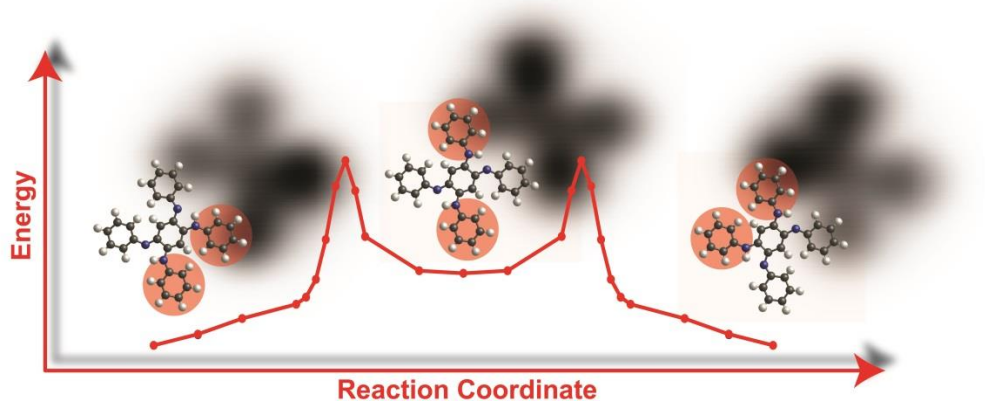

Figure 4.1 Graphical Table of Contents figure for the publication[1] associated with this chapter. The experimental STM data (monochrome) are summarised along with the main theoretical results (colour). Represented is a *meta*-AP → *meta*-AP H-tautomerisation involving a specific *para*-AP intermediate.

4.2 Introduction

Semiconductor devices dominate the microelectronics industry, and the miniaturisation of such devices has seen great progress such that a standard smartphone now contains on the order of a billion transistors. However, as their size decreases ever further, problems such as power consumption, heat dissipation, and quantum effects become important. There is therefore a need to design conceptually new methods to handle information at the nanoscale.

There are two main strands of nanotechnology research which are trying to address this problem: the use of the two-dimensional carbon allotrope graphene which is strong, light, and is an excellent conductor; or the use of single molecule architectures as electronic components. The latter aims to replicate the function of an electronic component, such as a switch, within a single molecule. As molecules are the smallest stable structures, it may be seen as an endpoint in the miniaturisation. Furthermore, the bottom-up approach of using molecules as building blocks to construct complex circuits has a cost advantage over the current top-down approach.

A molecular switch is a molecule which is stable in two distinguishable states, and these states can be addressed using some external stimulus. Molecular switches, in particular, have therefore attracted much interest because of their ability to encode the basic “1” and “0” used in binary systems. In Chapter 1, a full description of molecular switches, their mechanisms, and their excitation processes was given. This chapter focusses on a family of molecular switches based on hydrogen tautomerisation in a quinoid moiety, which uses inelastic tunnelling electrons to activate the process.

The novelty of this system is twofold. The switch is the first of its kind which employs H-tautomerism which is not restricted to the macrocycle of a porphyrin type molecule. This means that the H transfer occurs at the periphery of the active switching moiety, and shows that tautomeric protons need not be protected in order to confer a molecule with two stable states. Secondly, the molecule may be functionalised without compromising the switching property; hence, the structure can be tailored to fit specific criteria. In addition, there is no change in shape or position of the molecule in conversion between the two states of the molecule. This is an important property when considering how such a molecule could be integrated into a circuit.

4.3 The Molecular System

The molecules investigated are all based on a nitrogen-substituted quinone derivative known as 3,6-diimino-1,4-cyclohexadiene-1,4-diamine (DCD). The molecule is composed of a central cyclohexadiene ring with amino and imino functional groups located at the 1,4 and 3,6 positions, respectively. This represents the central functional unit of the family of compounds that are studied here. Functionalisation of this structure through substitution of amino hydrogen atoms by phenyl and tolyl groups forms N,N'-diphenyl-3,6-bis(phenylimino)-1,4-cyclohexadiene-1,4-diamine (azophenine, AP) and N,N'-ditolyl-3,6-bis(tolylimino)-1,4-cyclohexadiene-1,4-diamine (azotolyline, AT), respectively. All three structures are displayed in Figure 4.2.

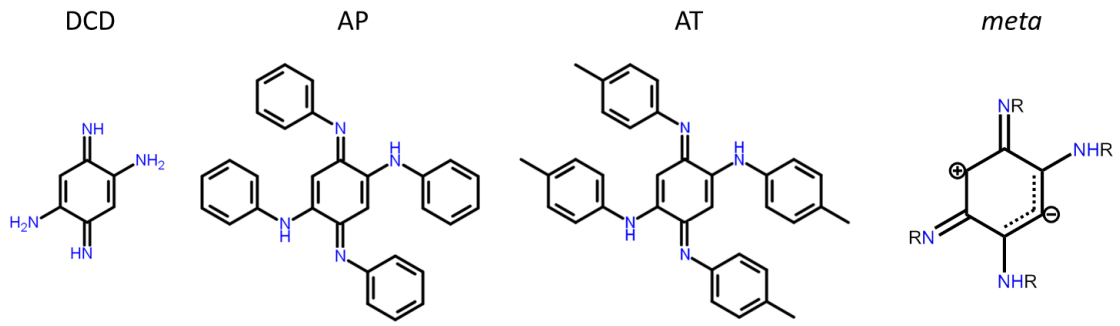

Figure 4.2 Chemical structures of DCD, AP, and AT in their native *para*- states. The *meta* structure shown has no Lewis structure in the gas phase.

The molecules exist in their native state as red polycrystalline solids in the isomeric forms indicated above. Different isomeric forms have been studied in this investigation and, for ease and clarity, the structures will be referred to as *para*, *ortho* and *meta*. *Para* indicates the case in Figure 4.2, where identical substituents of the central, 6-membered carbon ring occupy positions directly opposite (*para* positions 1,4) to each other. Correspondingly, *ortho* and *meta* structures refer to the situation where identical functional groups occupy the 1,2 and 1,3 positions, respectively. Following the normal valence rules, the *meta* structure is not stable in the gas phase due to lack of a Lewis structure. However, as will be discussed later, this species is observed experimentally on the metal substrate and is likely stabilised trough electronic coupling to the surface.

The literature relevant to these three molecules starts with their synthesis[2–4]. Their use has primarily been focussed on their ability to act as bridging ligands by bidentate coordination via the lone pairs of the nitrogen atoms[5–7]. Coordination occurs after a conversion from the native *para*-state to the *ortho*-state, indicating that isomerisation of these compounds can be

induced and will be discussed later in this chapter. Derivatives of these compounds have also seen use as pH-dependent chromophores[8,9].

Additional examples in the literature document a double proton transfer in these molecules[10–12] involving the hydrogen atoms located on the amino groups. Through spectroscopic and *ab initio* methods, the authors were able to show that a rapid tautomerisation between the two para states occurs in liquid solution and crystalline solid phases. This observation led to their selection as potential candidates for molecular switches. However, the tautomerisation observed when adsorbed on a metallic surface is quite different, as we will find out in the rest of this chapter.

The molecules were deposited onto a Cu(110) surface to investigate their possible switching properties. This surface was used because both it and the molecules have 2-fold symmetry, which means that the number of different adsorption configurations is limited, and hence, the complexity of analysis is reduced. Furthermore, copper is ubiquitous in the fabrication of electronic components and the interaction of a molecule with such a metal is of obvious interest. Surprisingly, no surface studies have been conducted on these molecules until now, despite azophenine first being synthesised in 1875.

The clean Cu(110) surface was prepared by repeated sputter/anneal cycles in a vacuum chamber with base pressure < 1×10^{-10} mbar (see chapter 3 for details). After cleaning, the crystal was cooled using liquid nitrogen to 78 K. The molecules were then deposited by sublimation directly into the prep chamber from a doser. This doser consisted of a glass tube heated by a filament held at 396 K and 406 K for evaporation of AP and AT, respectively. The exposure time was kept short (10 s) to ensure that a surface decorated with isolated molecules was achieved. After preparation, the sample was cooled further to 5 K before measurement with the STM. All images, unless stated otherwise, were collected using the constant current imaging mode.

4.4 Molecular Imaging

STM images of the surfaces prepared using AP and AT are displayed in Figure 4.3. Unfortunately, due to residual water being present in the DCD sample, the molecule was not successfully imaged. For this reason, experimental data on AP and AT is presented; and DCD is

included in the theoretical treatment as this represents the smallest possible molecular switch based on our quinone derivative.

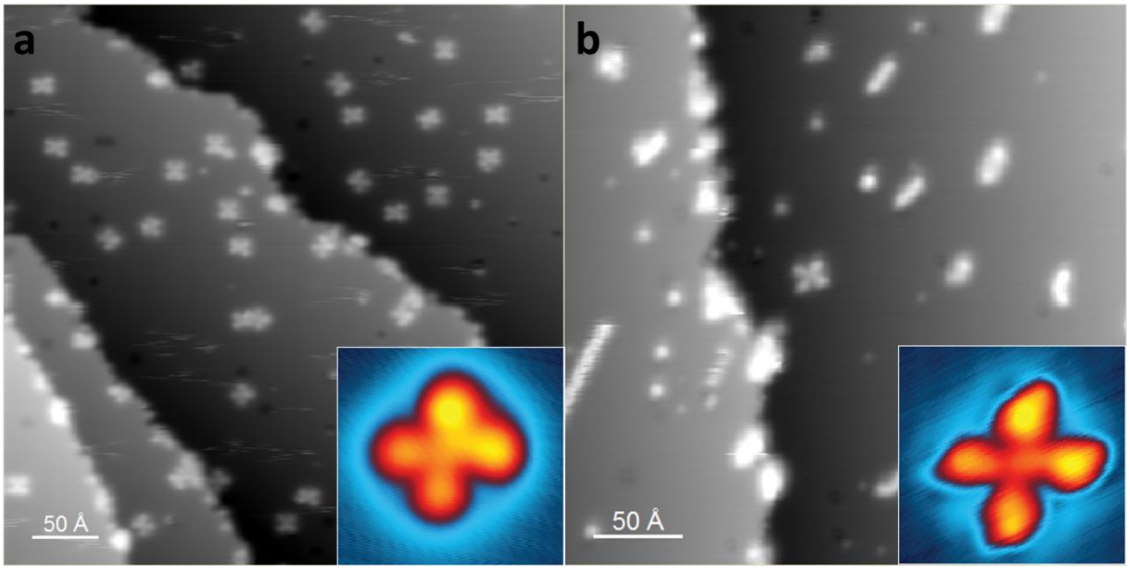

Figure 4.3 STM topographic images of (a) AP (I = 0.51 nA; V = 0.24 V) and (b) AT (I = 0.03 nA; V = -0.06 V) deposited on a Cu(110) surface, measured at 5 K. Insets show zoomed in images of each molecule.

We see that, after a short exposure, the Cu(110) surface is decorated with isolated AP molecules in a range of different conformations (Figure 4.3a). Small, unidentified adsorbates are also present in low concentrations and appear as small dark depressions or brighter protrusions. These may be attributed to small molecules such as carbon monoxide, water or oxygen which are present in small quantities in the vacuum chamber due to filament outgassing or mechanical movement of parts inside the chamber (e.g. adsorbing during sample transfer to STM). These pollutant species were kept to a minimum by ensuring that the molecules were thoroughly outgassed prior to deposition and transferring the sample as promptly as possible after preparation. We see that most of the AP molecules are isolated from each other and from pollutant species. This is important if we want to address their switching properties as it has been shown[13,14] that nearby species can inhibit such properties.

For AT, the number of intact molecules observed on the surface is considerably lower than with AP for similar deposition conditions. Comparison of the large scale images in Figure 4.3 shows that the degree of fragmentation observed in AT is much higher when compared to AP. It is unclear why this is the case and could be due to a number of factors such as bond destabilisation due to differing functional groups or sample purity. The latter is most likely because the electron donating character of extra methyl groups into the aromatic ring systems should act to stabilise the C-N-C bond which connect the side groups to the central ring. The

same adsorption configurations are observed for AT compared to AP but with less frequency due to difficulties in sample preparation. The rest of the chapter will therefore concentrate on AP but will refer to AT when comparison is necessary.

Focussing on the molecules, we see that, shown as insets in Figure 4.3a for AP and 4.3b for AT, both exhibit topographies which are clearly recognisable with respect to their chemical structures. The four lobes surrounding the central feature correspond to the phenyl or tolyl groups. When comparing AP to AT we see that, in the latter, the lobes are slightly more pointed, indicating the presence of the additional methyl groups. Since these methyl groups have the same contrast and point radially outwards, we can deduce that both AP and AT adopt flat-lying geometries when adsorbed on the surface.

We also note at this point that, in both cases, two of the lobes have brighter contrast, and are adjacent to each other while the opposite two lobes have lower STM height. This is an initial indication that a conformational change has occurred upon adsorption. From the native *para* state of the molecule, we would have expected to see diagonally opposite lobes to share similar electronic signatures, and therefore we can tentatively say that either *ortho* or *meta* forms are present on the surface. The chemical insensitivity of STM means that we cannot say which one is present; however, from our DFT calculations (see section 4.7.2), we can deduce that the *meta* species is energetically preferred.

For purposes of investigating the lowest energy structure, we now look at the different adsorption geometries of AP. The close-up images shown in Figure 4.4 show the lowest energy and most populous species but, from inspection of many STM images, we see that there exist a number of other species which are recognisable as AP but which adopt buckled or fragmented configurations. Displayed in Figure 4.4 are a number of different structures of AP.

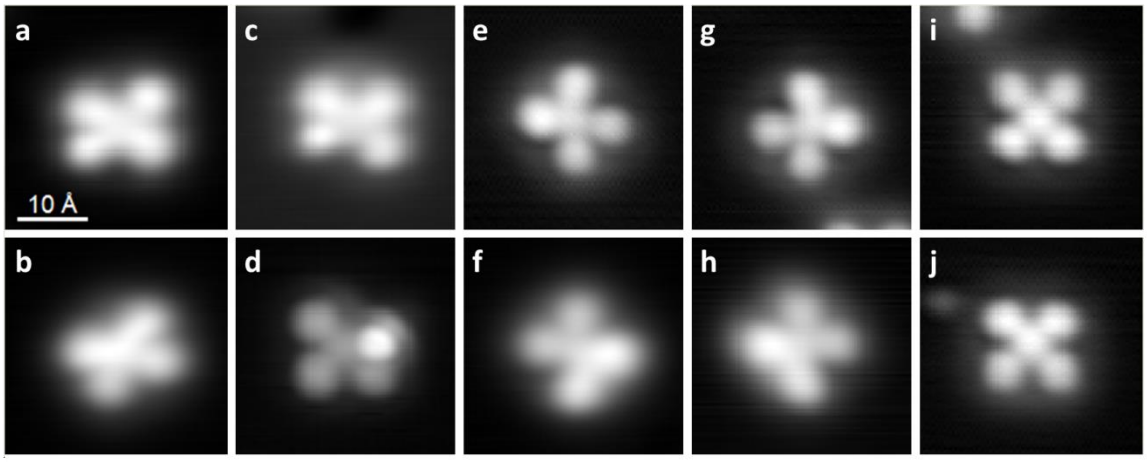

Figure 4.4 Different adsorption configurations of AP on Cu(110). (a)-(d) Buckled configurations, no switching. (e), (f) low energy *meta*-AP in both tautomeric states. (g), (h) reflectionally equivalent *meta*-AP adsorption configuration in both states. (i), (j) both tautomers of a higher energy metastable state of *meta*-AP. (I = 1.4 nA; V = -0.18 V; T = 5 K)

The presence of the deformed species shown in Figure 4.4a-d are indicative of adsorbed molecules which have phenyl or tolyl groups which are bent out of the plane of the surface or are positioned so as to make the molecule, as a whole, non-square. These are identified as high energy structures and do not display bistability. Their presence is due to molecules landing on the cooled substrate and not possessing enough thermal energy to explore the potential energy surface to reach the most stable configuration. Correspondingly, at lower surface temperatures, the population of these species is higher.

Neglecting the buckled/fragmented species, we see that we have six adsorption configurations (Figure 4.4e-j). These configurations form the majority of the species observed and are seen with equal populations on the surface. However, there is another observation which leads us to conclude that two of these structures do not conform to the lowest energy configuration.

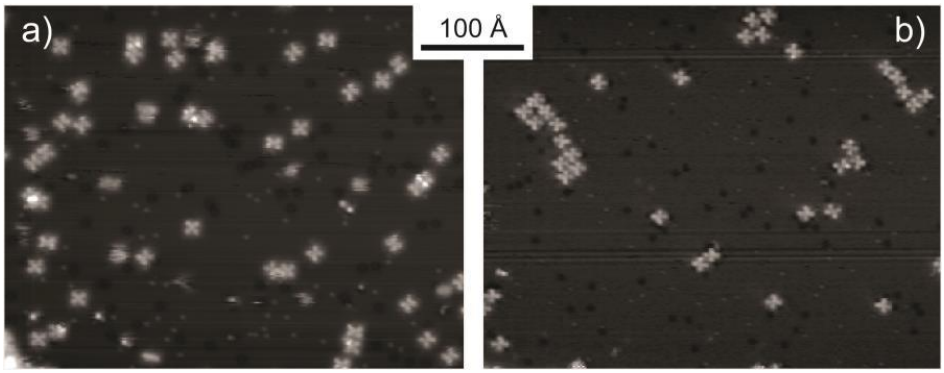

Figure 4.5 STM images of AP (a) before (I = 0.62 nA; V = -0.81 V; T = 78 K) and (b) after (I = 0.69 nA; V = 1.09 V; T = 78 K) annealing at 220 K.

A short anneal to 220 K, followed by cooling of the sample to 78 K, showed that the only species present on the surface were those displayed in Figure 4.4e-h. Before and after representative images of this simple experiment are shown in Figure 4.5. We can see that small islands of the most stable structures have formed. The buckled configurations are absent as well as the structures seen in Figure 4.4i-j. While we have attributed the buckled structures to higher energy conformational arrangements, we can also conclude that the other two structures were metastable states with energies slightly higher than the global minimum energy.

The remaining 4 molecules (Figure 4.4e-h) are the most stable structures and it can be seen that, from a topographic point of view, they are identical. Each has two adjacent lobes, which share the same bright STM contrast, opposite two dim lobes.

4.5 Switching in AP and AT

Considering the four lowest energy states on the surface, which are only distinguished by the positions of the bright lobes, the possibility of switching between these states was investigated. To do this, an open-feedback loop bias sweep from -0.5 to +0.5 V was performed on both AP and AT. The position chosen for the tip was a symmetric position between the two bright lobes as indicated by black dots in Figure 4.6c and 4.6d. The tunnel current is measured while the voltage is varied, and the result is shown for both AP and AT in Figure 4.6a. All experiments presented in this chapter use the same manipulation point to allow comparison of data between different molecules. The location dependence of the electron injection was also investigated, and is presented in Chapter 6.

We see that in both cases, the *I*/*V* curve is smooth in the interval $-0.35 \leq V \leq +0.35$, which indicates that there is no switching. Sharp, rapid changes in the current occur outside of this interval. A further manipulation, using a constant voltage outside of the ±0.35 V range reveals that the current switches between two distinct values (Figure 4.6b). This is indicative of a change in the conductivity of the tunnel junction and, since the tip height is held constant, a change of electronic structure in the molecule below the tip must be responsible. This property therefore satisfies the requirement for a switch because the binary behaviour corresponds to the molecules alternatively accessing two different conductance states.

The topographic change corresponding to this current switching is best represented as a series of sequentially acquired STM images. The example shown in Figure 4.6c shows two neighbouring AP molecules. Both molecules initially occupy the same state (in this example, both molecules have their two bright lobes in the top-right direction). The tip is then brought to the indicated position, the feedback electronics deactivated, and the bias raised to a value above the switching threshold. After a sharp change in the tunnel current is observed, the manipulation is stopped, and the same area is imaged to reveal that the targeted molecule has adopted the configuration in which the bright lobes are now opposite to the initial state (i.e. in the bottom-left direction). The same procedure is repeated on the neighbouring molecule; and then both are brought back to their original states by means of controlled voltage manipulations.

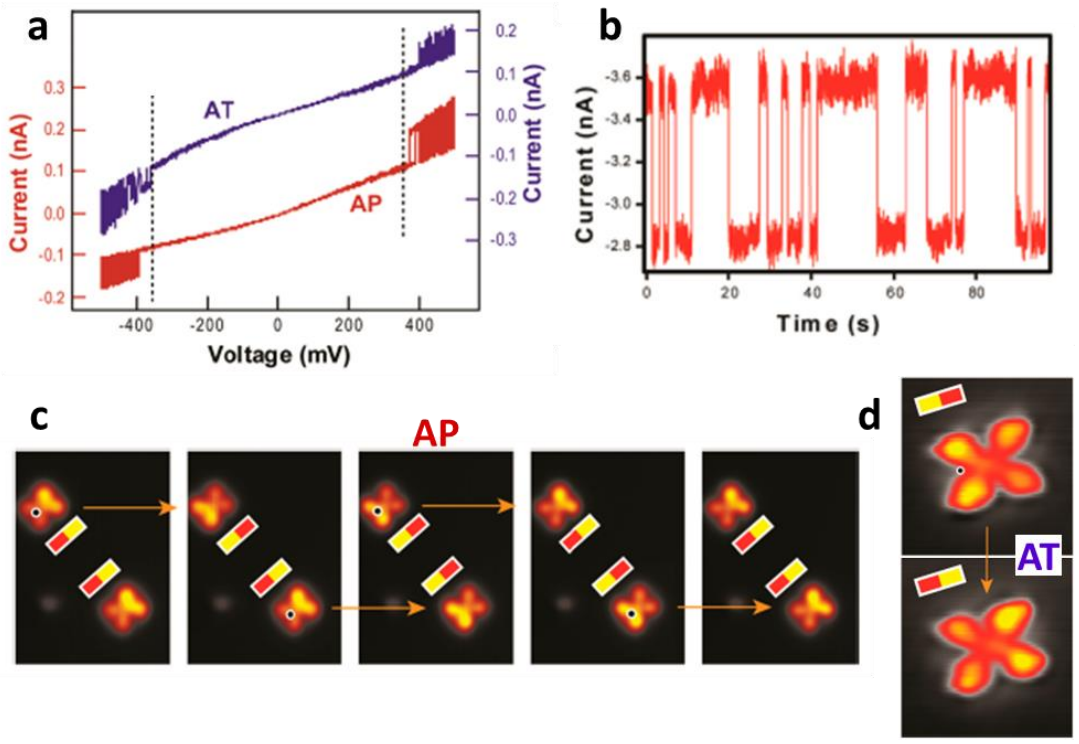

Figure 4.6 Demonstration of switching in AP and AT. (a) *I* as a function of *V* for AP (red) and AT (blue) indicating switching outside of -0.35 ≤ V ≤ +0.35 range. (b) *I* as function of time (constant *V*) showing bistable behaviour. (c) Sequentially acquired STM images of neighbouring AP molecules (I = 1.00 nA; V = -0.19 V; T = 5 K). The marked point shows the location of the voltage pulse; the next image in the sequence displays the outcome of the manipulation. (d) The same demonstration for AT (I = 0.03 nA; V = -0.06 V; T = 5 K)

The same switching behaviour is present in the further functionalised AT molecule, as shown in Figure 4.6d. We see that, after a similar voltage pulse outside the ±0.35 V range, the same qualitative result of a shift in the apparent height of the lobes from one side of the molecule to the other is present. Furthermore, we note that the shape of the lobes in AT does not change

after the switch which means that the tolyl groups do not rotate out of the plane of the surface to achieve the observed contrast change. The contrast change in both molecules must therefore be due to a more subtle change in the structure of the molecule, which is accompanied by reordering of the electron density. As we have seen from both the *I*/*V* measurements and the topographic changes observed, AP and AT are controllably switchable and the switch is activated at approximately the same voltage for both. This leads to the conclusion that chemical functionalisation of the structure does not affect appreciably the switching property.

An important observation is that the switching only involves the transfer of brightness from two lobes to the opposite two lobes. That is, switching between the states shown in Figure 4.4e and 4.4f is seen and likewise, switching is observed between states shown in Figure 4.4g and 4.4h. We never observe a switch event occurring which involves, for example, 4.4e to 4.4g. This means that we can rationalise the four lowest energy configurations identified earlier as two energetically equivalent species, each of which possesses two accessible states. The observed switching in each of these configurations is hence equivalent to a 180° rotation. Most importantly, however, physical rotation of the molecule is ruled out due to the identical switching behaviour being observed within molecular islands of AP (see chapter 5). Steric hindrance in such an environment would preclude rotational motion, and therefore points to a mechanism involving an intramolecular change in the molecule. A closer look at the adsorption registry reveals that both equivalent adsorption configurations are reflectionally symmetric when the molecule and the underlying substrate are considered.

Determination of the adsorption registry of the molecule is important as it not only allows us to say that we have two equivalent adsorption configurations, but gives a starting point for the DFT optimisations. The adsorption registry of AP was determined using a partially reconstructed Cu(110)-O(2×1) surface. This method was used due to difficulties in resolving both the substrate Cu atoms and the molecule simultaneously. The geometric structure of this reconstruction is accurately known from previous studies using low energy electron diffraction (LEED) and STM experiments[15,16], and is much more corrugated than the bare surface.

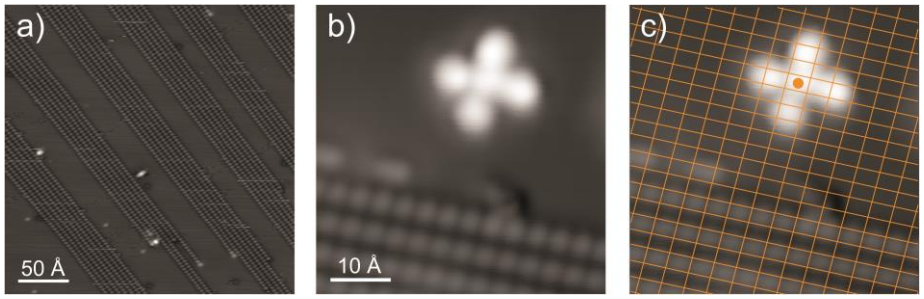

Figure 4.7 Adsorption registry determination. (a) Partially reconstructed Cu(110)-O(2×1) surface with rows of atomically resolved oxygen reconstruction (I = 1.00 nA; V = 0.69 V). (b) STM image after deposition of AP showing a molecule adsorbed close to a reconstructed region (I = 0.03 nA; V = 0.25 V). (c) The overlaid grid corresponds to the underlying Cu(110) surface (intersections are on-top sites). It can be seen that the central ring of AP lies in the 4-fold coordination site (indicated by dot).

Figure 4.7a shows a partially reconstructed surface and was achieved by exposure of Cu(110) (surface temperature: 623 K) to a low concentration of O_2 (P = 1 × 10^{-8} mbar). The resulting surface is striped with areas of O(2×1) separated by stripes of bare metal and, from the registry of the reconstruction, the underlying Cu(110) lattice is inferred as shown in Figure 4.7c. Once prepared, AP was deposited in the same manner as previously, and it was seen that the molecules' preferred adsorption region was the bare surface. The stronger interaction of the flat lying π-systems of the phenyl groups with the metallic surface rather than the oxide is the most likely reason for this. An AP molecule was imaged that had adsorbed close to the reconstruction, and the Cu(110) lattice was overlaid as shown in Figure 4.7b and 4.7c. We can clearly see that the central point of the molecule lies over the 4-fold coordination site, with diagonally opposite lobes aligned along the [-110] and [001] directions, respectively.

Both of the equivalent, lowest energy forms of AP adopt this adsorption position with respect to the underlying substrate. We can therefore henceforth consider only one of these forms and the same will be true of the other. The determination, through open-loop current measurements, that two different conductance states exist for AP and AT, allows us to regard them as bistable switches. This behaviour is as a result of some intramolecular process and the next sections will go on to confirm this as H-tautomerisation, and show that the mechanism is stimulated by inelastic electron tunnelling. A full study of the excitation process and mechanism was conducted on AP only; however, as mentioned above, the same is believed to be true for AT.

4.6 Switching Statistics

To identify the excitation process governing AP, many switching events were recorded as the tunnel current, *I*, and bias voltage, *V*, were varied. The tip was positioned as indicated in Figure 4.6 for all measurements to ensure the measured tunnel current had two distinguishable values. If a more central position is chosen the molecule still switches but the change in conductance directly below the STM tip is too small to be measured, hence the switch events cannot be seen in a *I* vs *t* measurement (see Chapter 6 for location dependence of the switching behaviour). For specific values of *I* and *V*, the time intervals corresponding to the residence time of the molecule in the high current state were measured. This takes the form of binary telegraphic noise in the tunnel current as shown inset in Figure 4.8a. Many such measurements were performed until the number of time intervals was statistically sufficient to fit a smooth curve when binned in a histogram.

This distribution takes the form of an exponential decay as shown in Figure 4.8a, and indicates that the switch is a spontaneous chemical process, and the molecule has no "memory" of the state it occupies[13]. The data were fitted using an exponential function, from which, the inverse time constant gives the switch rate, *R*, at the particular values of *I* and *V* that were selected.

$$f(t) = Ae^{-\frac{t}{\tau}}$$

By repeating this process as a function of current while keeping *V* constant, we find that for voltages exceeding ±0.35 V, the *R* vs *I* relationship is linear (see Figure 4.8b). The linear relationship indicates that the process is activated by a single inelastically scattered electron. From this, we can also rule out any dependence of the switch rate on the electric field generated by the tip, because as the tip approaches the molecule (as *I* increases) the field varies in a non-linear fashion. If the field varies non-linearly we would hence expect a non-linear variation in the switch rate, and this is not observed.

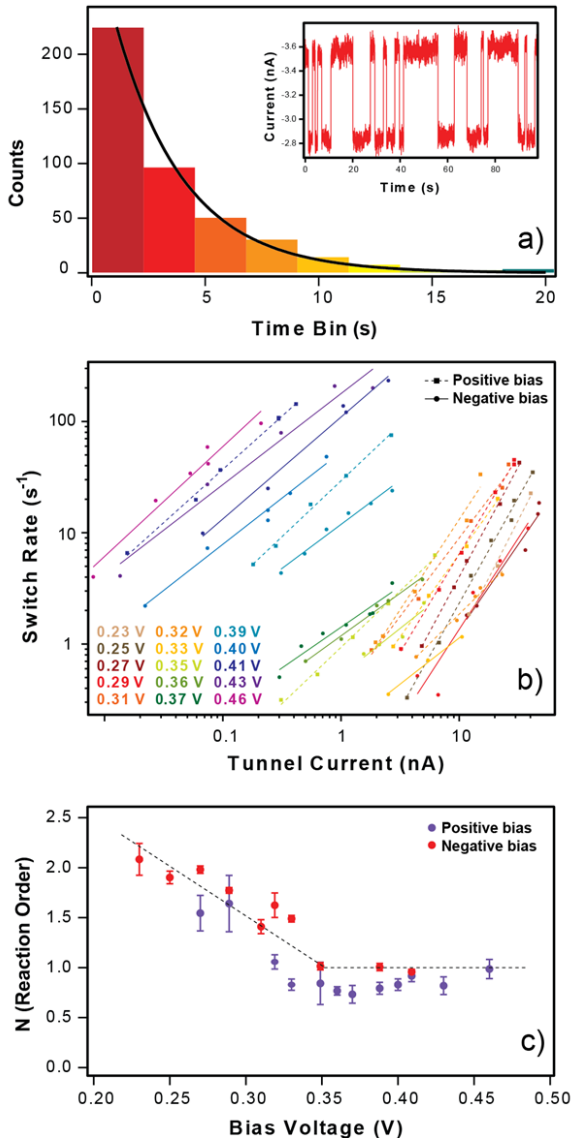

Figure 4.8 Switching statistics of AP. (a) Typical distribution of the high-current residence times from current vs. time measurements (inset). The data are fitted with an exponential fit, from which the rate of switching is extracted as the inverse time constant. (b) Switch rate as a function of tunnel current at a range of biases. The data are fitted with power laws of the form *Rate* $\propto I^N$. (c) Variation of reaction order, *N*, with *V*, showing increase at ±0.35 V.

The switch rate was determined for a range of different voltages of both positive and negative polarities as seen in Figure 4.8b. When voltages inside the threshold range were used, it was found that the dependence of *R* on *I* was no longer linear but proportional to I^N, where *N* is the number of inelastic electrons activating the process:

$$R = \frac{1}{\tau} \propto I^N$$

From this series of power laws, the reaction order, *N*, was plotted against bias voltage as shown in Figure 4.8c. We can see that *N* increases as *V* decreases below 0.35 V, indicating that

a vibrational ladder climbing process, activated by multiple electrons is in effect. The point at which more than one inelastic electron is required indicates that the activation energy for the switching process is 0.35 eV.

4.7 Mechanism

After establishing the excitation process as inelastic tunnelling electrons, we would now like to determine the mechanism governing the switching process. Rotation of the side groups as a means of switching the molecule has already been ruled out, and we know that a hydrogen transfer reaction is active in the non-adsorbed molecule. It has been said earlier in the chapter that H-tautomerisation is the mechanism, and this can be proved now by comparing our experimental observations to theoretical DFT calculations. Both the gas phase and surface bound geometries were optimised to confirm this mechanism. Dr Tanja van Mourik (University of St Andrews) performed the gas phase calculations using Gaussian, and the results are discussed. For the surface periodic calculations, models were devised by me and calculations were run by Dr Herbert Früchtl (University of St Andrews).

4.7.1 Gas Phase DFT Calculations

Initially, the structures and energies of isolated AP and DCD, both in the absence and the presence of Cu species, were investigated. These were calculations performed on discrete molecules without a metal surface, which approximates their behaviour in the gas phase. This allows confirmation of the molecules' gas phase configuration (i.e. their structure immediately before adsorption) as well as giving information on the likelihood of a change in the chemical structure in response to the presence of nearby Cu species. We also explore the energetics of transitioning between *para* and *meta* states for isolated AP and DCD so that comparison can be drawn later when the calculations involving the adsorbed molecules are discussed.

The structures were optimised using the M06-2X[17] functional and the 6-31+G(d) basis set within the Gaussian 09 software package[18].

Isolated AP and DCD

The *ortho*, *meta* and *para* isomers of both AP and DCD in isolation were optimised and their most stable conformations are displayed in Figure 4.9.

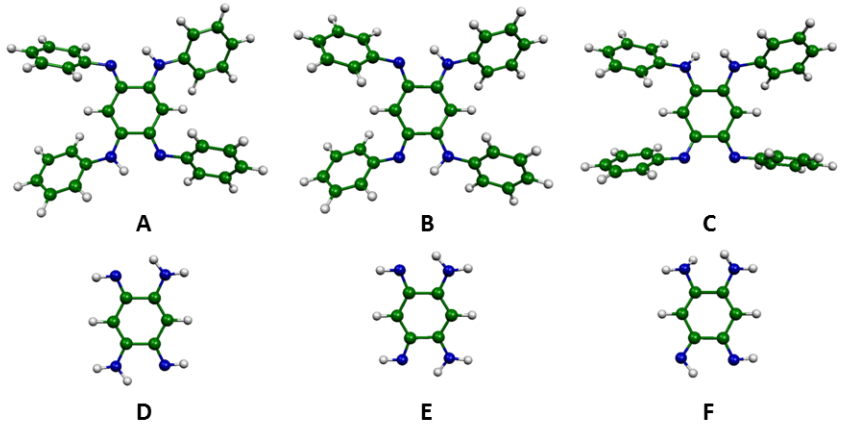

Figure 4.9 The optimised gas phase *meta*, *para* and *ortho* forms of AP (A, B, and C, respectively) and DCD (D, E, and F, respectively).

For AP we see that, in contrast to the surface-bound experimental observations, all three forms adopt highly non-planar conformations in the gas phase. Furthermore, we note that the shapes of all three are different. This indicates that steric hindrance between neighbouring phenyl groups plays a significant role in changing the energy of the molecule. In particular, the position of the two amino hydrogen atoms must be the largest contributor to this effect since this is the only structural difference when comparing *ortho*-, *meta*-, and *para*-AP. This effect is less pronounced in DCD due to the absence of bulky side groups.

Comparison of the relative energies of the AP configurations reveals that, as expected, *para*-AP is energetically favoured. This is followed by *meta*-AP (0.548 eV higher than para-AP) and then *ortho*-AP (0.798 eV relative to *para*-AP). For DCD we also see that, in agreement with literature, the *para* form is favoured in the gas phase. However, in contrast to AP, we see that *ortho*-DCD is the next most stable (0.420 eV relative to *para*-DCD), and then *meta*-DCD (0.625 eV higher than *para*-DCD). This reversal in the order of relative stability can be explained by the formation of an intramolecular N-H•••N hydrogen bond between the imino hydrogen and the neighbouring nitrogen atom. This favourable interaction acts to lower the energy of *ortho*-DCD and is not possible in AP due to the presence of larger phenyl groups in place of these H atoms.

The transition states for the tautomerisation of a single H atom in *para*-AP and *para*-DCD to form the corresponding *meta* forms were also calculated. The barriers for AP and DCD are 0.795 and 0.959 eV, respectively, and are shown graphically in Figure 4.10. For DCD this tautomerisation was calculated previously[19] as 0.57 eV. However, it is likely that the value calculated in our work, using a more up-to-date functional and basis set, is more accurate. Finally, it is worth commenting that, if the observed switch is due to a transition between *para*-AP and *meta*-AP, the computed barrier (0.96 eV) is much higher than the experimentally determined value of 0.35 eV. It is sufficient to conclude at this point that the adsorption of the molecule on the surface must lead to a lowering of this barrier.

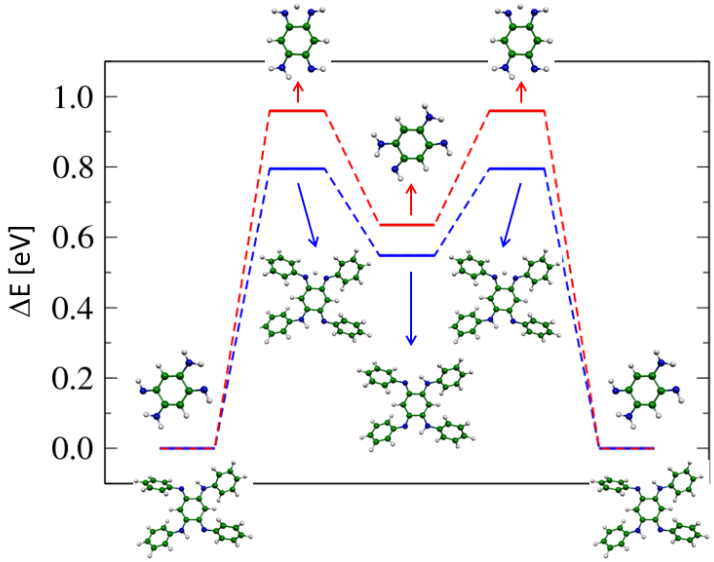

Figure 4.10 Relative energies of the stationary points along the *para* → *meta* tautomerisation pathway of gas phase AP (blue) and DCD (red).

AP and DCD in the presence of Cu and Cu^+

In order to gauge the effect of the stability of the molecules in the presence of metal species, further optimisations were performed on AP and DCD in the presence of Cu atoms and Cu^+ ions. In agreement with a previous computational study for DCD[5] and the use of these molecules as bidentate ligands[6], we find that the *ortho* configuration is preferred in both AP and DCD when a Cu^+ ion is used. *Para*-AP and *para*-DCD energies lie 0.23 and 0.33 eV higher in energy relative to their individual *ortho* equivalents, respectively. The *meta* optimised structures are much more disfavoured, with relative energies of 0.97 and 1.53 eV for AP and DCD, respectively. The same qualitative result is found when the optimisations are performed in the presence of a neutral Cu atom. The relative energies are summarised in Figure 4.11.

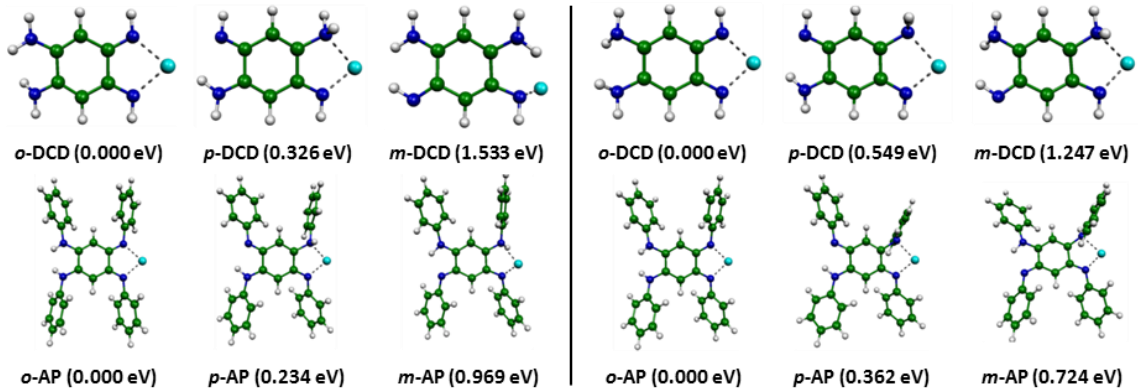

Figure 4.11 Optimised structures of DCD and AP in the presence of Cu^+ (left) and Cu (right). Energies relative to the lowest energy structure (*ortho*) are given.

It is clear from this result that the molecules can easily undergo a change of internal structure in response to a nearby Cu species. This supports the experimental observation of adjacent bright lobes, meaning that we have a configurational change away from native *para*-AP when AP comes into contact with the Cu(110) substrate. While this result and the above mentioned transition barrier give insight into the gas-phase molecular system, we must model the full bound system (molecule + surface) to provide an accurate determination of the adsorbed structure, mechanism, and activation energy.

4.7.2 Periodic DFT Calculations

With the gas phase calculation confirming that a configurational change from *para*-AP to *ortho*-AP is possible in the presence of copper, but disagreement with the experimentally observed barrier height, the AP molecule on a Cu(110) slab was optimised in order to give a more representative model of the AP/Cu(110) system. These periodic calculations were performed using the Vienna Ab-initio Simulation Package (VASP)[20–22] using the PBE functional[23] and a plane-wave basis set. For computational convenience, the projector augmented wave method[24] and VASP-supplied pseudopotentials[25] were used to approximate the core electrons. Dipole correction[26] was applied to the direction orthogonal to the surface, and the D2 empirical van der Waal correction[27] was applied. The substrate was approximated by a slab consisting of 160 Cu atoms arranged in four layers which was optimised prior to introduction of the AP molecule. After this stage, the AP molecule was introduced just above the surface atoms, and further optimisations were done by allowing the atoms of the molecule and the top two surface layers to relax, while keeping the lower two layers frozen. The bottom layers

of the slab were not expected to change much during an optimisation, so by freezing them in position, the expense of the calculations was greatly reduced.

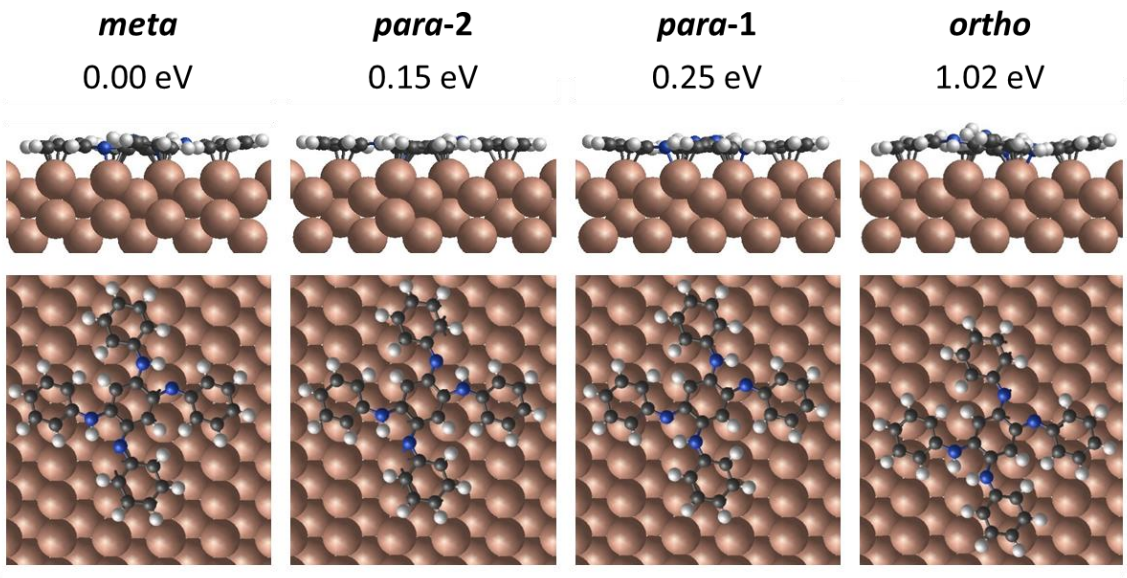

Figure 4.12 Optimised geometries and relative energies of AP adsorbed on a Cu(110) slab. *Meta*-AP adopts the lowest energy, followed by two non-degenerate *para*-AP, and finally, *ortho*-AP is energetically unflavoured.

AP/Cu(110) Optimisations

The *ortho*-AP, *meta*-AP, and *para*-AP structures were adsorbed on the Cu(110) slab and optimised. The results are shown in Figure 4.12. There are a number of points of interest common to all of the optimised geometries. Firstly, the 4-fold coordination site is the favoured position for the central carbon ring, and this agrees with the experimentally determined adsorption position (section 4.5). Also in agreement with this experiment: the main molecular axes, through diagonally opposite phenyl groups, align with the [-110] and [001] high symmetry directions of the substrate. Additionally, the molecules all adopt an approximately planar geometry, with all five of the ring systems facing the Cu(110) surface atoms. This indicates that any steric factors affecting the shape of the molecule (as seen in the gas phase calculations) are overcome by the more favourable interaction of the π-electron systems with the electronic states of the metallic surface.

In agreement with the experimental observation of two equivalent switching species (each of which has two states), we see that for *meta*-AP and *ortho*-AP, there are four possible adsorption configurations. Since these AP/Cu(110) structures are symmetrically equivalent we

can say that they are degenerate. For *para*-AP, however, we see that identical substituents of cyclohexadiene ring (imino or amino) can lie parallel or perpendicular to the [-110] direction. This gives rise to two, non-degenerate states, *para*-1 and *para*-2, each of which has two possible (energy equivalent) configurations. This, as we will see, will have consequences if the reaction pathway includes a *para*-AP configuration.

With these observations in mind, we can now consider the lowest energy AP configuration on the surface. As we know that the lowest energy structure has been studied experimentally (see annealing experiment above), comparison to the theoretical result will confirm which AP configuration (*meta*/*ortho*/*para*) is active for switching. In relative terms, *meta*-AP is the most stable structure. This is followed by *para*-AP, which, for the state where the amino groups are perpendicular/parallel to the [-110] direction, has an energy 0.15/0.25 eV higher than that of *meta*-AP. The *ortho* configuration has a significantly higher optimised energy of 1.02 eV, relative to *meta*-AP. This finding is somewhat surprising: not only is it at odds with the gas phase calculation (which found that *ortho*-AP is most stable in the presence of Cu), but the absence of a Lewis structure for the gas-phase *meta* compound means that it was originally not expected. Nevertheless, this is the lowest energy and hence favoured configuration. This stabilisation likely comes from the fact that unpaired electrons (see Figure 4.2) in this conventionally forbidden structure lower its energy further via donation or acceptance from the surface[28].

At this stage, *ortho*-AP is discarded henceforth on the basis of these energetic arguments, and the mechanism is determined based on the *meta*-AP and *para*-AP structures.

STM Image Simulation

In order to reconcile the experimentally observed differences in contrast of the lobes of the molecule with the optimised structures, STM images were simulated based on the *meta*-AP and *para*-AP (lowest energy) geometries. This was done within the bSkan software package[29,30] using the Tersoff-Hamann approach. In this model, the tip apex is approximated by a spherical function, and the charge within an energy window is integrated to build up a picture which resembles the STM image (see details in Chapter 2). The theoretical AP/Cu(110) STM images were calculated by integrating the states between the Fermi energy (E_f) and (E_f - 0.2 eV) in order to simulate the typical tunnelling conditions when imaging the molecule in a stable form (i.e. not switching). The resultant images are displayed alongside an experimental image and

the ball and stick model in Figure 4.13. The original output images from bSkan showed, qualitatively, the expected outcome but were unrealistically resolved (showing individual atoms in the AP molecule). A post-processing step of convoluting the images with a Gaussian function of width 3 Å was therefore taken to simulate the tip convolution effects seen in STM experimental images.

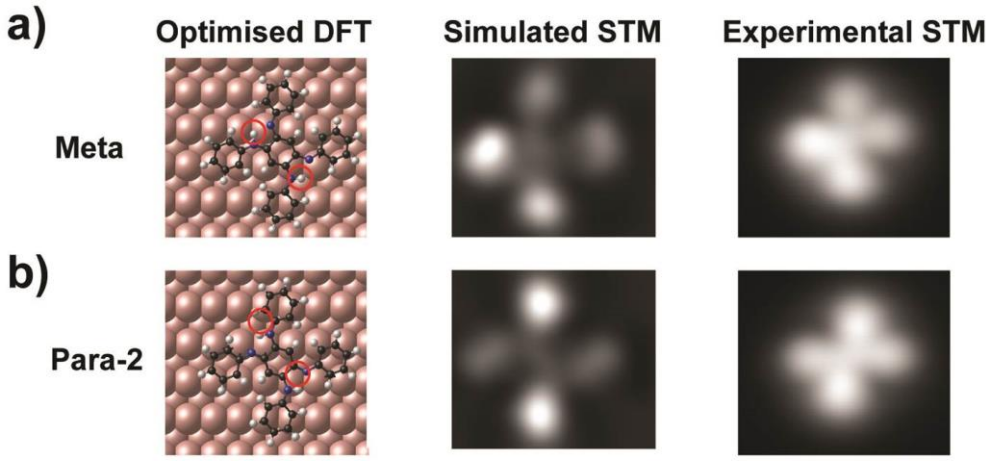

Figure 4.13 Simulated STM images of (a) *meta*-AP and (b) *para*-AP alongside the optimised models and experimental data for comparison (*meta*: I = 2.40 nA; V = -0.18 V. *para*: I = 2.20 nA; V = -0.18 V)

As can be seen in Figure 4.13a, the simulated image of *meta*-AP possesses two adjacent lobes with similar bright contrast, in agreement with the experimentally obtained topography. From this, and the fact that it adopts the lowest energy, we can conclude that *meta*-AP is the molecular switch present on Cu(110). Comparison to the optimised structure shows that the position of the bright lobes corresponds to the side groups on which an amino hydrogen atom is present. In the reverse case, in which the H atoms occupy the opposite nitrogen atoms, the brightness in the molecule would be transferred to the other two lobes. This proves that the mechanism for the switch is tautomerisation of these H atoms from the amino groups to the adjacent imino groups. The reaction is accompanied by electronic reordering of the molecule and is manifested in the STM images as a shift in brightness from one side of the molecule to the other. Besides its relative energetic instability, another strong argument for ruling out the other possible *ortho*-AP structure is that this tautomerisation reaction would be highly unlikely due to the greater distance the H atoms have to move (2.3 Å in *meta*-AP compared to 4.9 Å in *ortho*-AP).

Reaction Pathway

After confirming the switching mechanism as a H-tautomerisation between two equivalent *meta*-AP states, we now turn to the determination of the reaction pathway. There are two conceivable options for the tautomerisation reaction: a concerted transfer of both H atoms simultaneously; or a sequential process in which one proton is transferred, followed by the other. By calculating which process has the smallest activation barrier, we can determine the most likely reaction pathway for the switching process.

Barrier heights were determined using the nudged elastic band (NEB) method. Described briefly, this method involves optimisation of a number of intermediate geometries between the initial and final optimised geometries of the molecule. These geometries define a path for the reaction and their structures are initially guessed by a linear interpolation between the start and end points. The potential energy and gradient is evaluated for each point along this elastic band using DFT. The force at each point is then calculated and the geometry is allowed to optimise further in the direction perpendicular to the band. Convergence of the calculation leads to a description of the lowest energy path over a potential energy surface between the initial and final states of the system. We use the Climbing Image NEB method, where the point with the highest energy is also moved along the band towards higher energy, so that at convergence, it represents the saddle point and gives the exact energy of the transition state. A more in depth description is given in reference[31].

There were eight geometries between the start and end points for the calculations on AP which were determined using the VASP TST Tools package. After a rough indication of the barrier was obtained, further refinement was carried out by performing a further NEB calculation with more points over the interval in which the maximum occurred.

Figure 4.14 considers a concerted *meta* → *meta* tautomerisation process in which the final state is equivalent to the initial state but rotated by 180°. We can see that, instead of a single activation barrier, there exist two sequential barriers separated by a local energy minimum. This implies that the protons are transferred one after another rather than simultaneously and hence the sequential mechanism is active. The local minimum therefore corresponds to the formation of a *para*-AP reaction intermediate, as determined by the DFT calculations.

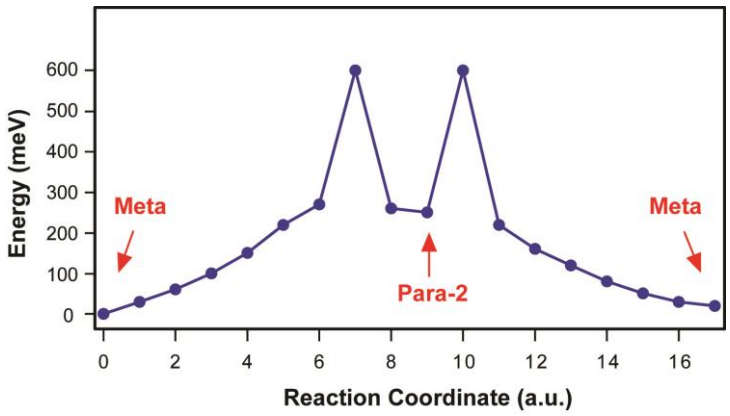

Figure 4.14 Converged reaction pathway for the concerted double proton *meta*-AP to *meta*-AP mechanism. The structure at the halfway point is *para*-2 indicating that a sequential mechanism is preferred.

The transfer of one proton to form *para*-AP has two possibilities due to the existence of two non-degenerate *para*-AP adsorption configurations. The sequential process was therefore investigated by performing two NEB calculations in which the *meta*-AP acts as the initial state, and each of the *para*-AP states as the final state. The result is shown in Figure 4.15 and, for ease, the *para*-AP configuration in which opposite amino groups are parallel or perpendicular to the [-110] direction are defined as *para*-1 and *para*-2, respectively.

The lowest energy and, hence, favoured reaction pathway is that in which *para*-2 acts as an intermediate. With a barrier height of 0.42 eV, this agrees qualitatively with the experimentally determined value of 0.35 eV. The reason for the discrepancy is likely due to the GGA's tendency to overestimate energies. The potential energy barrier involving the *para*-1 intermediate requires 0.52 eV and hence is unlikely to describe the reaction pathway.

The observed switching process can therefore be summarised. Firstly, inelastic electron excitation of *meta*-AP forms a *para*-AP intermediate. This unstable configuration then quickly relaxes to one of the lowest energy *meta*-AP states by either return of the first proton to its original position (no switch observed), or by transfer of the second proton to the opposite imino group (switch observed).

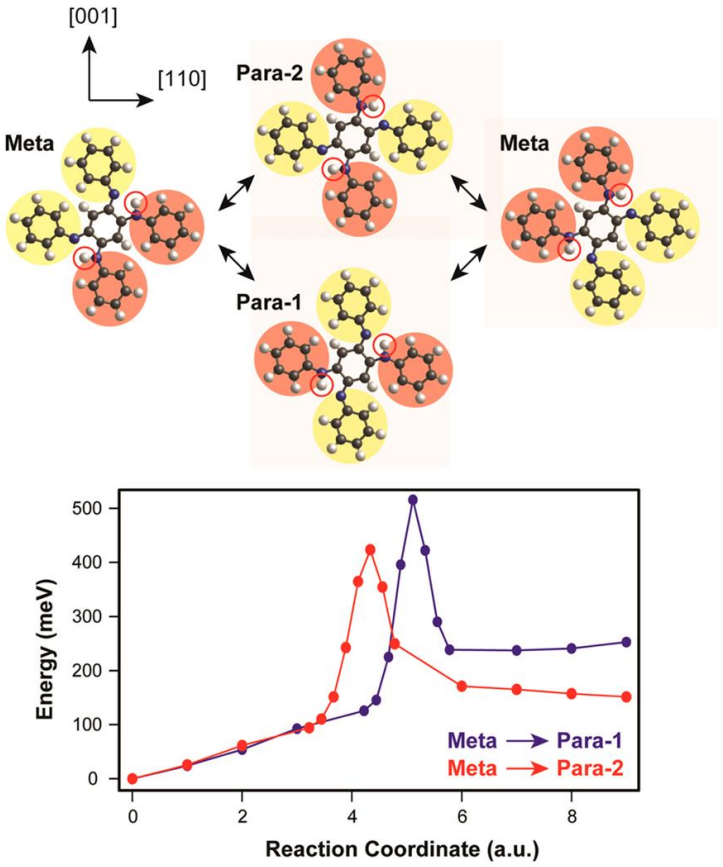

Figure 4.15 (Top) Reaction pathways for *meta*-to-*meta* transition. The symmetry of the substrate imposes a non-degeneracy on the two pathways. (Bottom) Potential energy diagram calculated using the nudged elastic band method indicates that the *para*-2 pathway is the lowest energy and hence favoured route for H-tautomerisation.

This mechanism can also be backed up by a rare, isolated experimental observation of the lowest energy reaction intermediate stabilised on the surface. During rapid switching of the molecule it was found that the current trace was disrupted. By stopping the manipulation and reimaging the molecule, it was found that a configurational change had occurred which showed opposite lobes, perpendicular to the [-110] direction, with matching bright contrast. As shown in Figure 4.13b, the experimental STM image, along with the simulated STM image for the lowest energy *para*-AP intermediate, confirms that this species is present. Further imaging of this unstable configuration returned it to the preferred *meta*-AP state.

4.8 Discussion and Conclusion

The above experiments illustrate that AP and AT can be easily deposited onto a metallic surface, and display a range of different configurations. The lowest energy forms of these molecules were identified, and their switching properties were investigated. Both molecules

display conductance bistability above a voltage threshold of 0.35 eV. Rigorous analysis of the switching behaviour under different tunnelling conditions showed that switching events are triggered by inelastic scattering of a single electron. Computational modelling allowed us to attribute the lowest energy structure to the *meta*-AP configuration and, although not included in the calculations, the same is likely true for AT. Further modelling confirmed that the underlying mechanism is due to a sequential H-tautomerisation reaction via a *para*-AP intermediate involving transfer of H atoms from amino to imino functional groups.

Until now, the H-tautomeric switches that have been studied involved the proton transfer process occurring inside the central macrocycle system of porphyrin type molecules. This implied that strict rules apply to the environment in which this process could occur, such as protective encapsulation, two-dimensionality, and the absence of deformation in the chemical structure. The quinone derivatives investigated in this work break these rules, and bring variation and versatility to the conception of molecular switches in general. Significantly, since the switching mechanism in the further functionalised AT molecule is not compromised, the switching moiety can be thought of as a basis for the construction of molecular switches with properties tailored to specific criteria or applications.

4.9 References

1. G. J. Simpson, S. W. L. Hogan, M. Caffio, C. J. Adams, H. Früchtl, T. van Mourik, and R. Schaub, *Nano Lett.*, 2014, **14**, 634–639.

2. R. Nietzki and E. Hagenbach, *Ber. Dtsch. Chem. Ges.*, 1887, **20**, 328.

3. C. Kimich, *Ber. Dtsch. Chem. Ges.*, 1875, **8**, 1026–1032.

4. P. Ruggli and F. Buchmeier, *Helv. Chim. Acta*, 1945, **28**, 850–863.

5. S. Frantz, J. Rall, I. Hartenbach, T. Schleid, S. Zális, and W. Kaim, *Chem. Eur. J.*, 2004, **10**, 149–154.

6. J. Rall, A. F. Stange, K. Hübler, and W. Kaim, *Angew. Chem. Int. Ed. Engl.*, 1998, **37**, 2681–2682.

7. Y.-B. Huang, G.-R. Tang, G.-Y. Jin, and G.-X. Jin, *Organometallics*, 2008, **27**, 259–269.

8. M. Elhabiri, O. Siri, A. Sornosa-Tent, A.-M. Albrecht-Gary, and P. Braunstein, *Chem. Eur. J.*, 2004, **10**, 134–141.

9. O. Siri, P. Braunstein, M.-M. Rohmer, M. Bénard, and R. Welter, *J. Am. Chem. Soc.*, 2003, **125**, 13793–13803.

10. K. Ujike, S. Kudoh, and M. Nakata, *Chem. Phys. Lett.*, 2005, **409**, 52–56.

11. H. Rumpel and H. H. Limbach, *J. Am. Chem. Soc.*, 1989, **111**, 5429–5441.

12. H. Rumpel and G. Zachmand, *J. Phys. Chem.*, 1989, **93**, 1812–1818.

13. B. C. Stipe, M. A. Rezaei, and W. Ho, *Science*, 1998, **279**, 1907–1909.

14. T. Kumagai, F. Hanke, S. Gawinkowski, J. Sharp, K. Kotsis, J. Waluk, M. Persson, and L. Grill, *Nat. Chem.*, 2014, **6**, 41–46.

15. D. J. Coulman, J. Wintterlin, R. J. Behm, and G. Ertl, *Phys. Rev. Lett.*, 1990, **64**, 1761–1764.

16. J. Jensen, F. Besenbacher, E. Laesgaard, and I. Stensgaard, *Phys. Rev. B*, 1990, **41**, 10233–10236.

17. Y. Zhao and D. G. Trulhar, *Theor. Chem. Acc.*, 2008, **120**, 215–241.

18. M. J. Frisch, G. W. Trucks, H. B. Schlegel, G. E. Scuseria, M. A. Robb, J. R. Cheeseman, G. Scalmani, V. Barone, B. Mennucci, G. A. Petersson, H. Nakatsuji, M. Caricato, X. Li, H. P. Hratchian, A. F. Izmaylov, J. Bloino, G. Zheng, J. L. Sonnenberg, M. Hada, M. Ehara, K. Toyota, R. Fukuda, J. Hasegawa, M. Ishida, T. Nakajima, Y. Honda, O. Kitao, H. Nakai, T. Vreven, J. J. A. Montgomery, J. E. Peralta, F. Ogliaro, M. Bearpark, J. J. Heyd, E. Brothers, K. N. Kudin, V. N. Staroverov, R. Kobayashi, J. Normand, K. Raghavachari, A. Rendell, J. C. Burant, S. S. Iyengar, J. Tomasi, M. Cossi, N. Rega, N. J. Millam, M. Klene, J. E. Knox, J. B. Cross, V. Bakken, C. Adamo, J. Jaramillo, R. Gomperts, R. E. Stratmann, O. Yazyev, A. J. Austin, R. Cammi, C. Pomelli, J. W. Ochterski, R. L. Martin, K. Morokuma, V. G. Zakrzewski, G. A. Voth, P. Salvador, S. Dannenberg, J. J. Dapprich, A. D. Daniels, Ö. Farkas, J. B. Foresman, J. V. Ortiz, J. Cioslowski, and D. J. Fox, *Gaussian 09*, Wallingford CT, USA, Rev. A.02., 2009.

19. M. K. Holloway, C. H. Reynolds, and K. M. Merz, *J. Am. Chem. Soc.*, 1989, **111**, 3466–3468.

20. G. Kresse and J. Furthmüller, *Phys. Rev. B*, 1996, **54**, 11169–11186.

21. G. Kresse and J. Furthmüller, *J. Comput. Mat. Sci.*, 1996, **6**, 15–50.

22. G. Kresse and J. Hafner, *Phys. Rev. B*, 1993, **47**, 558–561.

23. J. P. Perdew, K. Burke, and M. Ernzerhof, *Phys. Rev. Lett.*, 1996, **77**, 3865–3868.

24. P. E. Blöchl, *Phys. Rev. B*, 1994, **50**, 17953–17979.

25. G. Kresse and D. Joubert, *Phys. Rev. B*, 1999, **59**, 1758–1775.

26. J. Neugebauer and M. Scheffler, *Phys. Rev. B*, 1992, **46**, 16067–16080.

27. J. Grimme, *J. Comp. Chem.*, 2006, **27**, 1787–1799.

28. M. Bieri, M.-T. Nguyen, O. Gröning, J. Cai, M. Treier, K. Aït-Mansour, P. Ruffieux, C. A. Pignedoli, D. Passerone, M. Kastler, K. Müllen, and R. Fasel, *J. Am. Chem. Soc.*, 2010, **132**, 16669–16676.

29. W. A. Hofer and J. Redinger, *Surf. Sci.*, 2000, **447**, 51–61.

30. W. A. Hofer, *Prog. Surf. Sci.*, 2003, **71**, 147–183.

31. H. Jónsson, G. Mills, and K. W. Jacobsen, in *Classical and Quantum Dynamics in Condensed Phase Simulations*, eds. J. Berne, G. Ciccotti, and D. F. Coker, World Scientific, B., 1998.

5 High Coverage of Azophenine on Cu(110)

5.1 Summary

The self-assembly of the AP molecule on a Cu(110) surface is investigated in this chapter. The ordering of extended molecular islands is discussed in terms of intermolecular interactions and molecule-Cu interactions. The absence of switching behaviour of individual AP molecules within islands is also addressed.

5.2 Introduction

In the previous chapter, the azophenine (AP) molecule was introduced, along with two other quinone derivatives. The study of this molecule in its isolated form revealed that the molecule is active as a H-tautomeric switch. In this chapter, we focus on the high coverage regime of AP in order to investigate the possibility of constructing ordered arrays of switching molecules. Owing to their size compared to conventional electronic components, such an assembly of molecules would mean that the density of active components could be increased significantly, and allow construction of, for example, much more efficient memory storage devices. We also look at how both intermolecular interactions and interaction with the substrate affect the growth, ordering, and switching behaviour of AP on Cu(110) at high coverage. The study of high density arrays of molecules raises the need to introduce briefly the processes involved in self-assembly of organic molecules on a metallic substrate. Another relevant area to be introduced is the incorporation of metal atoms into molecular arrays.

5.2.1 Self-assembly

Molecular self-assembly is the spontaneous association of molecules under equilibrium conditions into stable, structurally well-defined aggregates joined by noncovalent bonds[1]. Ubiquitous in biological systems, self-assembled structures can be found in the phospholipid bilayer[2] of cell membranes, as well as the nucleic acids[3] on which all life depends. As well as applications in the field of biology, self-assembly has been found useful in areas such as colloidal science[4], molecular recognition[5], and polymer science[6]. Of course, self-assembly is a

general process and applies mostly to three-dimensional systems. We limit ourselves, however, to the interesting case where we have spontaneous ordering of molecular structures on the surface of a solid. This allows for direct visualisation and study using scanning probe techniques.

The resulting structure of a self-assembled array of molecules is determined by a complex interplay between substrate-adsorbate interactions, lateral interactions between adsorbates, and intramolecular interactions. The latter is usually only important when considering relatively large molecules such as proteins.

Substrate-adsorbate interactions play an important role in the production of ordered structures. For physisorption, where the molecule is held by van der Waal and dipole interactions, the bound species may diffuse across the surface and interact with other molecules or surface defects. In the case of chemisorption, a covalent chemical bond is produced between the molecule and surface and often leads to immobilisation and distortion of the adsorbed species. Depending on the adsorption process, different degrees of ordering can be observed. Aromatic molecules, for example, may have rather large energies of adsorption due to favourable interaction between the π-systems and the underlying substrate. Despite this, diffusion on the surface is still possible due to a relatively low barrier for this process and it is therefore possible to see self-assemblies of large molecules. Another factor to consider is the reactivity of the substrate. If the substrate is too reactive, decomposition of the target molecule can occur. It is therefore necessary to choose a suitable surface. For this study, the relatively inert Cu(110) surface has been chosen not only for its low reactivity, but for its symmetry which matches the two high symmetry axes of the molecule of interest.

The substrate can also be chosen to direct the geometry of the target molecules in certain ways. Molecules containing functional groups with a high affinity for the surface often adsorb in such a way as to maximise this interaction. A prominent example of this are thiols on Au(111), which often form densely packed self-assembled monolayers by adsorbing in an upright position with a strong S-Au bond at their base[7]. The geometry of adsorbed aromatic molecules is commonly planar due to favourable interaction between the π-electrons and the underlying substrate. An example of this has already been seen in the previous chapter for AP and AT, and this study will be furthered here by looking at the structure of AP at high coverage.

Adsorbate-adsorbate interactions also play a major role in the ordering of molecules on a metal surface. Lateral hydrogen bonding, dipole-dipole interaction, van der Waals interactions,

π-π bonding, and metal coordination are all determining factors in the morphology of a self-assembled molecular array. Hence, by careful selection of the chemical structure of the building blocks, the characteristics of the self-assembled structures such as size, shape, reactivity, and porosity can be controlled.

5.2.2 Metal-Organic Coordination Networks

Of particular interest in this chapter (as will become evident later) is the growth of self-assembled structures via metal complexation to produce so called metal-organic coordination networks (MOCN). These generally consist of very robust structures due to the strong metal ligand bonding which holds the network together. Examples from the literature include coadsorption of Fe with varying length dicarboxylic acids[8]. The authors found that by varying the ratio of molecules to metal atoms, the pore size can be controlled, and this could facilitate the accommodation of guest molecules (C_{60} in this case). Another case showed that co-deposition of metal atoms is not necessary in order to produce MOCNs. Instead, the free surface adatoms facilitated the growth of one dimensional metal organic chains consisting of trimesic acid and Cu adatoms on a Cu(100) surface[9].

It is known that a favourable interaction between Cu and AP exists. As discussed in Chapter 4, AP can act as a bidentate ligand in the solution phase to form complexes with copper. Furthermore, our gas phase calculations have shown that a favourable interaction between the amino/imino groups of AP and Cu/Cu^+ species exists. Hence, it can *a priori* be expected that the chemical coupling of AP and the copper substrate is strong. Indeed, it is shown in this chapter that it is possible to grow a two-dimensional condensed phase which consists not only of AP but with the incorporation of additional Cu adatoms.

5.3 High Coverage AP

The experimental system considered in this chapter is the AP molecule deposited on the Cu(110) surface as introduced in the previous chapter. The molecules are deposited onto a surface held at room temperature, meaning that they are able to diffuse laterally to produce self-assembled two dimensional islands. With a short exposure of the molecules to the cleaned surface, we primarily see adsorption at the step edges. This is in agreement with the higher reactivity of step edge sites compared to terraces, and therefore the molecules are more

strongly bound at these sites. Furthermore, we can see in Figure 5.1a that the step sites which have a termination in the rows running in the [-110] direction are preferred over those which have a termination in the [001] direction. Further deposition results in saturation of the whole step edge as seen in Figure 5.1b.

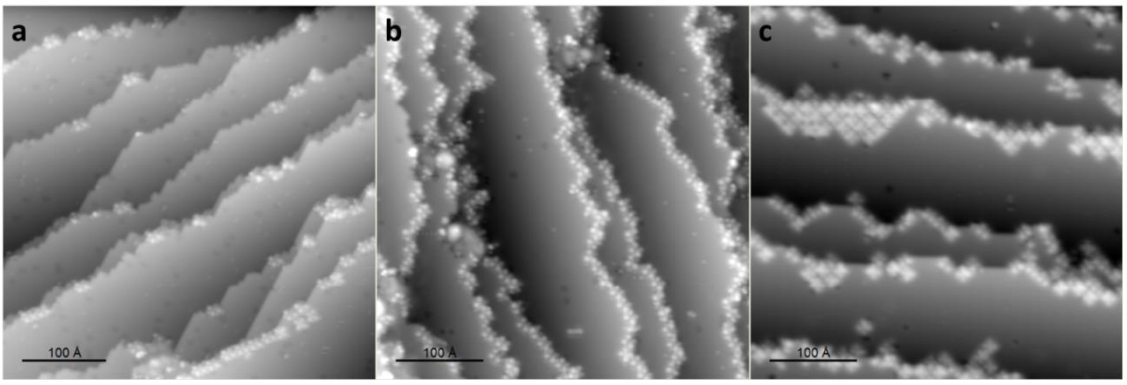

Figure 5.1 STM images showing increasing AP coverage (from left to right). (a) At first only a few molecules decorate the otherwise bare step edges (I = 0.38 nA; V = 1.28 V). (b) Next, the step edges are saturated but the terraces are bare (I = 0.51 nA; V = 0.20 V). (c) Finally, growth of molecular islands onto the step edges occurs (I = 0.12 nA; V = 0.96 V).

The molecules which lie across a step edge generally have two of their peripheral phenyl groups adsorbed on the upper terrace while the other two are on the lower terrace. This contorted geometry means that switching in these molecules in not observed and it is not possible to determine which configuration (*ortho*/*meta*/*para*) they adopt. Although step-edges are more reactive, the molecules are generally intact and no signs of decomposition are observed. Once saturation coverage of the step edges is achieved, single layer growth of molecular islands over the Cu(110) terraces occurs. The onset of this is seen in Figure 5.1c. It is also seen that defects on the terraces of the surface stabilise the molecules upon deposition. Correspondingly, we see large molecular islands both in the middle of terraces and growing from a step edge.

An example of the large islands extending from growth at a defect can be seen in Figure 5.2. We can see that the molecules within the islands are ordered into a periodic array which extends in two high symmetry directions. Determination of the [-110] and [001] directions of the underlying substrate (top of Figure 5.2) reveals that the high symmetry directions of the islands are ±45° rotated compared to the [-110] direction. The square unit cell has a length of 14.8 Å.

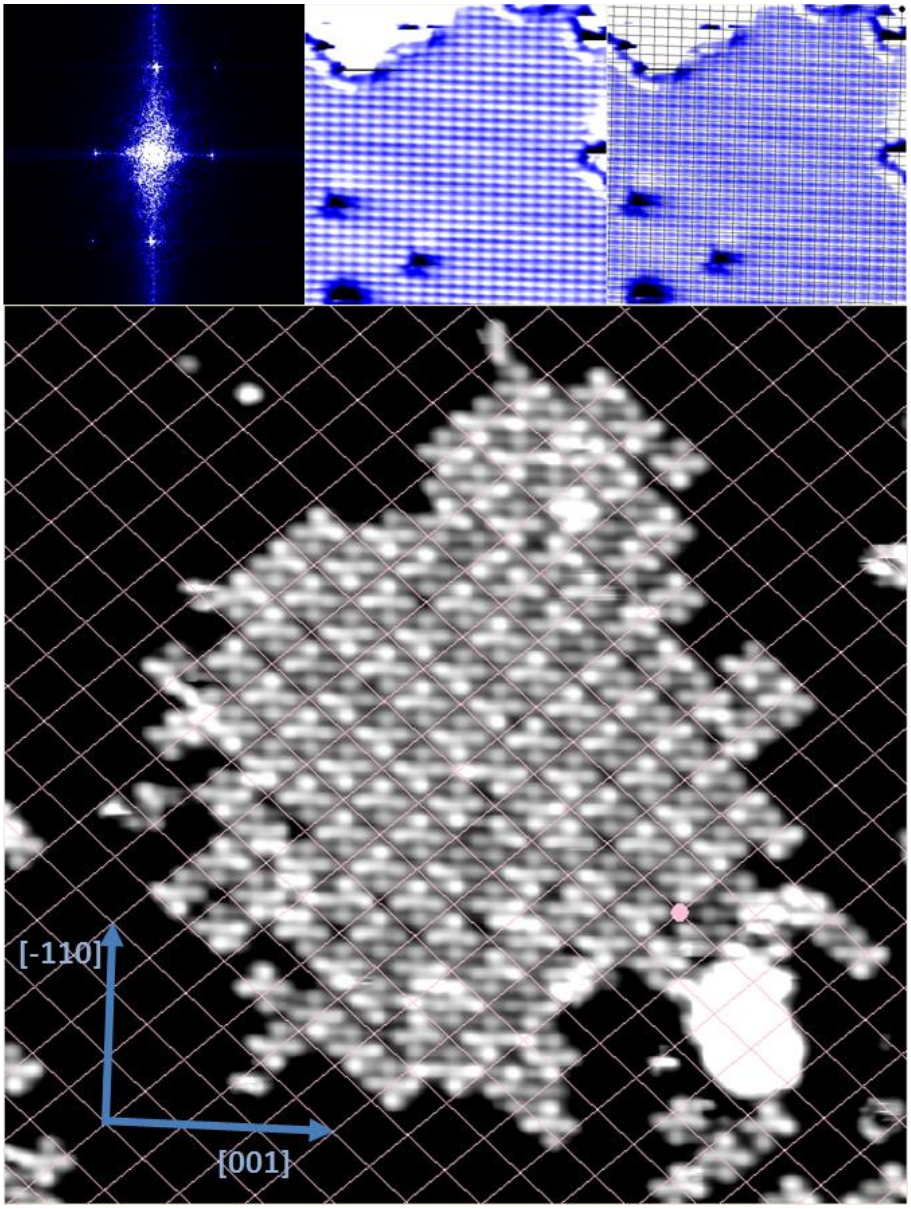

Figure 5.2 STM image of a typical AP molecular island (I = 0.10 nA; V = -0.195 V). The underlying surface directions are determined from an atomically resolved image (top; I = 0.84 nA; V = -0.108 V). The molecules all adopt the low energy meta-AP configuration and the high symmetry directions of the island are oriented 45° rotated compared with the [-110] and [001] directions of Cu(110).

The ordering and size of the molecular islands is highly dependent on the surface temperature and the flux of incoming molecules when deposition is performed. Figure 5.3 shows two cases where these conditions were different and the result is, in one case, large islands with long range order, and in the other case, disordered molecules which are clustered together in small groups. In Figure 5.3a the evaporation temperature of AP was held at 117 °C, the Cu(110) temperature was 40 °C, and the exposure time was 20 minutes. In contrast, for the sample preparation shown in Figure 5.3b, AP was evaporated at 130 °C for 5 minutes while the surface temperature was held at 15 °C. In the case where a lower temperature is used the rate of

evaporation of AP is low and molecules impinging on the surface have freedom to explore the surface before binding to a defect or another molecule. This leads to controlled growth of islands where, in the limiting case, molecular islands are grown from a single nucleation point which increases in size one molecule at a time. In the high evaporation temperature (hence high flux) case, AP molecules arrive at the surface and after a short time bind to another nearby molecule. This dimer is then likely immobilised, and the result is many small islands with no long range crystallinity. Furthermore, the higher temperature of the sample in the low flux case means that deposited molecules have more energy than the high flux (low surface temperature) case to diffuse before becoming immobilised.

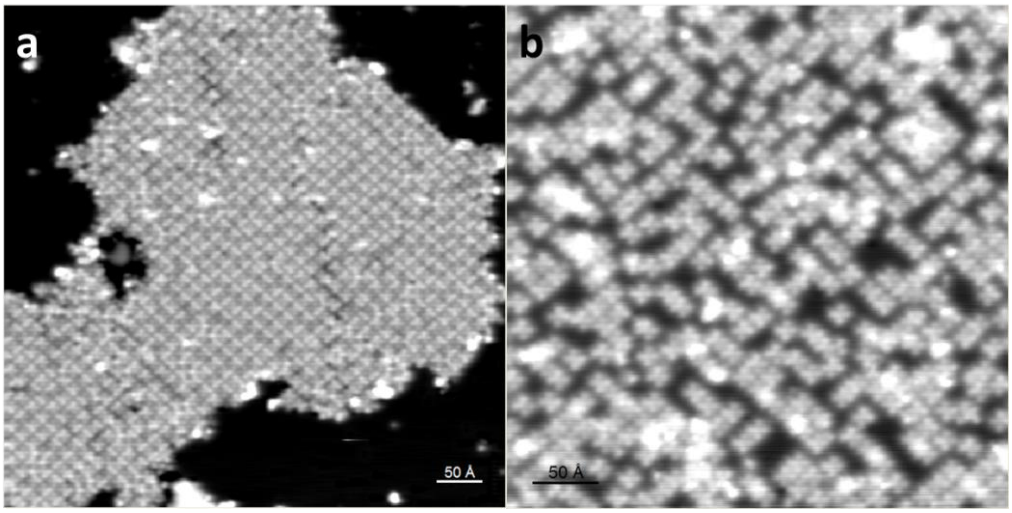

Figure 5.3 Effects of surface temperature and flux on the growth of AP islands. (a) STM image of large ordered island of AP grown using low evaporation temperature and high surface temperature (I = 0.15 nA; V = -0.05 V). (b) STM image of disordered AP with similar coverage to (a), which is the result of low surface temperature and high evaporation temperature during deposition (I = 0.06 nA; V = 0.06 V).

In the knowledge that slow and controlled growth leads to large, well ordered islands, we now concentrate on the detailed structure of these AP arrays, such as shown in Figure 5.3.

5.3.1 Adsorption Configuration in the Condensed Phase

Figure 5.4a shows a high-resolution STM image acquired over a large and ordered island of AP. It can be seen that the AP molecules have the same topographic signature when compared to the isolated case discussed in Chapter 4. That is, two lobes display bright STM contrast (corresponding to aminophenyl functional groups), and the opposite two lobes have lower apparent height (corresponding to iminophenyl side groups). An additional parallel that can be drawn is that the main molecular axes (running through diagonally opposite lobes) lie along

the high symmetry [-110] and [001] directions of the underlying Cu(110). The observed similarities between AP molecules in islands and those which are isolated lead to the conclusion that we solely have the low energy *meta*-AP configuration present in the condensed phase. Inspection of many molecules within extended islands reveals that all four of the possible *meta*-AP configurations are present (two reflectionally equivalent adsorption species; each with two tautomeric states). Analysis and discussion on the relative population and distribution of these states will follow later in this chapter.

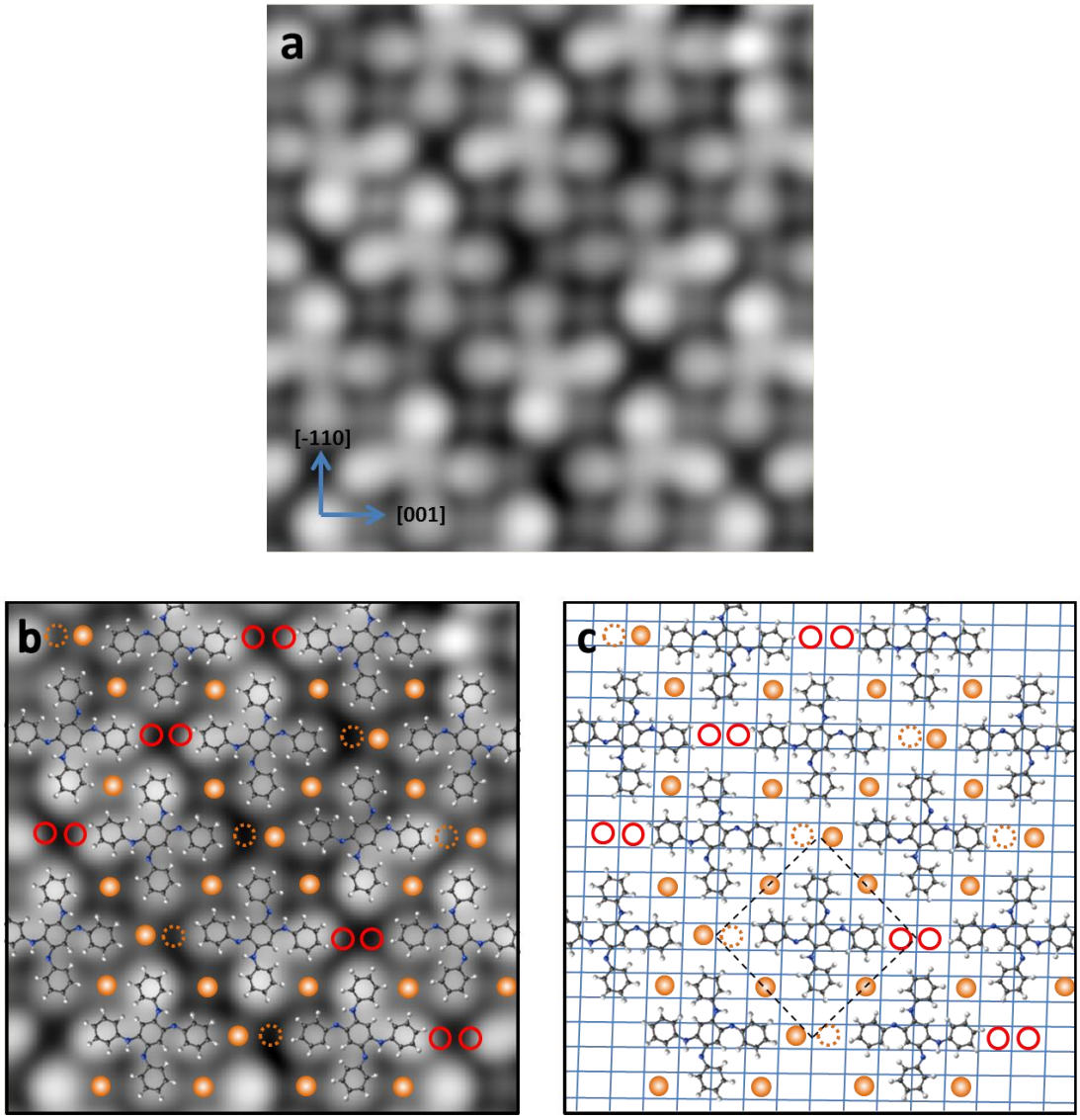

Figure 5.4 (a) STM image displaying AP molecules in a close packed arrangement with uniformly sized species adsorbed in the interstitial sites which are assigned as Cu adatoms (I = 3.00 nA; V = 0.02 V; image width is 53 Å). (b) Same image overlaid with model. (c) Model with Cu(110) lattice grid. The Cu adatoms are periodically spaced and are assigned to the four-fold coordination site. The unit cell for the (4√2 × 3√2)R45 overlayer structure is indicated in black (alternatively the molecular adlayer can be described as a centred (8 × 6) structure).

In contrast to isolated AP, we see the inclusion of additional circular features in the interstitial sites of the molecular islands. These additional features are unexpected because AP at low surface coverage appears in the STM images as an isolated species with no additional adjoined species. We can see in Figure 5.4a that the features are uniform in size and occupy the spaces between the lobes of adjacent or diagonally opposite molecules. Furthermore, there are positions in which the features are present and those in which their absence is observed by a dark depression. The fact that we observe both occupied and vacant sites indicates that the features in the intermolecular interstices are as a result of adsorbed species rather than an electronic effect or a tip convolution effect. Small pollutant adsorbates, such as CO, H_2, H_2O or O_2 are all candidates which could explain the identity of the circular features. However, we can rule these out on considerations of cleanliness of our samples (background pressure $< 5 \times 10^{-11}$ mbar). The additional features can, however, be reliably attributed to Cu adatoms. The reason for this is two-fold: 1) the uniform size and shape of the features mean that a single species is present, and 2) it is known (see section 5.2.2) that AP has a strong interaction with Cu which would stabilise their presence in the islands.

The adsorption site of the Cu adatoms is unclear due to difficulties in our attempts to resolve both the molecular islands and the underlying substrate simultaneously. However, it is likely that the incorporated Cu atoms conform to the next epitaxial layer of the substrate. As seen if Figure 5.4c, the lattice grid of Cu(110) shows that all sites occupied by the additional protrusions are identical. Since we assign these features to Cu adatoms, it makes sense to consider that they are adsorbed in their energetically preferred location, i.e. the four-fold coordination site. With this hypothesis (which implies that Cu-Cu interaction is stronger than molecule-Cu interaction) the high resolution image indicates that AP is hence not adsorbed as in the isolated case (four-fold site), but shifted to the short bridge site.

As seen from the model in Figure 5.4c, each molecule has, at each side, a site where a Cu resides. At the corner sites where four molecules meet, there are two possible sites for additional Cu. The maximum occupancy of these sites is restricted to one atom. Therefore, we have a maximum of 4 Cu adatoms per overlayer unit cell. In most cases, however, there are 3 adatoms per unit-cell because it is seen later in this chapter that the functional groups of the molecule (amino/iminophenyl) affect the position of this adatom. Specifically, the adatom shows a strong preference to be in close proximity to an iminophenyl group. Since, in any particular molecule, diagonally opposite lobes always contain different functional groups there may only be one adatom at the corner of each overlayer unit-cell. Hence, the unit-cell of the

molecular adlayer is comprised of 1 molecule and 3 Cu adatoms on average. The interstitial sites between directly adjacent molecules are occupied in almost every case, whereas vacant sites are seen more commonly in the sites where four different molecules meet (analysis of these four-fold sites will follow).

There are two possibilities for the origin of the Cu adatoms: 1) freely diffusing Cu atoms on the Cu(110) surface are trapped and incorporated into the islands during growth, or 2) the Cu atoms are abstracted from the surface due to the presence of the AP molecules. In both cases the trapping/extraction process must have a barrier for activation that is overcome at temperatures below room temperature since we do not see Cu adatoms attached to AP when deposition occurs at liquid nitrogen temperatures. If the first case is true, where adatoms are trapped, their density on the surface must be high enough to account for the number incorporated into the islands. In the second case, where adatoms are abstracted, the molecule-substrate interaction must be high enough to allow the abstraction. This process is likely helped greatly by cooperative effects, whereby the abstraction is rendered facile by the presence of more than one molecule. Regardless of their origin (which is unclear at this stage of my research), the Cu adatoms incorporated into the molecular islands have a rather interesting behaviour which depends strongly on the states of the molecules in their immediate environment. Upon analysis of the different possible environments, we see a statistically significant pattern arising (see section 5.3.3).

5.3.2 AP Switching Within the Condensed Phase

Shown in Figure 5.5 are STM images of an ordered island which has been scanned at voltages both above and below the switching threshold of ±0.35 V. Comparison of the two images reveals that at high voltage, molecules have a fuzzy appearance in some instances (circled). This is indicative of rapid switching, between the two tautomeric states of these molecules as the tip passes over them. We note that, in the environment described in section 5.3.1, rotation of AP is sterically prevented, and so the switching observed in this example (and in Chapter 4) must be due to H-tautomerisation rather than just a 180° rotation of the entire molecule.

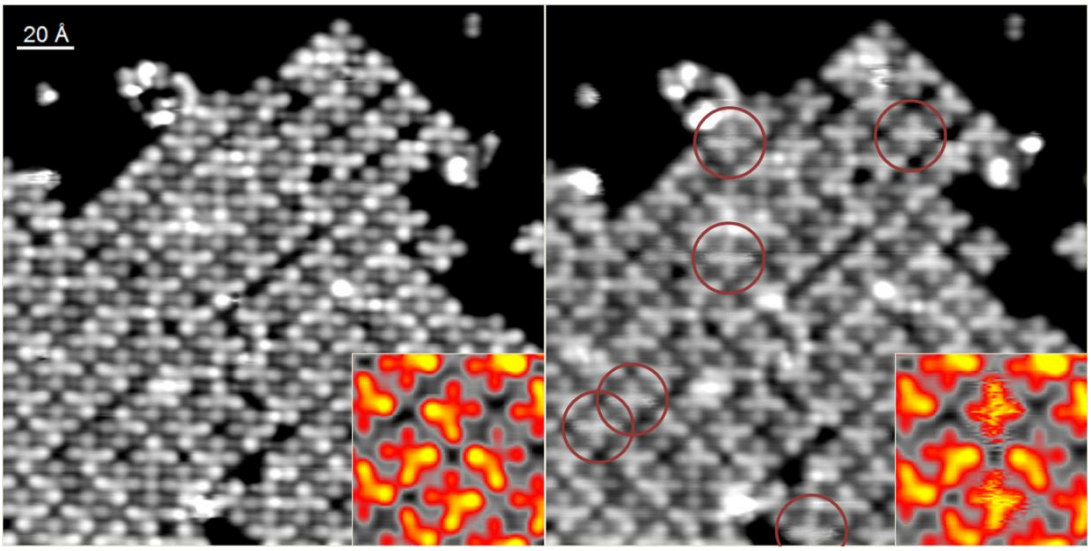

Figure 5.5 Examples of switching molecules within an ordered array of AP. (Left) STM image acquired with a bias below the 0.35 V switching threshold (I = 0.60 nA; V = 0.09 V). (Right) STM image with scanning bias above the switching threshold with switching molecules indicated with red circles (I = 0.60 nA; V = 0.70 V). Insets show a clearer example of switching within an island (Left: I = 1.1 nA; V = 0.19 V; Right: I = 0.22 nA; V = 0.56 V)

Another observation is that only a few examples of switching molecules are seen in the islands; the majority remain in a single state even at elevated scanning bias (even up to 2 V) or following voltage pulses. Possible factors which determine whether a particular molecule is active or inhibited for switching are: the interaction between neighbouring molecules; or the Cu adatoms in the immediate environment of a molecule. In the former, it may be that the state of one molecule has a strong effect on the state of the adjacent molecules such that, when two molecular configurations are beside each other, the possibility of switching is quenched. Alternatively, the presence of Cu adatoms could mean that a particular state of the molecule is preferred due to favourable interaction with amino/imino nitrogen lone pairs. A combination of these (and other) factors may be responsible and, to address this, an in-depth investigation of adatom-molecule (section 5.3.3) and molecule-molecule (section 5.3.4) interactions will be presented.

5.3.3 Interstitial Cu Adatom Analysis

As discussed above, Cu adatoms may be located between two directly adjacent molecules, or in a diagonal position where four different molecules meet. In almost every instance the adjacent sites are occupied with a Cu adatom. We see that both switching and inactive molecules have these sites occupied, and hence, these adatoms have no effect on activating or

hindering the switching property. A significantly higher number of vacant sites are seen when considering the diagonal positions and it is likely that the presence/absence of a Cu adatom will influence the likelihood of switching. We now investigate this.

When considering an interstice at the point where four molecules meet, we can see that there are four lobes (each from a different molecule) surrounding the site. These lobes may either display bright or dim STM contrast which corresponds to aminophenyl or iminophenyl groups, respectively. Since there are four phenyl rings, and two possible states per ring (amino-/bright contrast or imino-/dim contrast), we have a total of 16 distinct environments for the Cu adatom. These configurations are displayed in Figure 5.6, where white/blue corresponds to dim/bright STM contrast.

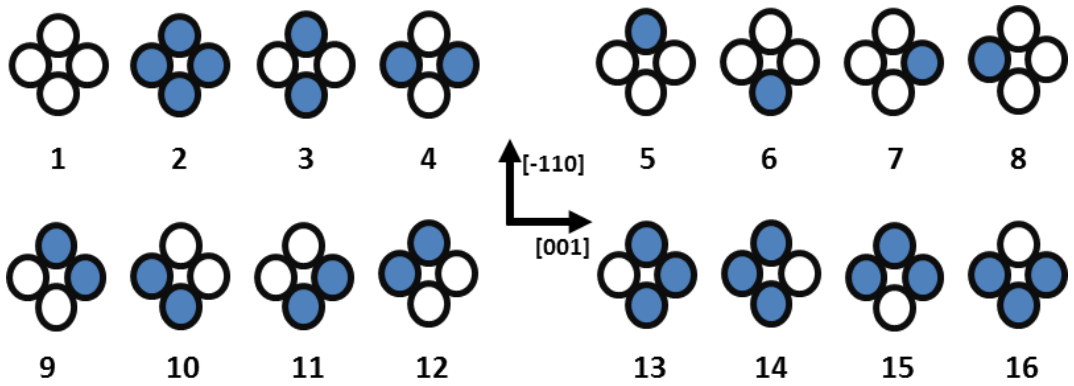

Figure 5.6 The 16 distinct configurations of a four-fold interstitial site. Each circle represents a peripheral phenyl group for a separate molecule. White corresponds to iminophenyl and is imaged dim; blue is an aminophenyl group and is imaged bright. The Cu(110) high-symmetry directions are shown for reference.

Firstly, based on statistical analysis of many STM images, the frequency of occurrence of each configuration was recorded, whereby 267 interstices (where 4 molecules meet) were considered irrespective of the presence or absence of the Cu adatom. The analysis is shown in Figure 5.7 (blue bars). It was found that environments 4 and 7 were most common, and 2 and 3 were least common. These particular configurations do not stand out as special cases, and are not related to each other through symmetry operations. This finding may simply be due to statistical variation, and if more sites had been counted, it may have resulted in an even distribution between all configurations. We also see large variations between symmetrically equivalent environments (for example 5 and 6). One would expect similar occurrence frequencies for these because they are 180° rotations of each other. From this we can say that there is not a strong factor in determining the occurrence frequency of a particular configuration of the 4-way interstice sites.

The second factor which was analysed was the presence or absence of an adatom in these sites. At the same time, it was noticed that there are two possible sites for the Cu atom within a single interstice. These are labelled “left” or “right” and correspond to positions which are closer to one of the two molecules in the [001] direction, as shown in Figure 5.4b.

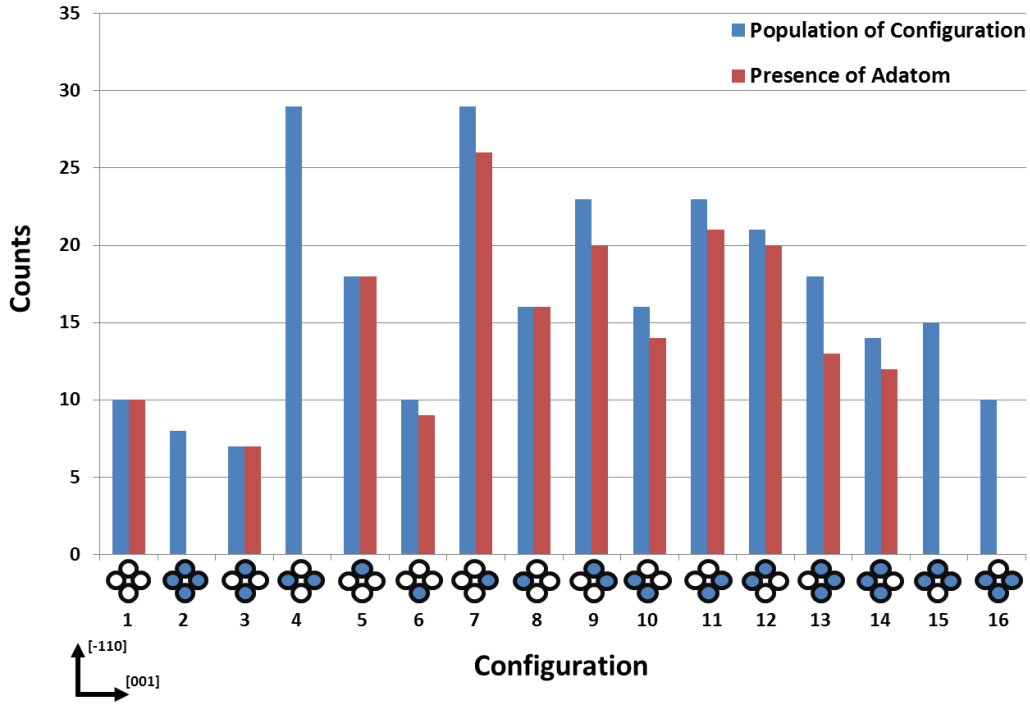

Figure 5.7 Occurrence frequency of the 16 configurations shown in Figure 5.6 (blue). The red bars indicate the number of each configuration which included a Cu adatom.

Among all of the interstitial sites that were analysed, it was found that 4 of the 16 different environments consistently lacked a Cu adatom. These data are shown in Figure 5.7 (red bars). The 4 configurations in which we see a systematic absence of Cu atoms all have a common feature: the pair of diagonally opposite lobes which are parallel to the [001] direction both show bright contrast (i.e. two lobes of blue colour aligned horizontally in the configurations show at the bottom of Figure 5.7). This suggests that these lobes prevent the inclusion/trapping of an adatom. The other two lobes (those parallel to the [-110] direction) seem to have no effect on the presence/absence of a Cu atom because we would expect configurations 3 and 14 to show similar behaviour. Further evidence to suggest that the bright lobes exclude Cu adatoms is seen when we look at the cases in which only one of lobes in the [001] direction is bright and the other one is dim. In these cases (configurations 7-14), the Cu adatom consistently occupies the position which is furthest from the bright lobe.

The above analysis of the Cu adatoms does not reveal any factors which affect the presence of switching in the AP molecules. In the AP examples that switch, there seems to be no consistent configuration of Cu adatoms which are present. It was therefore hoped that investigation into the molecule-molecule interaction would provide an explanation.

5.3.4 Pairwise Analysis of Tautomeric States of AP

The analysis of the included Cu species, discussed above, showed that we can reliably predict where we will find occupied interstices; however this analysis does not explain why molecular switching is activated/inhibited within the molecular islands. A further interesting question that can be addressed is: Does any ordering exist in terms of the configurations of the molecules within the islands? It is clearly seen from the long-range periodicity of the islands that the molecules are well ordered laterally due to their interaction with the substrate. However, when we look specifically at the state (position of the imino and amino groups) of the ordered molecules, it seems at first glance that no long-range order exists. For example, we do not see extended domains consisting exclusively of one of the four possible *meta*-AP states (remember: there are two equivalent, mirror symmetric, adsorption configurations; each of which has two tautomeric states – i.e. 4 states in total). This section looks at this apparent randomness, and reveals that there is strong evidence for an intermolecular potential which has consequences for the growth of these self-assembled structures.

As mentioned, AP can adopt one of four different *meta* configurations when the complete molecule/substrate system is considered. These configurations are shown in Figure 5.8a along with a colour coded arrow which points from the bright amino lobes to the dim imino lobes. By taking an example STM image (see Figure 5.8b) and assigning each molecule with the corresponding coloured arrow, it becomes clear exactly which state each molecule occupies and how these states are distributed. Figure 5.8c shows the image overlaid with colour coded arrows, and it seems that there is a certain degree of clustering of like colours. This may lead one to believe that the molecular states within islands are not completely random and that there is a tendency for molecules with the same state to group together. However, if we compare this to a randomly generated array (produced simply using Excel's random number generator) of coloured arrows, as shown in Figure 5.8d, we can see that there is a comparable amount of clustering. The apparent similarity between the experimental and random case seems to indicate that no (strong) molecule-molecule repulsion or attraction exists. However, the in depth pairwise analysis that follows shows that this naïve observation is erroneous.

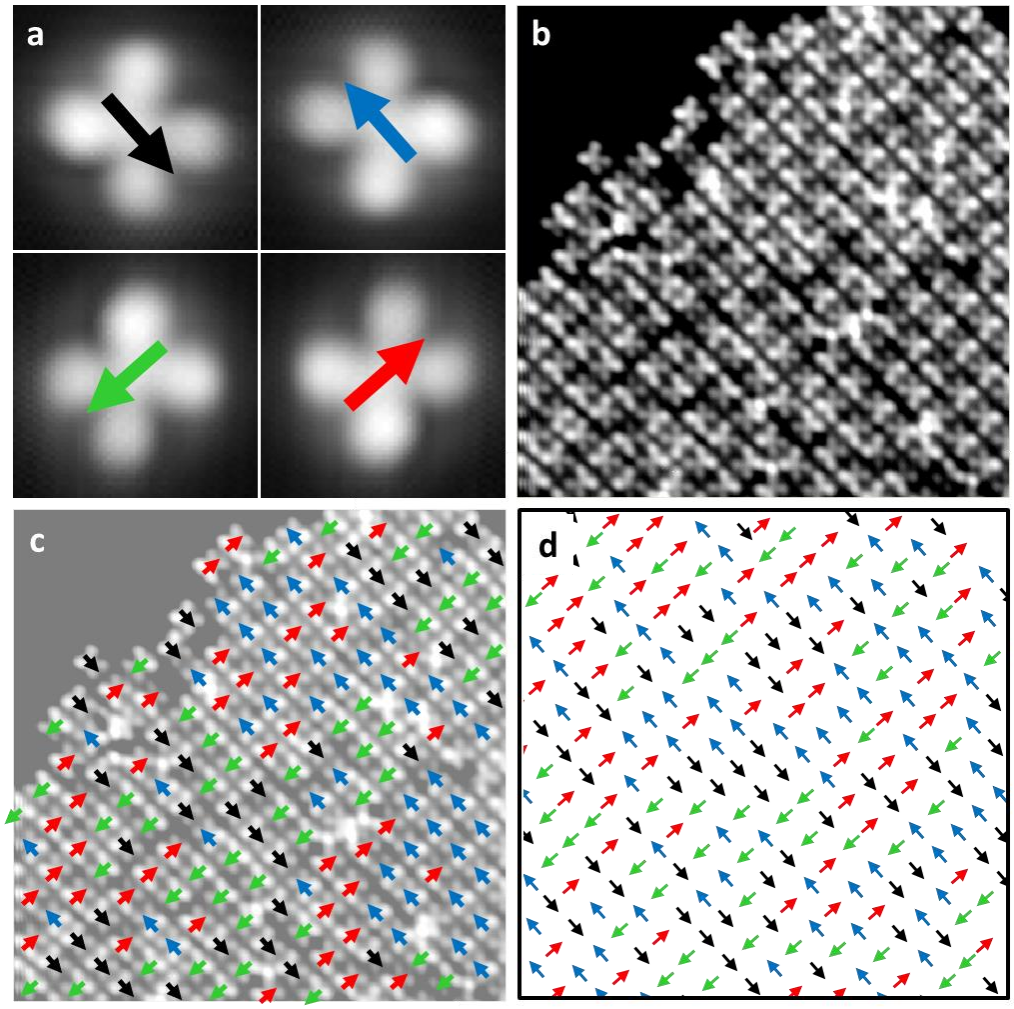

Figure 5.8 Pairwise analysis of AP configurations within molecular islands. (a) Each of the four equivalent meta-AP configurations is assigned a coloured arrow. (b) STM image of an AP island (I = 1.10 nA; V = 0.1 V). (c) Same STM image with colour coded arrows overlaid. (d) Randomly generated array for comparison with experimental data.

The pairwise analysis considered directly adjacent molecules only. Because of the square symmetry of the islands, this means that each molecule has four direct neighbours. Since there are four states of the molecule (i.e. four coloured arrows), there are 16 different way to pair them. Considering that the surface imposes a directionality, there are a further 16 pairings. Among the 32 distinct pairings (shown in Figure 5.9), there will obviously be symmetrical equivalencies but, for now, we will analyse each pairing separately. Later it will be shown that the equivalent pairings are related, and are revealed by the statistical analysis.

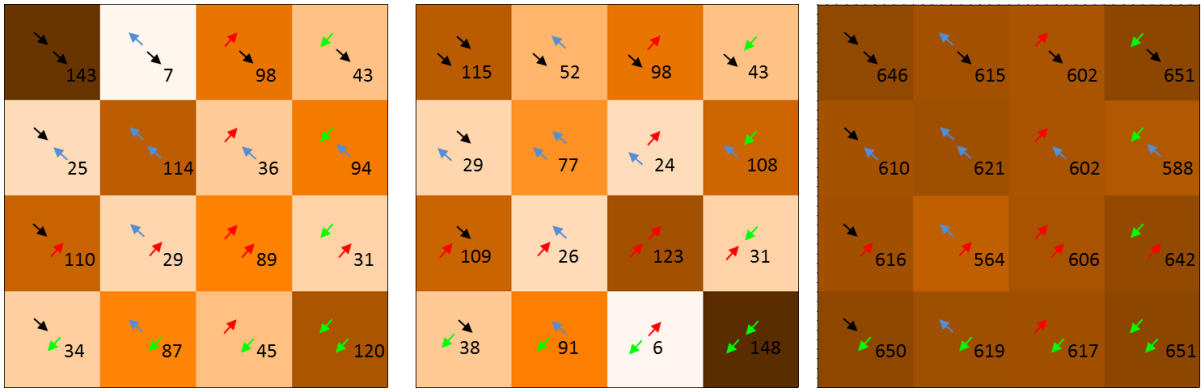

Figure 5.9 (Left and middle) The occurrence frequencies of the 32 possible adjacent AP-AP pairings. A total of 2223 pairings were examined; darker colouration represents more common molecular pairs. (Right) Example result of the same analysis performed on a randomly generated array of 9990 molecular pairs.

2223 pairs of molecules were counted from many STM images, and arranged into symmetrical matrices based on their frequency of occurrence as shown in the first two matrices of Figure 5.9. The darker colour in these matrices represents a pair which was seen more often (conversely, light colour is least frequently observed). We can immediately see that higher intensity colour is present along the diagonals which contain pairs of the same colour. This is already an indication that clustering of colours seen in the initial analysis is not random. Another interesting point is that the two configurations in which the arrows point away from each other (i.e. both bright lobes of neighbouring AP molecules are face on) are hardly seen – in total, only 13 times out of 2223.

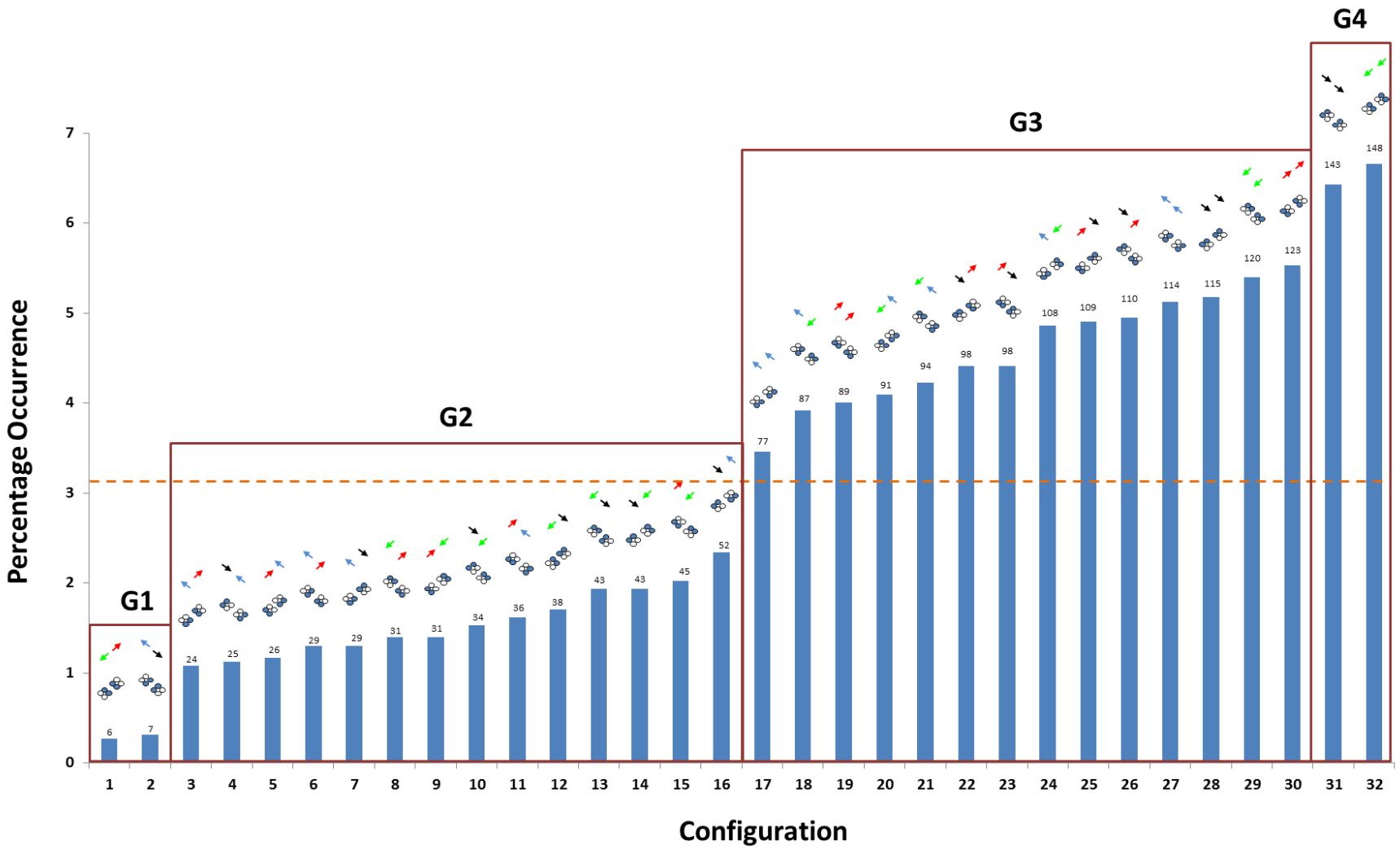

Figure 5.10 Relative occurrence of each AP-AP configuration, showing four distinct groups. The dotted line indicates the average number of counts per pairing, which is expected in the case of random pairing.

To convince ourselves that the distribution of paired molecular configurations is not random, we can perform the same analysis on the aforementioned randomly generated molecular island. From the third matrix in Figure 5.9, it is clear that this is the case, because the random matrix has a homogeneous distribution of occurrence frequencies indicated by a single colour. For the random case, 9990 pairs were considered to show the behaviour in the limiting case, but a similar distribution was observed using 2223 random pairs.

After counting and observing the apparent deviation from random behaviour, the frequencies of the 32 pair configurations were plotted in a histogram ordered from least to most frequent (Figure 5.10). Interestingly, based on their relative occurrence, the data show four distinct groups in which we have a group of 2, then two groups of 14, and finally a group of 2 (the groups are labelled G1 to G4 in Figure 5.10). Due to their relative abundances we can say that the 32 pairs which make up these groups lie on a spectrum ranging from disfavoured to favoured, compared to what we would expect from the random case. The horizontal line at 3.125% in Figure 5.10 indicates the average number of counts per pairing. Anything below this line indicates a configuration which is repulsive in nature, and anything above has an attractive interaction.

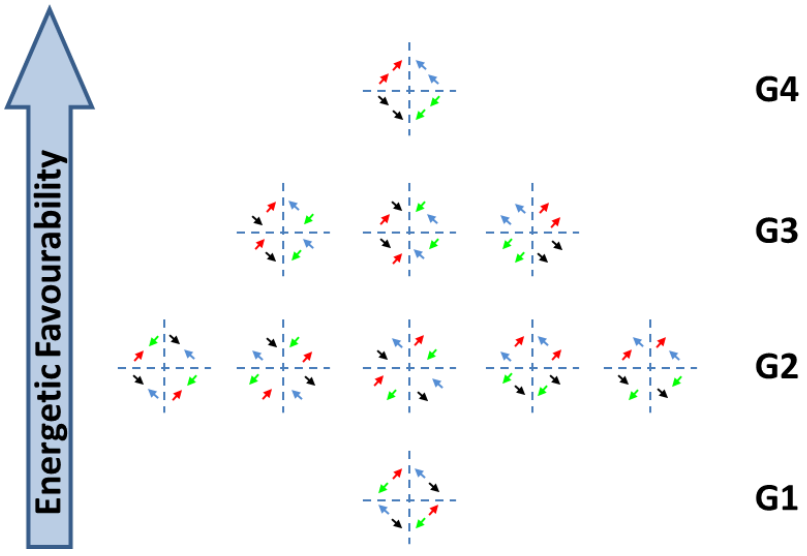

Figure 5.11 Reflectional equivalence of AP-AP pairs within the four subsets seen in Figure 5.10. Dotted lines are mirror planes.

If we look at the first (least favoured) subgroups, it can be seen that, if one of the pairs is reflected through a horizontal or vertical mirror plane, the other configuration is achieved. This is shown in Figure 5.11. This reflectional equivalence can be extended to the other subsets. Specifically, if we choose any AP-AP pair in the second subset (G2) and reflect it, its reflection is found within the same group. From this group we can derive 5 symmetric quartets. All 14 pairs

of molecules are accounted for: two quartets contain 4 distinct pairings, and three contain 2 due to symmetry reasons. Moving to group G3, we again see symmetric equivalencies between all of the members of this group. There is, however, one exception: the two states which are observed to have the highest occurrence frequency have their mirror images within this lower set. That is to say that we have only one symmetric quartet in which the configurations within the set of four do not have similar populations. The reason for this is not obviously clear because the four configurations are symmetrically equivalent, even when the underlying substrate is taken into account. By summing the statistics for each group of four and replotting (Figure 5.12), we can see the stark difference in energies for each set of symmetrical pairs. As mentioned, the data can be thought of as a relative ordering of the interaction energies of molecules in different states.

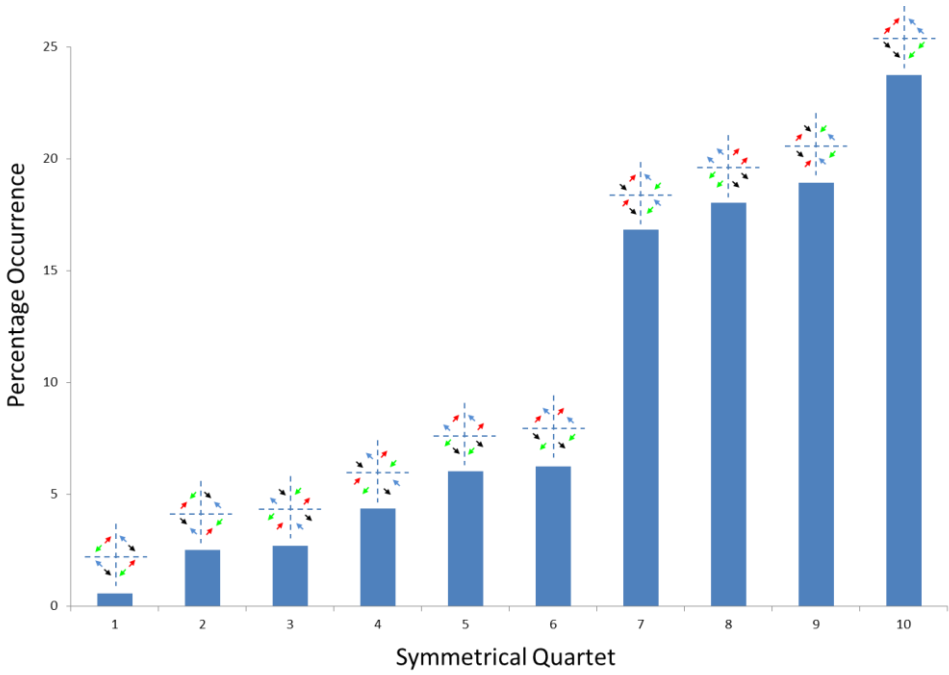

Figure 5.12 Relative occurrence of each of the symmetric quartets shown in Figure 5.11.

The symmetry relations between different molecular pairings, derived from the above pairwise analysis, define an energetic ordering of the favourability of intermolecular interaction. This can be used to describe the way in which the molecular islands might grow on the surface. In the low flux deposition regime, we can assume that individual islands grow from a single molecule which forms a nucleation point at a terrace defect or a step edge. Incoming additional molecules then have sufficient diffusivity to probe the available sites presented by the nucleation centre (i.e. the first molecule). It is then possible that, upon finding the lowest

energy site, a Cu atom is drawn from the substrate and the mutual interaction of both molecules with this adatom prevents further diffusion or dimer dissociation. With further growth of the islands, access to the lowest energy pairings becomes more difficult to achieve, and instances of uncommon molecular pairings will occur. One might expect extremely ordered islands; however, the short range interaction of molecules arriving at the surface leads to statistical variation and pairing of AP which are unfavourable. Correspondingly, we see islands which display no long range crystallinity but which is not completely random.

Despite determining that the islands have order according to the states of neighbouring molecules, the pairwise analysis does not explain why the switching in AP is deactivated in the majority of cases.

5.4 Discussion and Conclusion

To conclude, it has been shown that ordered two-dimensional arrays of AP can be formed on a Cu(110) surface. The degree of crystallinity seen within the self-assembled structures is controlled both by the flux of the incoming molecules and the temperature of the metallic substrate. High resolution STM imaging of the islands revealed the presence of additional adsorbates in the interstitial spacings of the molecular islands. These species were attributed to Cu adatoms, the origin of which is most likely from abstraction from the surface. Rather than being dispersed homogeneously throughout the islands, the presence/absence of these adatoms was found to be highly dependent upon the states of the surrounding AP molecules. It was also determined that there are two possible sites for adatoms in the spaces where 4 AP molecules meet; and the choice of site depends on the electronic density of the molecular lobes in the [001] direction of the surface.

Analysis of the tautomeric states of the molecules revealed that the islands do not grow in a random manner. Using a pairwise analysis, it was shown that the 32 possible pairings can be ordered in terms of their occurrence frequency and thus allows us to identify their relative stability. Furthermore, it was found that the likelihood of a molecular pairing was directly linked to the symmetry of the two molecules with respect to the underlying substrate. Attempts were made to link the pairwise analysis to the likelihood of finding a molecule capable of switching but no clear connection was found.

Unfortunately, it has not been possible to find an explanation as to why some of the molecules within the islands switch and other do not. On the whole, individual AP molecules within the islands do not display the characteristic switching property seen in their isolated form. Even when the tunnelling bias is raised well above the 0.35 eV threshold, the switching is still inactive. From the analyses above it has been found that the presence of Cu adatoms is dictated by the chemical groups of the surrounding molecules. Furthermore, it has been found that the islands are not formed as a result of random growth, but rather due to short range ordering dictated by the favourability of pairwise interactions. Despite these findings, the instances in which we do see molecules switching do not systematically happen for a particular configuration (i.e. a particular environment of Cu adatoms and specific molecular configurations does not give rise to switching). Had more instances of switching molecules been observed, a similar statistical analysis could have been performed to extract their general behaviour.

Further work in this area would be useful to describe the behaviour of the tautomeric switches in periodic arrays. This could include collection of additional STM images of the islands in order to observe more examples of the active molecules. A better understanding could lead to more accurate control of the switching property in the condensed phase. Theoretical modelling of this system, through DFT calculations, may allow us to confirm the identity of the included adsorbates as Cu adatoms and their specific adsorption site. If the state of each switching element in such an island could be manipulated, this could be applied to computer memory and would mean that the density of data storage can be substantially increased.

5.5 References

1. G. M. Whitesides, J. P. Mathias, and C. T. Seto, *Science*, 1991, **254**, 1312–1319.

2. T. H. Bayburt, Y. V. Grinkova, and S. G. Sligar, *Nano Lett.*, 2002, **2**, 853–856.

3. Z. L. Pianowski and N. Winssinger, *Chem. Soc. Rev.*, 2008, **37**, 1330–1336.

4. G. Decher, *Science*, 1997, **277**, 1232–1237.

5. J. M. Lehn, *Angew. Chem. Int. Ed.*, 1990, **29**, 1304–1319.

6. M. Bieri, M.-T. Nguyen, O. Gröning, J. Cai, M. Treier, K. Aït-Mansour, P. Ruffieux, C. A. Pignedoli, D. Passerone, M. Kastler, K. Müllen, and R. Fasel, *J. Am. Chem. Soc.*, 2010, **132**, 16669–16676.

7. Y. Tai, A. Shaporenko, H.-T. Rong, M. Buck, W. Eck, M. Grunze, and M. Zharnikov, *J. Phys. Chem. B*, 2004, **108**, 16806–16810.

8. S. Stepanow, M. Lingenfelder, A. Dmitriev, H. Spillmann, E. Delvigne, N. Lin, X. Deng, C. Cai, J. V Barth, and K. Kern, *Nat. Mater.*, 2004, **3**, 229–233.

9. T. Classen, G. Fratesi, G. Costantini, S. Fabris, F. L. Stadler, C. Kim, S. de Gironcoli, S. Baroni, and K. Kern, *Angew. Chem. Int. Ed.*, 2005, **44**, 6142–6145.

6 Asymmetric Control of a Bistable Molecular Switch

6.1 Summary

This chapter in concerned with the spatial mapping of the location of the STM tip during excitation of the AP molecular switch. Maps of the molecular state preference and the switch rate are produced. These are interpreted and discussed to reveal that the molecule possesses an asymmetry in the control of which final state is produced. This is due to the selection of a particular reaction intermediate which is dictated by the symmetry of the underlying Cu(110) substrate.

6.2 Introduction

In this chapter we return to AP in its isolated form, which was characterised as a tautomeric molecular switch in Chapter 4. The process was shown to be stimulated by inelastic tunnelling electrons, which induced the transfer of the two amino hydrogen atoms to the opposite imino groups. This process lead to switching between two equivalent tautomers: *meta* and *meta'*. When measured in the tunnel junction of an STM, the current showed two distinct values. With large, measurable differences in conductivity, which can be alternatively accessed, this property indicated the usefulness of AP (and its derivatives) as a molecular switch. Through theoretical calculations, it was determined that the reaction pathway for the switching process follows a *meta* → *para* → *meta'* route. Additionally, it was found that there existed two, non-degenerate para intermediates, and *para*-2 (see Chapter 4) had the lowest energy and hence was the favoured intermediate involved in the switching pathway. The requirement for a switch is that it must have two (or more) accessible and distinct states. In this regard, AP is the first tautomeric molecular switch based on the new class of compounds known as quinone derivatives. However, an attractive feature of any switch is that its state is controllably accessed upon a specific external stimulus being applied. Until now we have only focussed on the random telegraphic switching behaviour. In this chapter it is revealed that the AP molecule has a further property, yet unreported for any other molecular switch, that allows complete

control over the final state of the molecule. This has the potential for great impact in the field of molecular electronics.

As discussed in Chapter 4, with careful control of the tunnelling parameters, the bistable nature of AP allowed the final state of the molecule to be chosen. This, however, required control from the STM user to stop the inelastic electron excitation when the desired state occurred. In other words, activation from the STM tip would induce switching, but without human intervention, one cannot say with any degree of certainty what state the molecule would end up in. This is a major flaw in the design of molecular components in general. Many molecules have been reported as switches owing to their bistability[1–3]. However, unless the state of the molecule can be reliably controlled, their usefulness in nanoelectronics may be limited.

To bring molecular electronics a step closer to functional use, this issue must be addressed. The requirement is that a specific stimulus will switch a molecule "on" and a different stimulus will switch it "off". Very few studies on molecular switches have been conducted which report this level of control. It is common that the *rate* of switching can be controlled through adjustment of the excitation energy[4]. But this is simple demonstration of Arrhenius behaviour and is true of any system activated by heat, inelastic electrons, or photons. A specific example of the control of the final state of the molecule has been shown with a $Cu[PVBA]_2$ complex[4]. By ramping the pulse voltage from negative bias to 0 V, the high current state could be produced with 100% accuracy. Alternatively, in going from a voltage near the Fermi level to -2 V the low current state could be achieved. Although controllable, this system has the unattractive feature that the switch involves formation and cleavage of a chemical bond and simultaneous movement of one of the PVBA ligands. This movement is not desirable when integrating molecular components into a "real-life" circuit as the connection to the electrode will be interrupted. In a separate example, the final state of a porphycene molecule was externally controlled by approaching the molecule with a Cu adatom[5]. In this case, the state of the molecule was fixed when the Cu atom is at its closest possible proximity. This external atom acted to generate an asymmetry in the double potential well of the isolated molecule, which rendered the molecule non-bistable, and hence favoured a particular molecular state. By changing the side of the molecule on which the adatom is located, the other tautomeric state could be chosen. This method of control is perhaps not so easily to implement, but nevertheless, is one of the few examples in the published literature. The issue addressed in this Chapter is that we can maintain the equivalence of the final state of the molecule (i.e.

symmetric potential well unaffected, with the two final states maintained degenerate), while imposing high control on the final configuration.

In this chapter, it is revealed that the aforementioned AP switch can be controlled by choosing the position in which the electrons are injected from the STM tip. Through high resolution mapping of the molecule in the x,y plane, the spatial dependence of the switch rate and the molecular state preference are shown. The results show that a strong preference (>95%) for one or the other *meta*-AP configuration is present when the manipulation is performed over specific phenyl lobes. This behaviour is explained in terms of the cross-sectional probability of one or the other amino protons being transferred upon ballistic interaction of with a tunnelling electron. The non-degeneracy of the two possible *para*-AP intermediates, which arises from the symmetry of the substrate (see Chapter 4), means that only the *para*-2 intermediate is involved in the reaction pathway. This imposes an asymmetry in the switching behaviour which allows us to control the tautomeric state of the molecule while maintaining the symmetry of the double potential well. Finally the chapter will discuss the implications of this discovery to molecular electronics. Bringing controllability to a system makes a random switch into a useful switch, and opens opportunities in construction of much more complex structures for nano-electronics.

6.2 H-tautomeric State Control in AP

6.2.1 Spatial Dependence of Switching Behaviour

In Chapter 4, all measurements of switch rate were performed over an off-centre symmetric position between two lobes of the same brightness (as shown in Figure 4.6). The same position was chosen to make the results consistent and comparable, and to provide a clearly measurable difference in current between the two tautomeric states. It was found, in the early stages of the investigation, that a strong preference for a particular state was evident in the *I* vs *t* measurements when the electronic excitation was performed over individual phenyl groups. The switch rate was more easily measured when there was a 50/50 distribution between the high and low states and this is why the off-centre symmetric position was chosen in Chapter 4. But that is not to say that the end result (determination of the activation energy) would be any different if a different position was chosen. The preference of the molecule to occupy a particular state will now be explored.

The two equivalent adsorption configurations of AP at both positive and negative 0.43 V were studied (that is, with an electronic excitation above the threshold for activation). The experimental details for the data acquisition are the same for all four cases, and are detailed for a single example as follows. First, a constant current STM image of a molecule of interest was acquired as shown in Figure 6.1a. Next, open-feedback measurements of the tunnel current were made on an equally spaced 51 × 51 grid over the STM image (totalling 2601 individual measurements). Each *I* vs *t* measurement of the tunnel current contained 2000 points, measured over a period of 0.2 s, giving a time resolution of 100 μs. This resolution, at this bias voltage, is sufficient to capture all of the switch events. The first 51 spectra are collected across a single horizontal line at the top of the image and there is an interval of 0.002 s taken between each one. During this interval the feedback electronics are reactivated, the tip returns to the set-point height, and the tip moves to the next measurement position. After the first 51 spectra are collected, the next 1/51 of the molecule is imaged and then a further 51 spectra are collected. This process is repeated until all 2601 are collected, and the whole grid spectrum acquisition takes approximately 10 minutes. In this time the thermal drift of the sample, relative to the tip, is negligible (comparison of topographic images before and after data acquisition reveals a shift of approximately 0.5 Å), and so, the resulting maps can be considered spatially accurate.

One issue that arises during data collection is that when a spectrum ends with the molecule in the opposite state to the initial state, the set-point height is slightly different in the next spectrum. This results in a slight change in the tunnel current, which means the next measurement will have a slightly higher/lower switch rate as the last one. Due to the switching nature of the molecule, this is, unfortunately, unavoidable. However, the effect is negligible (very small change in *I*) and is averaged out over the whole image and therefore does not drastically affect the results.

The resulting 2601 spectra show the expected telegraphic noise known from our previous experiments (Chapter 4). Spectra collected in the area surrounding the molecule do not show any switch events because the tip is not directly above the molecule. Similarly, no switching is recorded in the central region of the molecule (along the switch axis) due to no change in the apparent height of the molecule in this zone. The molecule is, however, rapidly switching during these voltage manipulations but the conductance difference in between the two states can't be distinguished. When the tip is elsewhere above the molecule, the two levels in the tunnel current are clearly visible.

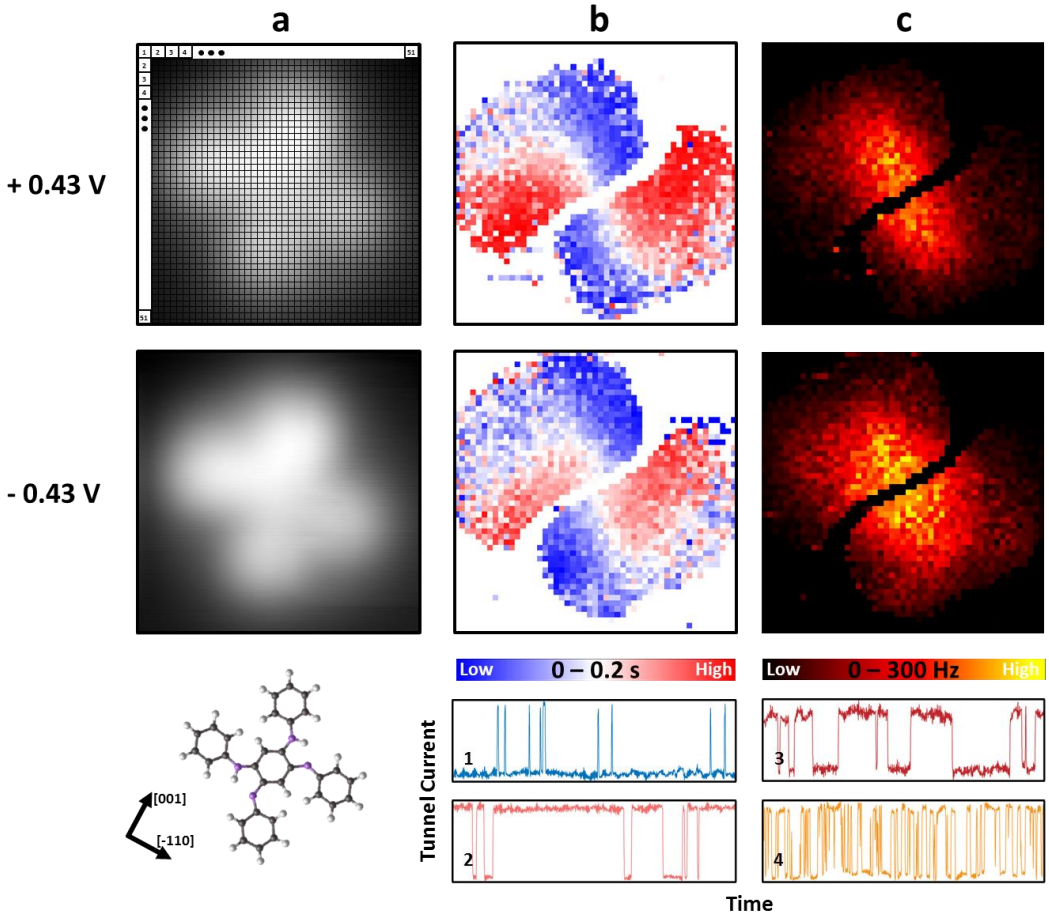

Figure 6.1 Spatial mapping of current state preference and switch rate in AP, measured at ±0.43 V. (a) Top – 51 × 51 grid, each point on which an *I*/*t* measurement is made; Middle – STM topography of AP; Bottom – Ball and stick model of AP with Cu(110) directions indicated. (b) Spatial dependence of measurement location with current preference – blue represents a preference for low current (example spectrum 1); red represents a preference for high current (example spectrum 2). (c) Mapping of switch rate – maximum rate (spectrum 4) is observed at the centre of the molecule and decreases radially (spectrum 3).

From these data, two maps of the molecule were produced: a state preference map and a switch rate map. In the first case, the time in which the high current state is occupied in each *I*/*t* spectrum is plotted in a 51 × 51 matrix. This number can range between 0 (only low state) to 0.2 s (only high state). The colour scale for the map in Figure 6.1b reflects this, with blue representing low current preference, red high current preference, and white represents the case where both are seen for equal times. The scale bar shows, at its extrema, the cases where the low and high states are occupied for the whole duration of the measurement. However, these two extreme cases are not shown in the map because an *I*/*t* spectrum in this case would display no switching events. It is therefore impossible to determine which state the molecule is in, so the pixel is coloured white.

The switch rate maps for ±0.43 V are displayed in Figure 6.1c. Unlike the analysis performed in Chapter 4, the switch rate in the present analysis must be determined differently. This is because a very high number of switch events are required to reliably fit the data with an exponential function to extract an exact switch rate. In the present data set, the number of events is insufficient to do this. Instead, the normalised number of switch events per second for each spectrum is used to provide the contrast in these maps. The colour scale shown applies to both of the switch rate maps and runs from 0 (black) to 300 (yellow) switch events per second.

In the current preference map there is a clear similarity to the topography of AP with the four coloured regions corresponding to individual amino/amino phenyl side groups. We have two diagonally opposite lobes which show a preference for the low current state (indicated in blue) and in the other two lobes the high current state is preferred (red). We also note that, in the regions between the blue and red areas, there is no preference for either high or low current and this is coloured white, i.e. the switching process is symmetric with a 50%-50% accessibility distribution amongst the two states. From these data it can immediately be seen that pulsing on specific lobes of the molecule allows selection of the conductance state with a high degree of certainty. Specifically, at the location exhibiting the highest preference for a particular state, found in the map acquired with positive polarity, the molecule resides in that particular state for 98.9% of the manipulation. The same position in the switch rate map indicates that the molecule is switching and thus, the high preference is not simply due to a coincidental lack of activity during the acquisition of data. Importantly, the preference for a particular state is independent of the initial state of the molecule.

Until now, we have concentrated on the measured value of the tunnel current. The tunnel current is, of course, the method of determining the state of the molecule (i.e. the way of knowing if the molecule is in a *meta* or *meta'* state). When the high current state is measured, the chemical group which is directly below the tip is aminophenyl. Likewise, when low current is observed, the iminophenyl group is directly below the tip. With this information the current preference map can be reinterpreted in terms of the actual final state of the molecule. This is of interest if we want to make sense of the observed location dependence.

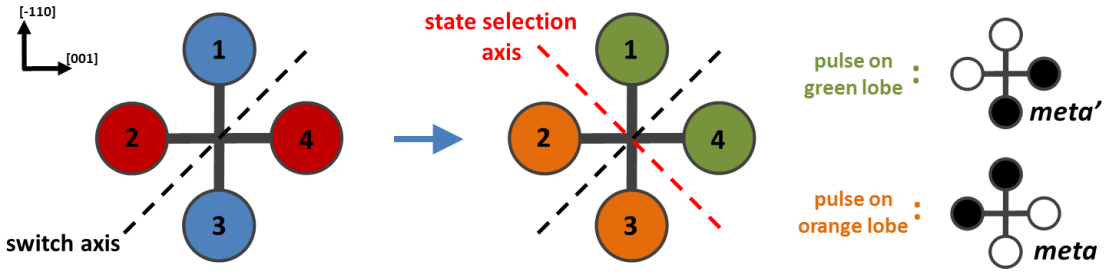

Figure 6.2 Schematic indicating that pulsing on one side of the state selection axis consistently produces a specific molecular state.

In Figure 6.2, the switch axis is defined and the lobes of the molecule are numbered 1-4. From the preference map we can see that pulsing on lobe 1 induces the low current state and hence the iminophenyl groups are in positions 1 and 2 (i.e. *meta*). If the pulse is performed over lobe 4 we induce the high current state. However, this means that the iminophenyl groups are still in positions 1 and 2. So, pulsing on lobes 1 and 4 gives different values for the tunnel current but returns the same final molecular configuration. The same can be said for pulsing on lobes 2 and 3: different current preferences, but *meta'* is consistently found to be the final state of the molecule. By replotting the current preference map, we can produce a map showing the preferred molecular configuration with respect to the location of electron injection. This is also shown schematically in Figure 6.2 where we have defined a further 'state selection' axis which is perpendicular to the switch axis. By providing electron excitation on one side of the state selection axis, a specific molecular state may be consistently produced.

Comparing the preference maps (Figure 6.1b), we see the same general behaviour for each at positive and negative bias. This indicates that the voltage polarity does not affect the spatial activation of the switch, and it was shown in Chapter 4 that the switch rate and activation energy are also not changed by the direction of tunnelling. This mirror behaviour at both polarities means that tunnelling into empty states (at positive bias) of out of filled states (at negative bias) does not play a major role in the switching mechanism.

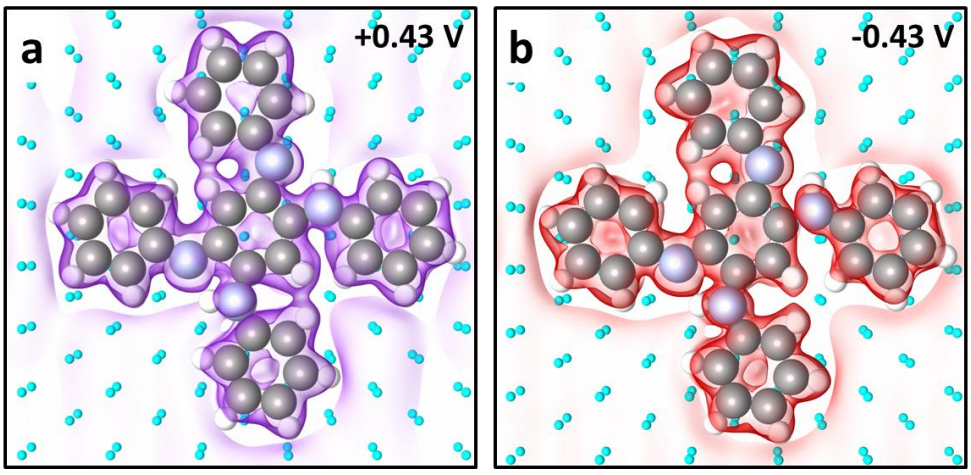

Figure 6.3 Charge density isosurfaces of the AP/Cu(110) system. Bands 0.43 eV above (a) and below (b) the Fermi level were summed to produce the above images.

A further indication that the tautomerisation reaction is not linked to the electronic structure of the molecule is seen in the switch rate maps. The maps of switch rate show a simple elliptical Gaussian distribution centred on the molecule. Its maximum lies at the middle of the central 6 membered carbon ring of AP and the switch rate decreases radially outwards. Although no data is measured at this point, due to the lack of a change in the apparent height of the molecule, interpolation of the data allows us to locate the maximum of the switch rate distribution at the centre of the molecule. The shape of the distribution again points to the fact that coupling to the electronic orbitals of the molecule plays no role in the tautomerisation process. If the mechanism governing this switching was mediated by, for example, injection into the LUMO, we would expect maxima in the switch rate map corresponding to the shape of this MO. The comparison of this map with the optimised DFT electronic isosurfaces, 0.43 V above and below the Fermi level, (Figure 6.3) shows that this is not the case. Using the DFT optimised structures from *meta*-AP, these images were produced from the charge density isosurfaces taken 1×10^{-4} e Å^{-3} with unit cell dimensions $17.85 \times 20.21 \times 25.26$ Å^3 (done by Jose Garrido Torres, University of St Andrews). The bands between the Fermi level and ±0.43 eV were summed to simulate the experimental conditions. It can be seen that MOs both above and below the Fermi Level display similar shapes and are distributed over the whole molecule. If a perturbation of the MO resulted in coupling to the vibrational structure of AP, we would expect see similar switch rates over the whole molecule. This seems to be the case for naphthalocyanine[6], whereby an asymmetry in the switch rate map indicates tunnelling into the LUMO. Furthermore, the maximum switch rate in this example is observed at the periphery of the molecule, relatively far away from the active hydrogen atoms. We also note that the work in reference[6] was conducted on a decoupling NaCl bilayer, whereas our substrate is metallic.

The only noticeable difference which is seen in the switch rate maps is that, at positive polarity, the spread of the distribution is narrower compared to the opposite polarity. The reason for this is not entirely clear. It was initially thought that coupling to different electronic bands may have been responsible. However, as seen above, the shape of the orbitals at both polarities is very similar.

6.2.2 Explanation of Observed Behaviour

At this point we know that AP can be used as a controllable molecular switch. By pulsing over particular regions of the molecule, the final state can be selected with a very high degree of accuracy (as shown above, 98.8%). It has also been shown that inelastic tunnelling into or out of the LUMO/HOMO does not affect the tautomerisation process. We do know, however, that the process is an example of inelastic scattering from Chapter 4, where it was found that the switch rate is linearly dependent on the tunnel current. This therefore gives rise to an obvious question: what is the specific physical process, which involves inelastic tunnelling, responsible for the observed switching behaviour? Furthermore, what is the reason behind the observed pattern in the preference maps?

In order to address both of these questions, it is important to recap the reaction pathway for the *meta* → *meta'* transition. It was shown that transfer of the amino hydrogens did not occur in a concerted manner but rather a sequential one. In this process, a single proton hops to the opposite imino group to produce a relatively unstable *para*-AP intermediate state. This is then quickly followed by return of the same proton (return to the original state), or movement of the second proton (to produce the switched form of the molecule). The choice of which proton moves first implies two possible *para*-AP intermediates exist. Through NEB calculations, it was proved that these two species are non-degenerate due to the symmetry of the Cu(110) substrate. The activation barrier leading to the *para*-2 state is the lowest and therefore favoured route for tautomerisation.

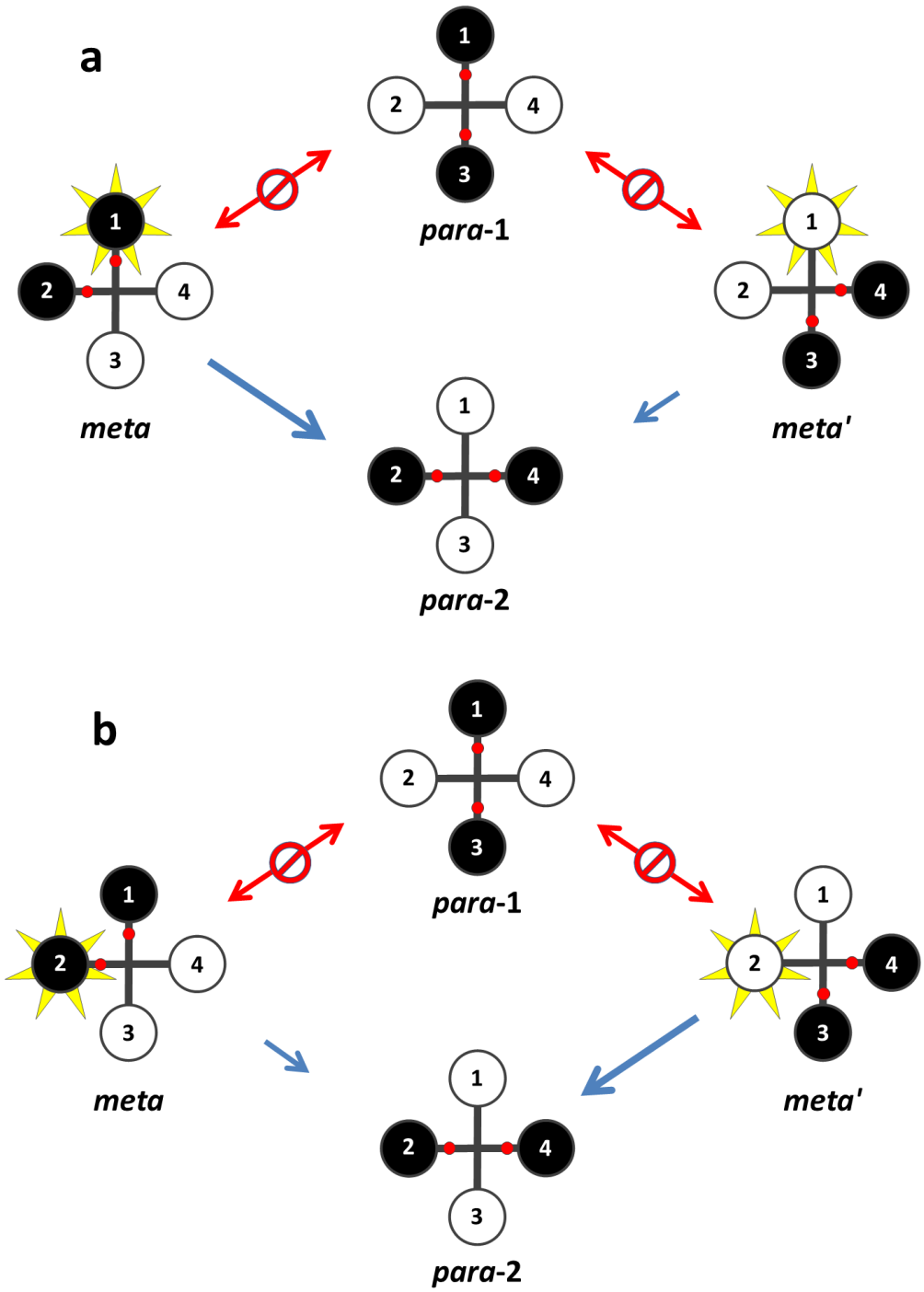

Figure 6.4 Origin of the switch control. Aminophenyl lobes are represented in black; iminophenyl lobes are represented in white; pulse location is indicated in yellow. (a) Electron injection on lobe one results in a preference for the low current state and hence *meta'*. (b) Electron injection on lobe 2 results in a preference for the high current state and hence *meta*.

With this knowledge, it is possible to interpret the molecule state preference maps (Figure 6.1). The map shows that the *para*-2 state is the only intermediate responsible, and it may be explained in terms of probability cross-section for the ballistic collision of a tunnelling electron with a tautomeric hydrogen atom (or corresponding phenyl ring). Consider first applying a

voltage pulse on lobe 1 as indicated in Figure 6.4a. The proton occupying lobe 1 is closer to the point of electron injection and therefore has a higher probability to be activated than the proton on lobe 2. The movement of this proton produces the favoured *para*-2 intermediate with a high probability. The *para*-2 then has equal probability to decay to either the *meta* or *meta'* species. Assuming that the *meta'* is achieved, and with the same electron injection location, we can see that the proton on lobe 4 is in closer proximity than that on lobe 3. We would therefore expect the *para*-1 intermediate to be formed with high probability. However, it is known that this intermediate is disfavoured due to energetic arguments, and therefore only the movement of the proton on lobe 3 will return the molecule to the original state. The reverse process occurs with a much lower probability than the forward process, and hence, when the STM tip is positioned on lobe 1, the *meta'* state is preferred. This agrees with the experimentally observed behaviour in that we see a preference for low current (corresponding to an iminophenyl group) on this lobe.

The same argument holds for a pulse on lobe 2 (Figure 6.4b). The proton closest to the tip pulse, when the molecule is in the *meta* state, is not transferred to the opposite imino group because this would result in the production of the unfavourable *para*-1 intermediate. Instead, with low probability, the proton occupying lobe 1 is transferred to produce *para*-2. Then, let us assume that relaxation of this intermediate results in the switched *meta'* form of AP. In this state, and with the same tip position, the movement of the proton on lobe 3 is much more probable, and return to the *meta* state occurs. The less likely transfer of proton 2 in the *meta* state, coupled with the favoured transfer of proton 3 in *meta'*, result in the *meta* configuration to be preferred when the voltage manipulation is performed over this lobe. Again, the experimental observation of high current preference is in agreement with this. Exactly the same behaviour is observed in the equivalent adsorption configuration in which the molecule is rotated 90° with respect to the surface.

The above arguments are the only way to rationalise the behaviour observed in the preference map. If the counterexample is taken, where the *para*-1 state is the preferred intermediate step, we would see an image with inverted contrast compared to the result observed .This is based on the argument that the location of the tip with respect to the tautomerisable hydrogen atoms dictates the probability of reaction. Furthermore, if both of the para intermediates were used in the reaction pathway, the contrast in the preference map would be lost and the state preference would show homogeneity across the map due to averaging out of both the *para*-1 and *para*-2 cases. We can, in fact, take this further and say that the

current preference maps may be interpreted as the *para*-2 intermediate. During the collection of data, the molecule is rapidly switching below the tip, and at each location we see an average behaviour of the preference of the molecular state. When this is expanded across the whole molecule, we can say that the average state of the molecule during acquisition of the map is the *para*-2 state. In this description, red areas indicate the high current state and represent an aminophenyl group below the tip; blue areas indicate the low current state and represent an imino phenyl group directly below the tip. The chemical configuration of the *para*-2 state and the contrast of the map are in good agreement and thus represent an indirect way of imaging a reaction intermediate.

Control of the state of AP originates from the fact that the tautomerisation process has two non-degenerate pathways. *Para*-2 is the sole reaction intermediate due to it providing the lowest energy route from *meta*-AP to *meta'*-AP. On a substrate which matches the symmetry of the molecule, such as Cu(100), there is no reason to believe that reaction pathways involving *para*-1 and *para*-2 would be of differing energies. The non-degeneracy in the AP/Cu(110) case is imparted by non-equivalence of transferring a proton from each of the aminophenyl to the corresponding opposite iminophenyl groups. This leads to a spatial asymmetry in the preference of the molecular state, based on the proximity of electron injection to the proton whose transfer would yield the *para*-2 state. The final states of the molecule remain energetically equivalent, and thus, we can say that this is the first example of asymmetric control of a purely bistable molecular switch.

6.2.3 Outlook

An interesting result is that the state of the molecule can be controlled using only lobes 1 and 2, which always possess the same functional groups. In this way, the molecule can be considered to have two lobes which control the state (1,2; input) and the opposite two lobes (3 and 4) control what the output reads. This useful feature may be harnessed in future applications by attaching one side of the molecule to a circuit and this leaves the other side of the molecule free to control the conductance behaviour of the circuit.

Such control of the state of AP has never before been shown for another molecular switch, and represents an important step towards producing nanoelectronic components that would function as part of a 'real-life' circuit. Currently, the most ubiquitous electronic component is the transistor. As discussed previously, the miniaturisation of silicon transistors cannot go on

indefinitely due to power consumption and quantum interference effects. The current system can be thought of as a three terminal system: lobe 1 switches the molecule “on”, lobe 2 switches the molecule “off”, and lobes 3 & 4 provide a readable output. A comparison can be drawn with a transistor, in that a small current at the base electrode (Figure 6.5a) allows a large current to flow across the other two gates. Without this small current, the circuit is deactivated, and thus the transistor functions as a switch. If the AP molecule could be integrated into such an architecture, with nanowire attachments at each of the input lobes and the output lobes as part of a larger circuit, control of a circuit could be achieved. Not only would this control be facilitated by a component which is an order of magnitude smaller, but power consumption is dramatically reduced owing to the requirement of a single electron to activate the switch. Furthermore, conventional transistors have a quadratic response to the applied voltage in order to allow switching; with a molecular transistor, the response is truly binary because of the discreet states of the molecule.

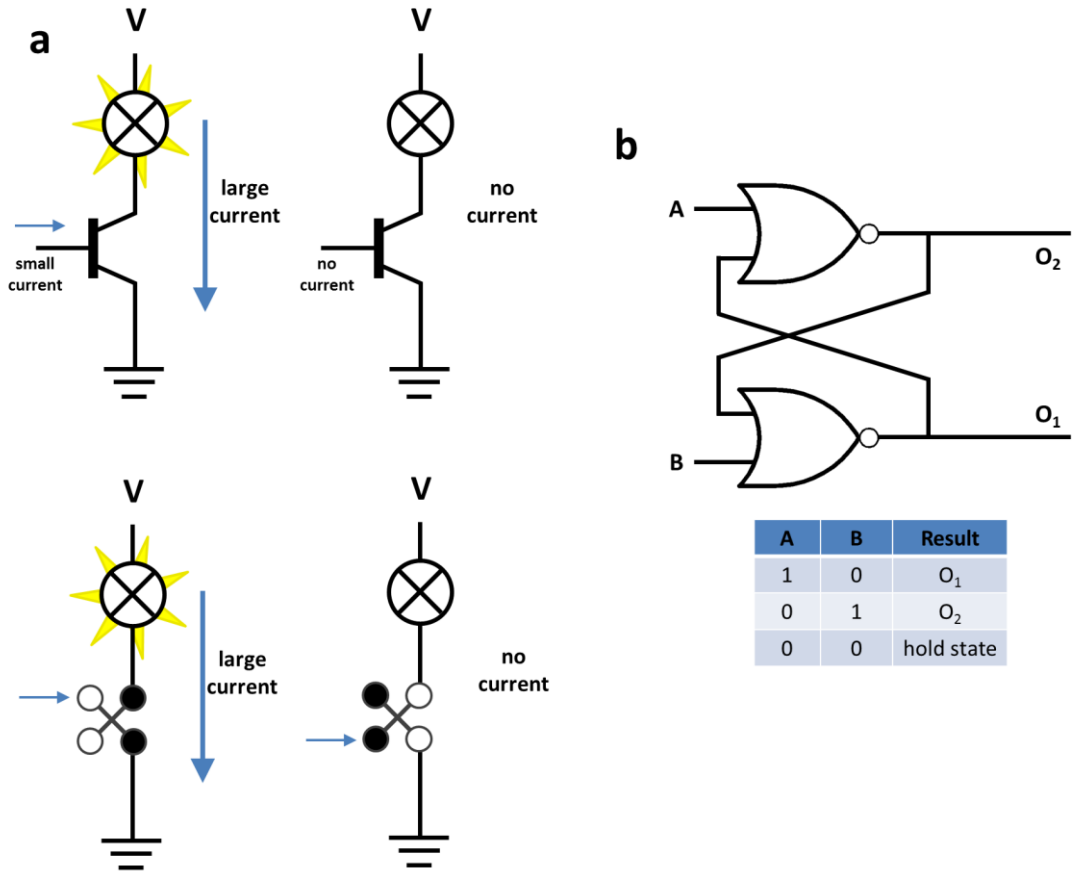

A	B	Result
1	0	O_1
0	1	O_2
0	0	hold state

Figure 6.5 Outlook on the utility of the state control property of AP. (a) In the same way that a transistor can be used to control current in a circuit, AP may also be used by providing excitation to a specific functional group. (b) The behaviour of AP is analogous to the function of a flip-flop circuit. Providing an input at A results in a sustained output O_1 (likewise for B and O_2).

An additional comparison that can be drawn from the AP molecular switch is that is can function as a flip-flop circuit. A flip-flop circuit is constructed from a pair of cross-coupled NOR logic gates as shown in Figure 6.5b, and has two stable states. When a signal is given to input A an output, O_1, is produced, and remains this way after the signal at A has ceased. Likewise, a different output, O_2, is generated when B is used as an input. AP mirrors this behaviour in that a pulse on lobe 1 produces a different state of the molecule than when a pulse is performed on lobe 2. In this application, the molecular switch may be treated as a programmable memory element, and due to its dimensions, the density of a memory storage device based on this technology could be vastly increased compared with today's standards.

6.3 Conclusion

It has been shown that, in addition to displaying tautomeric bistability, the state of AP can be controlled with a high degree of accuracy. By spatially mapping the molecule using STM spectroscopic methods, it was shown that, when specific peripheral phenyl groups of the molecule are injected with electrons, a particular state of the molecule was highly preferred. Both the switch rate map and the preference map point towards a process which is not mediated by coupling to the electronic orbitals of the molecule. In fact the structure observed in the preference map can be interpreted in terms of a probability cross-section for the ballistic interaction of a tunnelling electron with the molecule. The *para*-2 AP intermediate is solely selected during the reaction pathway due to it adopting a lower energy compared to the alternative *para*-1 state. This non-degeneracy is imparted by the underlying substrate which produces an asymmetry in the combined molecule-substrate system. The preference map indicates the presence of only the *para*-2. The ability to control the state of a molecule reliably is a new feature to this field of research and can be exploited in future applications such as transistor switching and logic devices based on single molecule functional units.

6.4 References

1. N. Pavliček, B. Fleury, M. Neu, J. Niedenführ, C. Herranz-Lancho, M. Ruben, and J. Repp, *Phys. Rev. Lett.*, 2012, **108**, 1–5.

2. M. Martin, M. Lastapis, D. Riedel, G. Dujardin, M. Mamatkulov, L. Stauffer, and P. Sonnet, *Phys. Rev. Lett.*, 2006, **97**, 1–4.

3. K. Morgenstern, *Acc. Chem. Res.*, 2009, **42**, 213–223.

4. R. Ohmann, L. Vitali, and K. Kern, *Nano Lett.*, 2010, **10**, 2995–3000.

5. T. Kumagai, F. Hanke, S. Gawinkowski, J. Sharp, K. Kotsis, J. Waluk, M. Persson, and L. Grill, *Nat. Chem.*, 2014, **6**, 41–46.

6. P. Liljeroth, J. Repp, and G. Meyer, *Science*, 2007, **317**, 1203–1206.

7 Conclusion

The field of molecular electronics is emerging as a viable solution to the problems faced in miniaturisation of electrical components. In particular, molecular switches are seen as the ultimate form of miniaturisation as they are the smallest stable structures capable of encoding binary signals. The thesis has been concerned with the use of scanning tunnelling microscopy to study these molecules in order to characterise their behaviour and develop an understanding of information storage at the nanoscale.

In the first instance, it was thought necessary to expand the limited library of tautomeric molecular switches. This type of switch is attractive in the sense that discreet conductance states are achieved through a subtle intramolecular change, and does not generally lead to a change in shape or position (important factors when considering integration into a circuit). The reported class of quinone-type molecular switches breaks away from the porphyrin-type H-tautomeric switches in that the proton transfer occurs on the periphery of the active unit rather than in a protective macrocycle moiety. Specifically, conductance bistability was measured in two example molecules, azophenine (AP) and azotolyline (AT). Under variation of tunnelling conditions, the process in AP was found to have an activation barrier of 0.35 eV and was stimulated by inelastic scattering of a single tunnelling electron. Computational modelling yielded qualitative agreement with the activation energy, and allowed confirmation that the double proton transfer occurs in a sequential fashion. Of the two possible reaction intermediates, *para*-2 was found to provide the lowest energy pathway for movement of H atoms from aminophenyl to adjacent iminophenyl functional groups. The retention of this remarkable property upon functionalisation of the molecule means that future iterations of this structure may be tailored to fit specific criteria, and assist in integration into “real-life” circuitry.

The next line of investigation tried to generate a densely packed array of the AP molecular switch. The reason for this was to probe the properties of AP in its two-dimensional condensed phase, with the focus of producing highly ordered self-assemblies of addressable memory elements. Unfortunately, it was not possible to achieve this due to the switching property of the molecule being quenched in the majority of cases. Methods were devised to try to explain why this was so, and included statistical analyses of both the molecule-molecule and molecule-Cu interactions. The pairwise analysis of molecule-molecule interaction revealed that

the islands are not random (as is the case on first impression), and in fact a relative ordering of 32 pairs of molecules exists. These pairs were found to be ordered in terms of their reflectional symmetry. Upon inspection using high resolution imaging, it was found that the islands included additional features in the interstitial sites of the molecules. These were attributed to Cu adatoms which have been abstracted from the bulk through strong interaction with surrounding molecules. It was found that their presence or absence in an interstice was heavily dependent on the electronic environment provided by four neighbouring AP molecular side groups. Although not confirmed, it was thought that the presence of Cu adatoms in the islands alters the potential energy surface sufficiently to force a single tautomeric state to be overwhelmingly preferred, and hence, deactivating bistability in most cases.

The study then returned to the AP switch in isolation after the discovery that the spatial dependence of the point of electron injection allowed control of the state of the molecule. This asymmetric control allowed selection of the high or low conductance states of the molecule with as much as 98.8% probability upon excitation of specific functional groups of the molecule. Production of a further map showing the switch rate as a function of location, followed by comparison to the optimised electronic structure, revealed that the process is not coupled to the electronic orbitals of the molecule. Instead the behaviour seen in the spatial maps was interpreted as a probability cross-section for the ballistic interaction of an inelastically scattered electron with the molecule. This interpretation was rationalised when the *para*-2 state was considered the only reaction intermediate involved in the proton transfer. The level of control is therefore conferred to the molecule from the non-degeneracy of the intermediates which results from the symmetry of the Cu(110) surface. This effect did not alter the bistability of the molecule in that the final states, *meta* and *meta'*, remained degenerate. This is the first such example of control of a molecular switch involving H-tautomerisation, and has great potential in future electronic applications.

The combined work of this thesis opens exciting new avenues of research. For example, the central active switching unit in AP could be miniaturised yet further by isolating just one imine-amine moitety (Figure 7.1) and transplanting it into another chemical structure. This would reduce the current system to a molecule capable of conductance switching, but which is based on the transfer of a single hydrogen atom. This leaves the possibility of functionalising the other side of the molecule with halogen atoms, which would allow linking of discreet switching units into dimers, trimmers, etc., by Ullmann-type reactions. Decoupling of individual

H-tautomerisation reactions within the same molecule could therefore allow much more complex molecular devices to be produced.

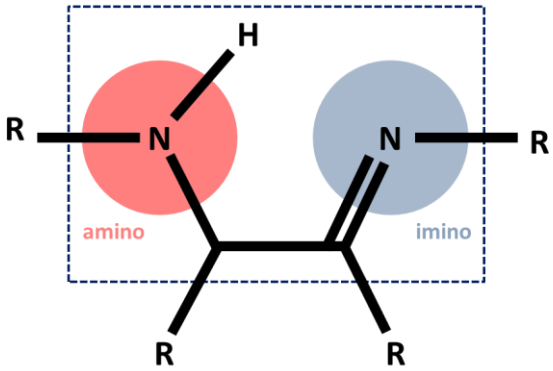

Figure 7.1 Fundamental amine-imine switching unit containing a single tautomerisable H atom. R represents locations for functionalisation of the structure.

An interesting way of furthering the work conducted on AP would be to attempt to deprotonate the molecule of its active hydrogen atoms completely. The deprotonated molecule has two resonance structures depending on where the negative charges are located, as shown in Figure 7.2. It may be possible to perturb the electric field near one of the nitrogen atoms using a charged species or an STM tip, and would result in the stabilisation of one of the resonance structures. Preliminary results show that a dehydrodgenation reaction does indeed occur in the AP/Cu(110) system and is likely catalytically activated upon heating. The structures observed are linear chains of AP molecules which have no apparent height differences in the four peripheral lobes. Further investigation could lead to stabilisation of a particular resonance structure and even transfer of this information along a one-dimensional molecular chain.

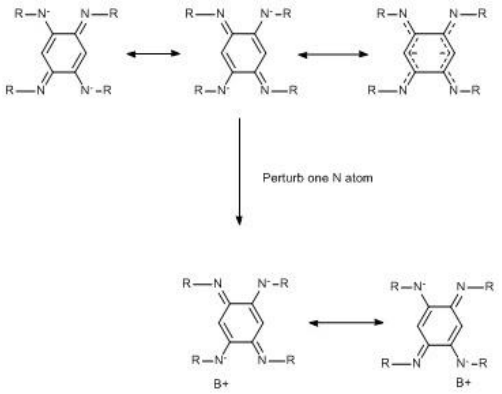

Figure 7.2 Scheme showing the two resonance forms of dehydrogenated AP (R = phenyl). Introduction of a charged species (B+) could lead to stabilisation of a one canonical form of the molecule.

List of publications

Directly related to current thesis

1. New Class of Metal Bound Molecular Switches Involving H‑Tautomerism
   G. J. Simpson, S. W. L. Hogan, M. Caffio, C. J. Adams, H. Früchtl, T. van Mourik, and R. Schaub
   Nano Letters 2014, **14**, 634-639.

2. Adatom-mediated stabilisation of a dense array of metal-bound molecular switches
   G.J. Simpson, J.A.G. Torres, Z. Abdullatif, H. Früchtl, T. van Mourik, and R. Schaub
   In preparation.

3. Asymmetric control of a metal-bound molecular switch – Towards the realisation of a single molecule transistor
   G.J. Simpson, J.A.G. Torres, H. Früchtl, and R. Schaub
   In preparation.

Other publications

1. Assembly of a Chiral Amino Acid on an Unreactive Surface: (S)-Proline on Au(111)
   R. T. Seljamae-Green, G. J. Simpson, F. Grillo, J. Greenwood, S. M. Francis, R. Schaub, P. Lacovig, and C. J. Baddeley
   Langmuir 2014, **30**, 3495-3501.

2. Adsorption of a Dihydro-TTF Derivative on Au(111) via a Thiolate Bonding Complex to Gold Adatoms
   J. S. Jethwa, F. Grillo, H. Früchtl, G. J. Simpson, M. J. Treanor, R. Schaub, S. M. Francis, N. V. Richardson, and R. A. Aitken
   Chemical Communications 2014, **50**, 10140-10143.

3. Formation of bioinorganic complexes by the corrosive adsorption of (S)-proline on Ni/Au(111)
   R.T. Seljamae-Green, G.J. Simpson, R. Schaub, H.A. Früchtl, J. Greenwood, F. Grillo, S.M. Francis, P. Lacovig, S. Lizzit, and C.J. Baddeley
   Submitted, 2014.